NASA/TM–20210024768

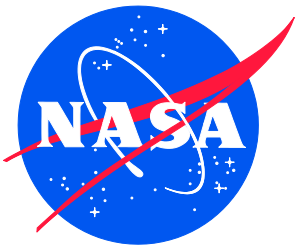

Buckling Test and Analysis of the 8-foot-diameter Sandwich Composite Cylinder Test Article CTA8.3 as Part of the Shell Buckling Knockdown Factor Project: Test Dates 16–19 December 2019

Kyongchan Song, Marc R. Schultz, Cyrus J. R. Kosztowny,
Adam Przekop, and Nathaniel W. Gardner
Langley Research Center, Hampton, Virginia

Michelle T. Rudd
Marshall Space Flight Center, Huntsville, Alabama

January 2022

NASA STI Program Report Series

Since its founding, NASA has been dedicated to the advancement of aeronautics and space science. The NASA scientific and technical information (STI) program plays a key part in helping NASA maintain this important role.

The NASA STI program operates under the auspices of the Agency Chief Information Officer. It collects, organizes, provides for archiving, and disseminates NASA's STI. The NASA STI program provides access to the NTRS Registered and its public interface, the NASA Technical Reports Server, thus providing one of the largest collections of aeronautical and space science STI in the world. Results are published in both non-NASA channels and by NASA in the NASA STI Report Series, which includes the following report types:

- TECHNICAL PUBLICATION. Reports of completed research or a major significant phase of research that present the results of NASA Programs and include extensive data or theoretical analysis. Includes compilations of significant scientific and technical data and information deemed to be of continuing reference value. NASA counterpart of peer-reviewed formal professional papers but has less stringent limitations on manuscript length and extent of graphic presentations.

- TECHNICAL MEMORANDUM. Scientific and technical findings that are preliminary or of specialized interest, e.g., quick release reports, working papers, and bibliographies that contain minimal annotation. Does not contain extensive analysis.

- CONTRACTOR REPORT. Scientific and technical findings by NASA-sponsored contractors and grantees.

- CONFERENCE PUBLICATION. Collected papers from scientific and technical conferences, symposia, seminars, or other meetings sponsored or co-sponsored by NASA.

- SPECIAL PUBLICATION. Scientific, technical, or historical information from NASA programs, projects, and missions, often concerned with subjects having substantial public interest.

- TECHNICAL TRANSLATION. English-language translations of foreign scientific and technical material pertinent to NASA's mission.

Specialized services also include organizing and publishing research results, distributing specialized research announcements and feeds, providing information desk and personal search support, and enabling data exchange services.

For more information about the NASA STI program, see the following:

- Access the NASA STI program home page at http://www.sti.nasa.gov

- Help desk contact information:

https://www.sti.nasa.gov/sti-contact-form/

and select the "General" help request type.

NASA/TM–20210024768

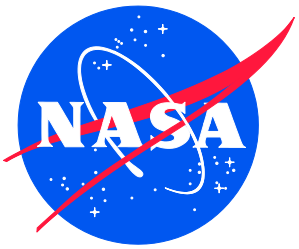

Buckling Test and Analysis of the 8-foot-diameter Sandwich Composite Cylinder Test Article CTA8.3 as Part of the Shell Buckling Knockdown Factor Project: Test Dates 16–19 December 2019

Kyongchan Song, Marc R. Schultz, Cyrus J. R. Kosztowny,
Adam Przekop, and Nathaniel W. Gardner
Langley Research Center, Hampton, Virginia

Michelle T. Rudd
Marshall Space Flight Center, Huntsville, Alabama

National Aeronautics and
Space Administration

Langley Research Center
Hampton, Virginia 23681-2199

January 2022

Acknowledgments

This work was conducted as part of the NASA Engineering and Safety Center (NESC) Shell Buckling Knockdown Factor Project, NESC assessment number 07-010-E. The CTA8.3 test article discussed herein was manufactured in an autoclave process by the Composite Technology Center at Marshall Space Flight Center, MSFC, (EM42). The testing was performed under the direction of Lucas Day by the Structural Strength Test Group (ET30) at MSFC. The authors would also like to thank Michael Lindell (Langley Research Center, LaRC) for his work in postprocessing data.

Available from:

NASA STI Program / Mail Stop 148
NASA Langley Research Center
Hampton, VA 23681-2199
Fax: 757-864-6500

Table of Contents

List of Figures

List of Tables

Nomenclature

3D	Three-dimensional
3D-DIC	Three-dimensional digital image correlation
AFT	Aft or bottom end of test article
CTA8.3	Cylindrical sandwich composite test article SBKF-P3-CYL-CTA8.3
D312	LaRC Structural Mechanics and Concepts Branch
DIC	Digital image correlation
DoF	Degree of freedom
E_1, E_2	In-plane extensional moduli in the fiber and matrix directions, respectively
EDI	Electronic displacement indicator
EM42	MSFC Advanced Manufacturing Group
ET30	MSFC Structural Strength Test Group
FEM	Finite element model
fps	Frames per second
ft-lbs	Foot Pounds
FWD	Forward or top end of test article
G_{12}	In-plane shear modulus
G_{13}, G_{23}	Transverse shear moduli in the axial and circumferential directions, respectively
gsm	grams per square meter
HS-DIC	High speed digital image correlation
IML	Inner mold line
in-lbf	Inch-Pound Force
JHA	Job hazard analysis
kips	1,000 lb
LaRC	Langley Research Center
lb	Pound
lbf	Pound force
lbf/min	Pound force per minute
LCS	Load control system
LS	Load sequence
LTAE	Load Test Annex East
M_{cr}	Linear critical buckling bending moment corresponding to the linear critical axial buckling load
MSFC	Marshall Space Flight Center
NDE	Nondestructive evaluation
NESC	NASA Engineering and Safety Center
OML	Outer mold line
P_{cr}	Linear critical buckling uniformly distributed axial compressive force obtained from perfect finite element model
P_{cr}^{NL}	Geometrically nonlinear critical buckling uniformly distributed axial compressive force obtained from finite element model with manufacturing shape imperfections
P_{cr}^{CL}	Linear buckling load of combined 90% axial compressive force and 10% bending moment obtained from perfect finite element model
psf	pounds per square foot
SBKF	Shell Buckling Knockdown Factor Project

TA	Test article
δ_{DxxxA}	Axial displacement measurements measured with or calculated from electronic displacement indicators

1.0 Introduction

It is well known that the buckling response of thin-walled cylindrical structures can be sensitive to geometric imperfections. The NASA Engineering and Safety Center (NESC) Shell Buckling Knockdown Factor Project (SBKF, NESC Assessment 07-010-E) has its goal to develop buckling design recommendations for a select class of composite launch-vehicle structures [1, 2]. This report describes the test and analysis results from the third SBKF cylindrical sandwich composite test article, which was designated SBKF-P3-CYL-CTA8.3 and herein is referred to as CTA8.3. This test was the third in a series of tests on sandwich composite cylinders that can be used to experimentally validate analysis methods, which in turn can be used to develop analysis-based shell buckling design guidelines for sandwich composite launch-vehicle cylindrical structures. CTA8.3 was an 8-foot diameter honeycomb core sandwich cylinder that was fabricated and tested at the Marshall Space Flight Center (MSFC). The primary objectives of this test were to interrogate the structural capability of the composite test article, and to verify the test-article design and analysis approach for cylinders subjected to axial compression and combined compression and bending loads.

Descriptions of the test-article design and test are given in Section 2. The modeling and analysis methods, as well as comparison of selected test results with predicted results are given in Section 3, and concluding remarks are presented in Section 4. References are listed in Section 5, drawings of CTA8.3 test hardware are given in Appendix A, and the shearography inspection report for CTA8.3 is presented in Appendix B.

2.0 Test Description

The test article and corresponding test system and facilities were designed and built for SBKF to enable the buckling testing of relevant launch-vehicle like thin-walled cylindrical structures (also known as *cylinders*). The 8-ft-diameter, 100-in. long CTA8.3 test article was designed by SBKF researchers at NASA Langley Research Center (LaRC) Structural Mechanics and Concepts Branch (D312) and was manufactured in an autoclave process at the Composite Technology Center by the Advanced Manufacturing Branch (EM42) at MSFC. The testing of CTA8.3 occurred on December 16–19, 2019 at MSFC in Building 4619 Load Test Annex East (LTAE) under the direction of the Structural Strength Test Group (ET30). A special-purpose test apparatus was designed and fabricated for the SBKF test effort. The test apparatus was designed to apply up to 1.5 million pounds of total force in axial compression, or combined compression and bending. In the tests described herein, a multichannel load control system (LCS) was used to apply the test loads and included load control and displacement control options. Several types of instrumentation and photographic/video systems were utilized during this test including strain gages, displacement transducers, load cells, and low-speed and high-speed digital image correlation (DIC, HS-DIC) techniques. This section gives a brief overview of the test objectives, test article, instrumentation, test facility, and test load cases. Additional details on the testing of CTA8.3 can be found in the Test Plan and Test and Checkout Procedure [3, 4].

2.1 Test Objectives

The CTA8.3 test article was the third composite test-article designed and tested as part the SBKF project. The test had the following primary objectives:

- Obtain test data to verify the predicted behavioral characteristics of the as-designed, as-built cylinder subjected to uniform axial compression loads, and combined axial compression and bending loads.
- Obtain test data for analysis tool and model validation.

2.2 Honeycomb Core Sandwich Composite Test Article

The test article was a honeycomb core sandwich composite shell constructed with carbon epoxy facesheet (IM7/8552-1) and aluminum core (Hexcel 3.1-1/8-0.0007N-5056 and Hexcel 8.1-1/8-0.002N-5056). The test article was designed to be representative of a "typical" composite launch-vehicle cylinder. However, it was not intended to be representative of any specific launch-vehicle structure.

2.2.1 Design

The CTA8.3 test article was designed to fail by global buckling rather than by a material strength failure or by local stability failures. As such, the maximum-strain material failure criterion was used, as were standard sandwich composite failure criteria to check for core shear failure, facesheet wrinkling, and facesheet dimpling as described in ref. [5]. Padups (additional plies in sandwich faces) at either end of the test article were designed to aid in load introduction by reducing the displacements and strains in the test article as it interfaced with much stiffer load-introduction fittings. The test-article design is shown using the fabrication drawing, Figure A-1 of Appendix A, where the as-manufactured cylinder included an extra 4 in. of manufacturing runouts at each end that were trimmed off after cure as indicated in Figure A-2 of Appendix A. The trimmed test article was potted in the metallic attachment rings (Figure A-3 of Appendix A) as shown in the assembly drawing (Figure A-4 of Appendix A).

The test article was a honeycomb core sandwich composite shell constructed with carbon epoxy faces (145 gsm Hexcel IM7/8552-1 prepreg) and aluminum core (Hexcel 3.1-1/8-0.0007N-5056 and Hexcel 8.1-1/8-0.002N-5056). All materials were treated as linear elastic orthotropic at room temperature. The material properties of the facesheet and core material systems are provided in Table 1 and 2 [5].

Table 1. Properties of carbon epoxy IM7/8552-1 material system

Property, Unit	E_{11}, Msi	E_{22}, Msi	ν_{12}	t_p, in.
Value	20.4	1.33	0.345	0.0054* 0.00694**

* FAW = 145 g/m^2
** FAW = 190 g/m^2

Table 2. Properties of 5056 aluminum honeycomb core

Property, Unit	Density, pcf	E_{11}, psi	E_{22}, psi	G_{12}, psi	G_{13}, psi	G_{23}, psi	σ_{11}, psi	σ_{13}, psi
Value	3.1	5.8	2.9	1.45	45,000	20,000	350* 260**	250* 200**
	8.1	15.66	7.83	3.915	143,000	51,000	1900* 1300**	945* 740**

* Typical
** Minimum

The quasi-isotropic five-ply faces had the acreage layup of $[30/\text{-}30/\overline{90}]_s$ and the core was 0.20 in. thick. A thin 0.06-psf Cytec FM 2009-1M adhesive film was used for the core-to-facesheet bond, and Henkel Hysol EA 9396.6MD epoxy paste adhesive was used for the core splices. In the first 10.0 in. from the top or forward end (FWD) and bottom or aft (AFT) end (all dimensions are subsequently given in the trimmed configuration of Figure A-2, i.e., after removing 4.0 in. from each end relative to Figure A-1), both the inner mold line (IML) and outer mold line (OML) padups comprised four plies interleaved with the acreage plies resulting in the layup shown in the bottom row of Table 3. Also, in the first 10.0 in. from both ends, heavier Hexcel 8.1-1/8-0.002N-5056 aluminum core was used based on the recommandtion of CTA8.2 test review. In the next 4 in. (i.e., between 10 and 14 in. from the ends), the IML and OML layups were the same as in the first 10 in., with the same padup plies, but the acreage core of Hexcel 3.1-1/8-0.0007N-5056 aluminum honeycomb was used. One padup ply was dropped from the IML and OML facesheets at 14.0, 16.0, 18.0, and 20.0 in. from both ends. The laminations corresponding to each of the above ranges are also shown in Table 3. Since only one 45° or –45° padup ply would be dropped at a time, the facesheet laminations between 14.0 and 20.0 in. stations were not symmetric. However, the IML and OML facesheet laminations were symmetric about the core midsurface. Furthermore, since the test article was built on a constant diameter tool, the additional thickness of the padups was built up to the OML only as shown in Figure A-1. The remaining acreage region between the padups was 60 in. long.

The approximate weight of the trimmed test article without the metallic load introduction fixtures was 158 lb. The nominal weight of the design was estimated at 157 lb; however, this estimate did not include Henkel Hysol EA 9396 paste epoxy adhesive used to fill in honeycomb core splices up to 0.25 in. in width.

Table 3. Layups in Acreage and Padup Regions of IML Facesheet (padup plies in bold)

CTA8.3 cylinder sections measured from cylinder ends, in.	IML facesheet layup, degrees
Beyond 20.0 (Acreage)	[30/-30/90/-30/30]
18.0 to 20.0	[30/-30/**45**/90/-30/30]
16.0 to 18.0	[30/-30/**45**/90/-30/**-45**/30]
14.0 to 16.0	[30/-30/**45**/90/**45**/-30/**-45**/30]
0 to 14.0	[30/**-45**/-30/**45**/90/**45**/-30/**-45**/30]

2.2.2 Initial Damage State of Test Article Evaluation

Prior to potting, nondestructive evaluation (NDE) was performed to inspect the test article by shearography and structured-light scanning. From the NDE of the test article, a total of 16 anomalies were detected and measured. The map of indication locations from the shearography and the structured-light scanning is shown in Figure 1 and the size of each anomaly in the form of h (axial) x w (circumferential) is listed in Table 4. A summary of the anomalies detected in CTA8.3 is given in the Shearography Inspection Report (Appendix B).

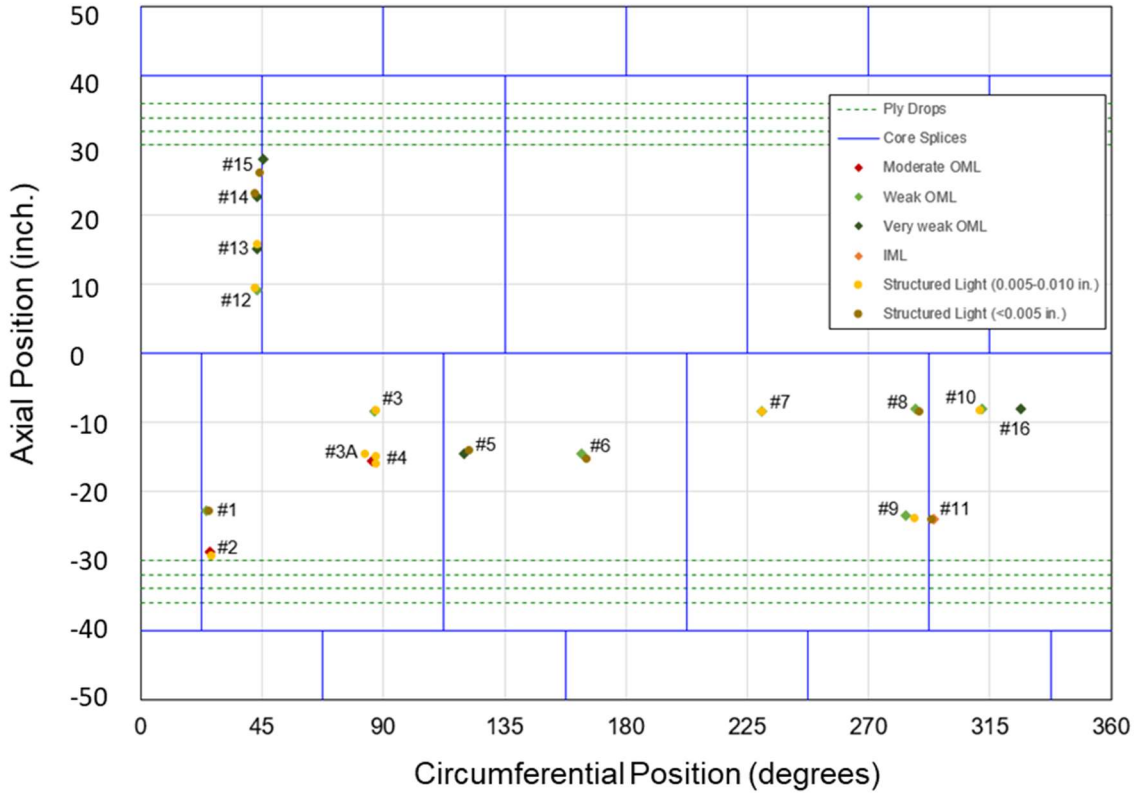

Figure 1. The map of anomalies of CTA 8.3 test article.

Table 4. Description of Damage in CTA8.3 Test Article

Indication	Surface	Size (h x w), in.	Description/Signal Strength	Damage Depth, in.
1	OML	0.70 x 0.81	Weak	-0.003
2	OML	1.49 x 0.71	Moderate	-0.01
3	OML	1.70x1.02	Very weak	-0.009
3a	OML	1.64 x 1.03	Weak	-0.008
4	OML	3.25 x 0.86	Moderate	-0.006
5	OML	0.93 x 0.83	Very weak	-0.003
6	OML	0.95 x 0.88	Weak	-0.003
7	OML	1.08 x 1.05	Weak	-0.005
8	OML	1.19 x 0.81	Weak	-0.003
9	OML	1.53 x 1.18	Weak	-0.009
10	OML	1.39 x 0.93	Weak	-0.007
11	IML	1.43 x 0.98	Weak	-0.001
12	OML	N/A	Very weak	-0.005
13	OML	N/A	Very weak	-0.01
14	OML	N/A	Very weak	-0.004
15	OML	N/A	Very weak	-0.003
16	OML	0.70 × 0.81	Weak	-0.009

2.2.3 Structured Light Geometry Measurement

The structured-light scanning geometry measurements of OML and IML surfaces were used to determine the geometric imperfections of the test article, and later used in the development of the as-built finite element models (FEMs). These measurements were taken with the test article potted inside the attachment rings that interface with the test fixture, that is, the measurements were taken with the test article in the *as-manufactured* condition. The midsurface radial position of the test article was obtained by averaging the OML and IML radial measurements and is shown in Figure 2; the midsurface imperfection is indicated by the variation in the radial position. The thickness (and subsequently thickness imperfections) was obtained by taking the difference between the OML and IML radial imperfection measurements and is shown in Figure 3. When interpreting Figures 2 and 3, it is important to consider that both results include the presence of the padup plies at the axial coordinates below –30.0 in. and above +30.0 in., and do not show end sections that are potted within the metallic attachment rings. The midsurface imperfection indicated by Figure 2 shows a global radial pattern where the radius varies in a mostly circumferential pattern around the cylinder. However, a more axially localized region with smaller radial position can also be identified around the circumference at the axial coordinate of approximately 15.0 to 30.0 in. The thickness plot in Figure 3 shows the thicker padup sections at the top and bottom, but other than that does not show a pattern as obvious as that in the radial imperfection plot. Rather, only a few localized thickness variations, primarily along the axial direction between radial stations 300° and 340° and several other locations, are seen.

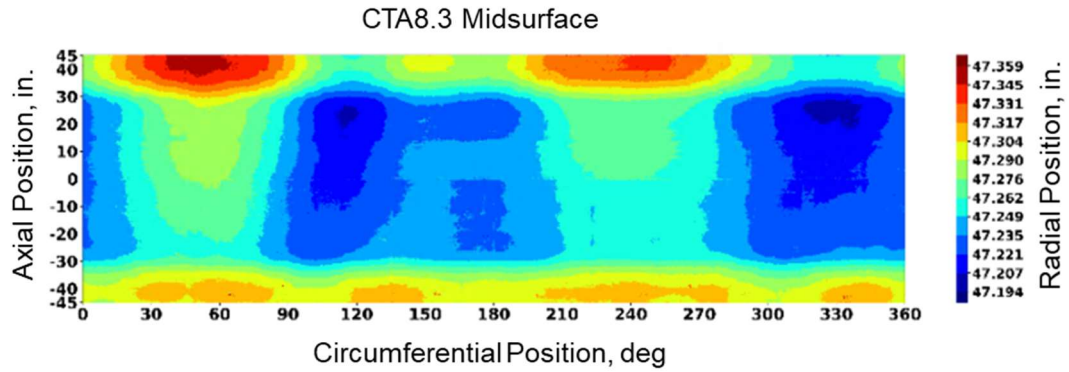

Figure 2. Unrolled image of midsurface radial position.

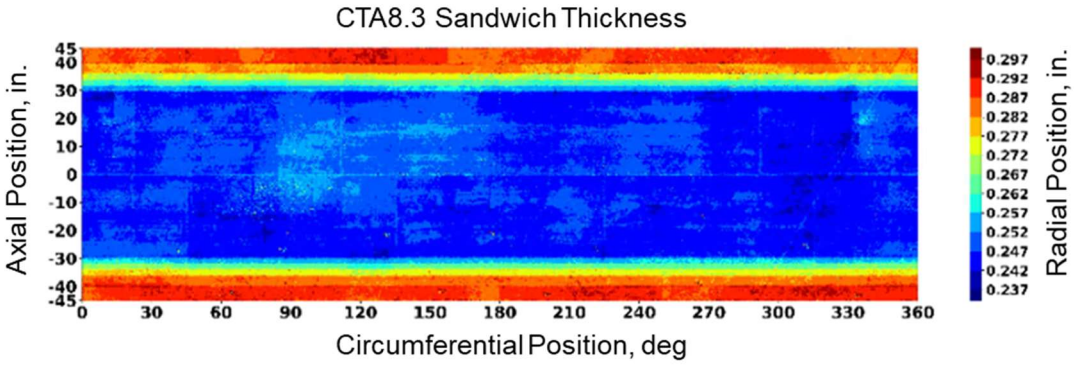

Figure 3. Unrolled image of the measured thickness.

2.3 Test Facility

The testing was conducted at MSFC in the LTAE in Building 4619 under the direction of the ET30 Structural Strength Test Group. The test assembly, shown in Figure 4, was designed, analytically verified, and fabricated to meet SBKF test objectives described in an earlier section. The test assembly is a self-reacting load system composed of an upper and lower load spider, 16 load struts, upper and lower transition sections, the test-article assembly, and eight load lines. Each load line consists of a hydraulic cylinder, a 4.0-in.-diameter loading rod (pipe), a load cell, and attachment hardware. The load lines can be controlled independently in load control or stroke (displacement) control to apply uniform compression or combined compression and bending with a maximum load capability of 1.5 million pounds of axial compression force and 80,000 pounds of axial tension force. For the testing described herein, the load lines were able to accommodate a stroke of ±2.0 in. during testing. Provisions were made to remove any test-assembly dead weight from the test article prior to beginning each load sequence (LS); the load at which the dead weight removed is referred to herein as tare load. The MSFC design drawings for the components that comprise the test assembly are indicated in Figure 4 and drawings 90M12375 and 90M12370 are given as Figures A-5 and A-6 in Appendix A.

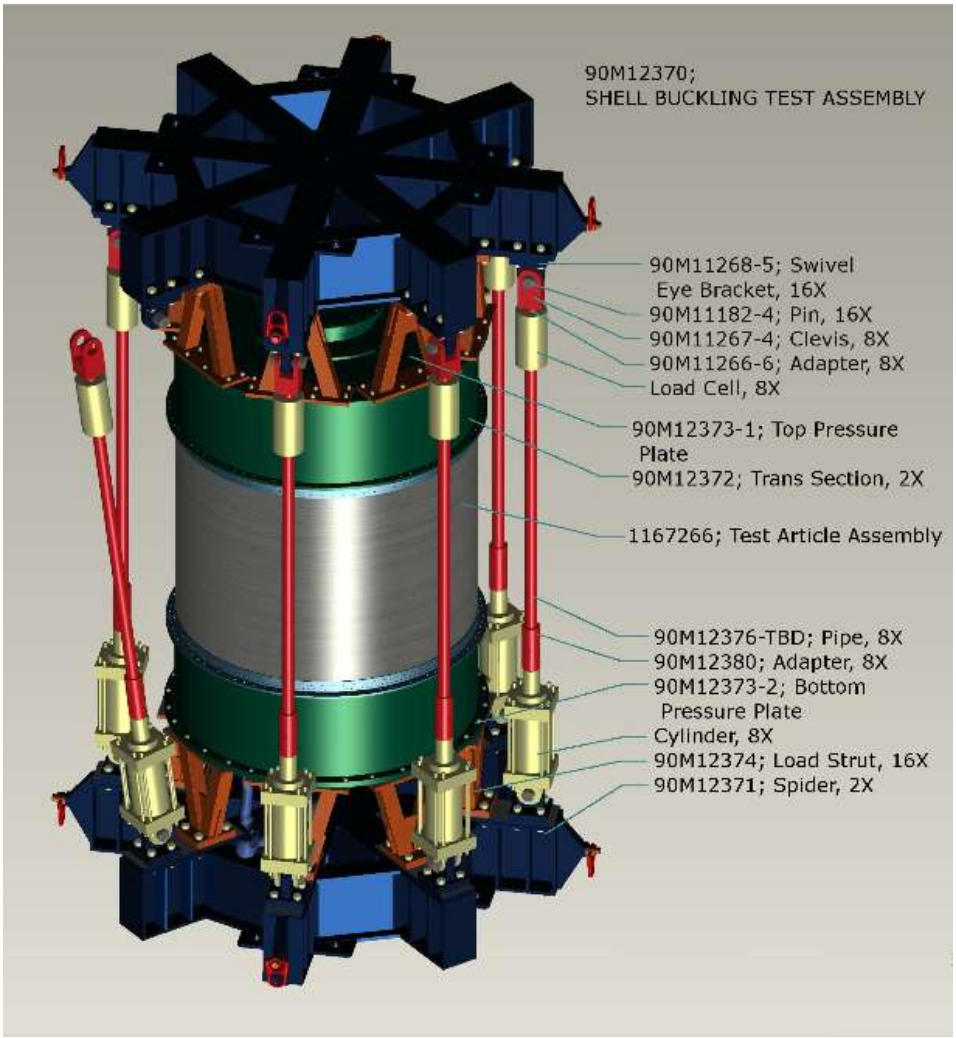

Figure 4. Test assembly at MSFC.

2.4 Test Article Installation and Alignment

During assembly, the test article was oriented to a known, specific circumferential orientation for testing, as shown in Figure 5. Having a known orientation was important for these tests so that the structural response, including strains and displacements, could be compared with the predictions. Knowing the orientation is particularly important during tests that apply a bending moment because the maximum compression load introduced into the test article needed to occur in a specific known location on the cylinder. It was also required that the top and bottom loading fixtures be aligned with each other so that the load lines were vertical and oriented parallel with the test-article longitudinal axis. Proper alignment of the load lines ensured that unwanted torsion or bending loads were negligible during testing. The attachment rings were indexed with respect to the test-article circumferential reference location to ensure proper alignment in the built-up test assembly, as specified in the assembly drawing of Figure A-4 in Appendix A. The ring alignment, specifically relative circumferential index angle, parallelism, and perpendicularity were verified and documented per the assembly procedure.

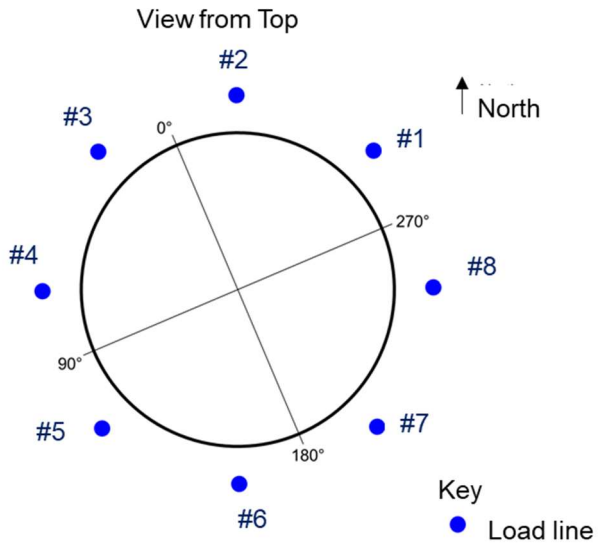

Figure 5. Test article orientation relative to the load-line layout and numbering convention, top view.

The test article interfaced with the test assembly through a set of attachment rings (Figure A-3 of Appendix A). The attachment rings were one-piece, 6061-T6 aluminum rings with an inner and outer attachment flange that interfaced with the transition section (90M12372) and a 1.05-in.-wide machined groove in which the test article was seated. The attachment rings weigh approximately 358 lb each. The test article was placed in the groove, potted, and mechanically fastened in place according to the assembly procedure described in Figure A-4 of Appendix A. Micor Micorox® Standard Grout potting material was used. The potting material was not considered a primary axial loading transfer mechanism between the attachment rings and the test article, as release agent Loctite® Frekote 700-NC™ was applied to the IML and OML surfaces of the cylinder seated in the attachment ring as well as the attachment ring channel as part of the process of installing CTA8.3 in the rings. The purpose of adding this release agent was to improve the uniformity of the load introduction by making the bond weak and allowing the test-article ends to be in bearing contact at the "bottom" of the end-ring grooves. The potting material, however, was considered a part of the primary mechanism against the out-of-plane rotation of the CTA8.3 cylinder wall at the boundary. Furthermore, mechanical fasteners (bolts through both end-ring flanges, the potting material, and the test articles) were used as a handling and a failsafe feature.

2.5 Test-Article Instrumentation

Several types of instrumentation and photographic/video systems were utilized during this test that included electrical-resistance strain gages, displacement transducers, load cells, and low-speed and high-speed digital image correlation techniques. All measured data obtained during the test were synchronized with respect to time, load signal from load line #1, and a triangle wave signal to enable posttest data synchronization.

2.5.1 Displacement Measurements

Axial, radial, and tangential displacement measurements of the test article, test-article attachment rings, and actuators were obtained during the test. Table 5 summarizes descriptions of displacement measurements and Figures 6, 7, and 8 show measurement locations. Actuator displacements were measured using displacement transducers attached to the hydraulic cylinders

and were used as position control sensors for the test control system. Additionally, the axial displacement of the AFT and FWD attachment rings were used to calculate the end-shortening of the test article (i.e., the relative axial motion of the FWD attachment ring with respect to the AFT attachment ring). As such, the axial displacement of both attachment rings was measured at four locations spaced 90° apart around the circumference. Additionally, the axial displacement of the AFT ring was measured at one location on the OML attachment ring flange as shown in Table 5 and Figures 6, 7, and 8. This additional OML measurement was used to calculate rotation (about the tangent) of the AFT attachment ring.

The axial end-shortening of the test article was calculated at the four axial-measurement locations around the circumference (0°, 90°, 180°, and 270°) as follows:

$$0°: \delta_{D000A} = \delta_{D113A} - \delta_{D317A}$$

$$90°: \delta_{D090A} = \delta_{D114A} - \delta_{D318A}$$

$$180°: \delta_{D180A} = \delta_{D115A} - \delta_{D319A}$$

$$270°: \delta_{D270A} = \delta_{D116A} - \delta_{D320A}$$

where δ_{D113A}, δ_{D114A}, δ_{D115A}, δ_{D116A} and δ_{D317A}, δ_{D318A}, δ_{D319A}, δ_{D320A} correspond to electronic displacement indicator (EDI) measurements on the AFT and FWD attachment rings, respectively, and δ_{D000A}, δ_{D090A}, δ_{D180A}, δ_{D270A} correspond to the derived end-shortening displacements at the 0°, 90°, 180°, and 270° locations, respectively. These end-shortening displacement equations presume that the measured AFT and FWD displacements are negative downward.

The radial displacement in the proximity of the predicted global buckling event origination was measured using four additional EDIs installed on the IML side of the cylinder. These EDIs, designated D425R through D428R, were installed as shown in Figures 6 and 7.

The out-of-plane deflections of the test article and attachment rings were measured at 13 locations. Specifically, displacements were measured at the midlength (see note in Table 5 for additional midlength location information) of the test article and on both attachment rings at four circumferential locations spaced 90° apart.

The relative rotational movement of the AFT and FWD attachment rings were monitored by measuring the tangential motion of both attachment rings at one circumferential location as shown in Table 5 and Figures 6, 7, and 9. These tangential displacement measurements were used to characterize the rotation of the rings about the cylinder axis (tangent to the edge of the attachment ring).

Table 5. Description of EDIs.

EDI ID[+]	Measurement range	Measurement description	Sign convention
D101R, D102R, D103R, D104R, D309R, D310R, D311R, D312R	±1.0 in.	Radial displacement on the AFT and FWD attachment rings to characterize local or rigid-body displacements	Outward radial displacement: +
D205R[#], D206R[#], D207R[#], D208R[#]	±2.0 in.	Radial displacement at the midlength of the test article	Outward radial displacement: +
D113A*, D114A*, D115A*, D116A*	±1.0 in.	Axial displacement of the AFT attachment ring on the IML flange (for test-article end-shortening and ring-rotation calculations)	Upward axial displacement: +
D317A*, D318A*, D319A*, D320A*	±2.0 in.	Axial displacement of the FWD attachment ring on the IML flange (for test-article end-shortening calculation)	Upward axial displacement: +
D121T, D322T	±1.0 in.	Tangential displacement at a point on the AFT and FWD attachment rings to characterize relative torsional displacements	Displacement in positive theta: +
D123S	±1.0 in.	Radial displacement on the AFT and attachment ring to characterize ring clevis rotation or deformation	Outward radial displacement: +
D124O	±1.0 in.	Axial displacement of the AFT attachment ring on the OML flange (for test-article end-shortening and ring-rotation calculations)	Upward axial displacement: +
D425R, D426R, D427R, D428R	±1.0 in.	Radial displacement at selected locations associated with the global buckling onset	Outward radial displacement: +

[#]All midlength radial EDIs were placed 0.5 in. down (in negative axial direction) and 0.4 in. in the negative circumferential direction (clockwise from top).

*All axial EDIs were placed 0.4 in. to the positive circumferential direction (counterclockwise from top).

[+]Unless otherwise indicated, EDIs were installed per SBKF-P3-CYL-CTA8.3 and the test plan.

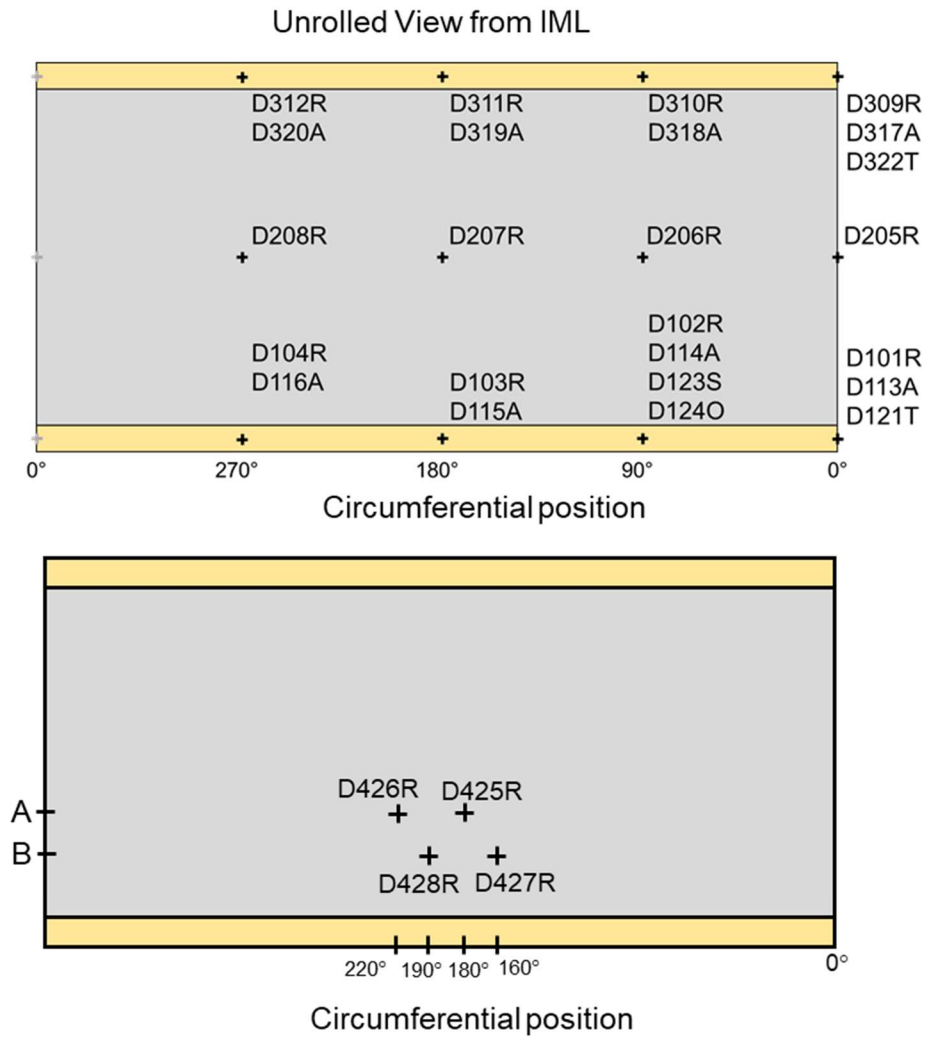

Nomenclature: DXYYZ

D – Displacement sensor
X – axial position indicator
- 1 – AFT ring
- 2 – test article midlength
- 3 – FWD ring

YY – indicator number
Z – orientation
- R – Radial
- A – Axial
- T – Tangential (hoop)
- S – Supplementary radial (for ring rotation)
- O – Axial OML

Key

EDI location

Test article

Attachment ring

Figure 6. Locations of EDI displacements, unrolled view from IML.

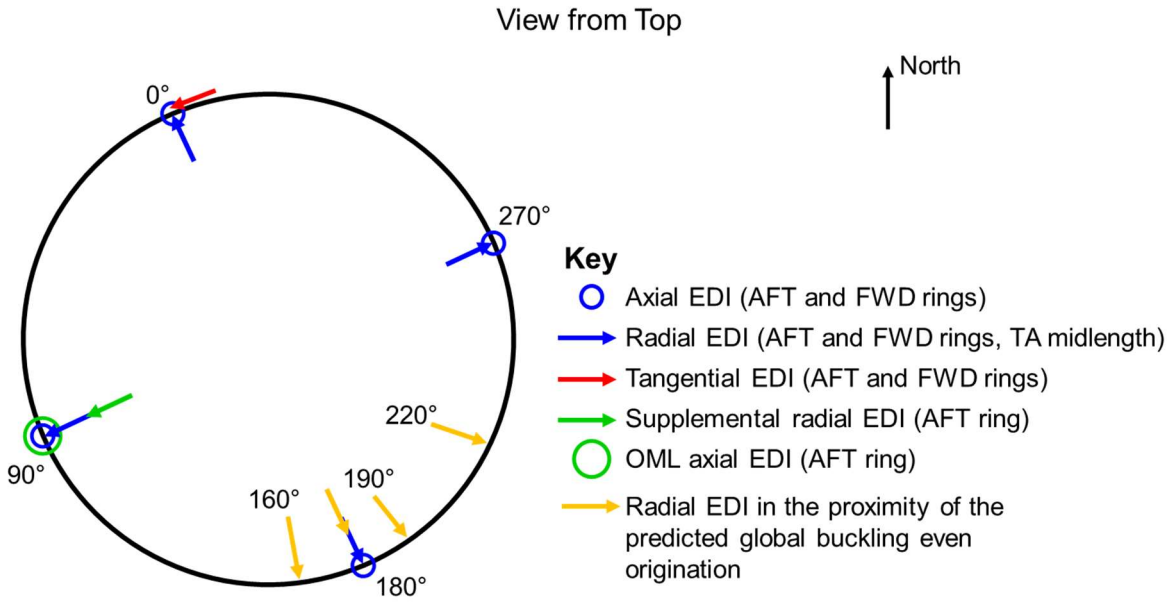

Figure 7. EDI locations from the top of the test article.

(Arrows in the direction of positive displacement.)

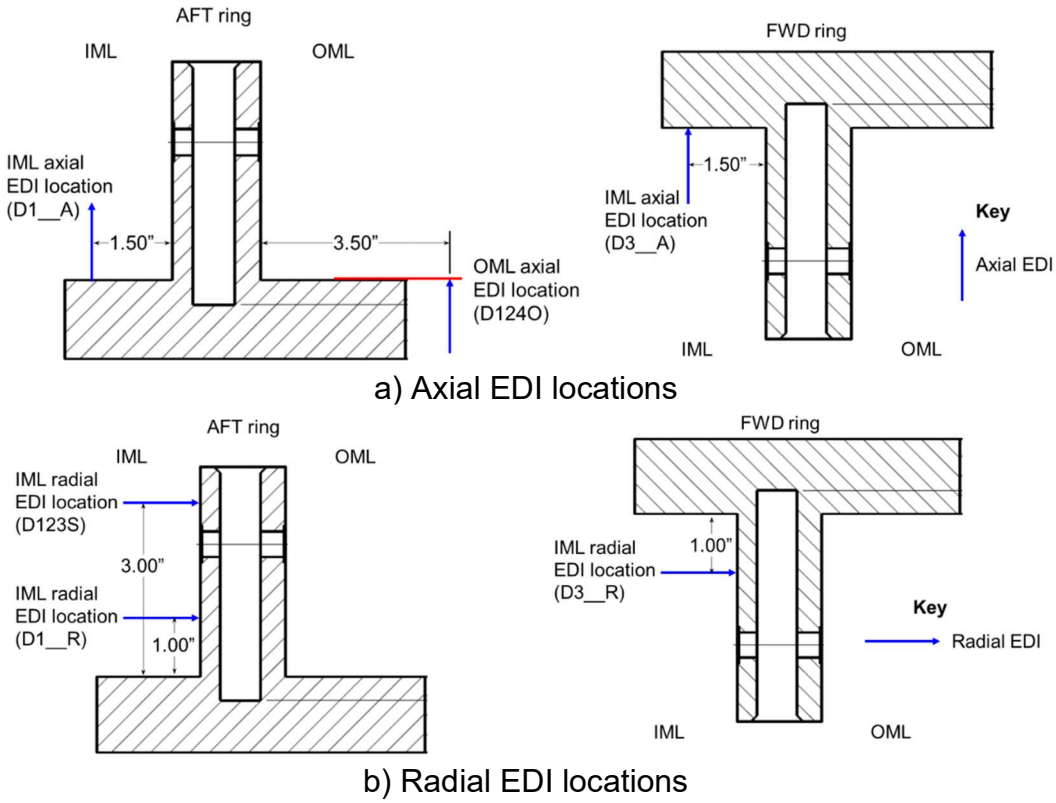

Figure 8. Cross-sectional view of the EDI locations on the attachment rings.

(Arrows in the direction of positive displacements.)

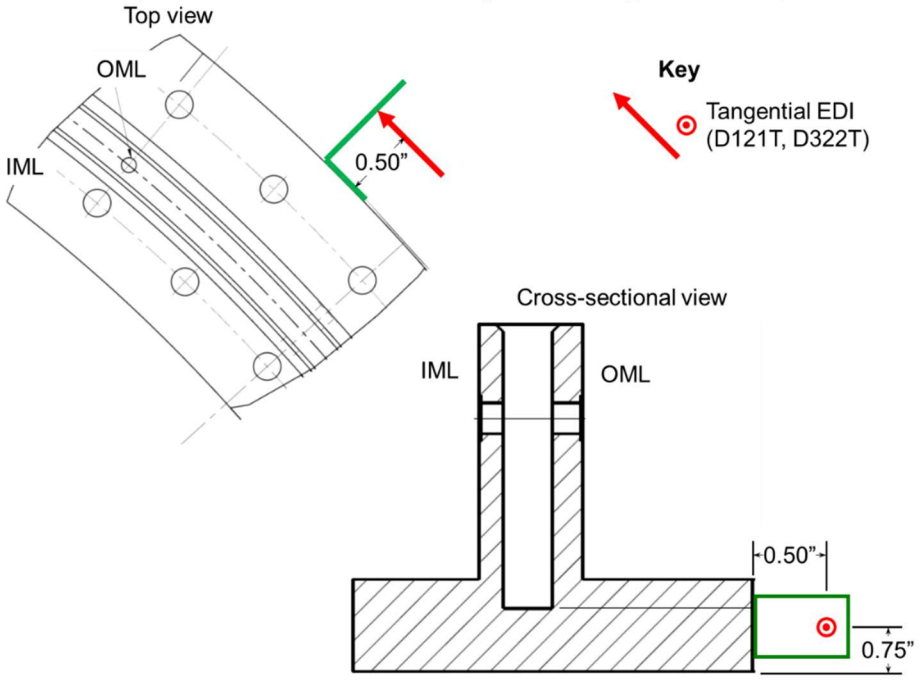

Figure 9. Tangential EDI location on the attachment rings.

(Arrows in the direction of positive displacements.)

2.5.2 Conventional Strain Measurements

Strain measurements on the test article were required to assess the uniformity of the load introduction into the shell during loading and to monitor the local strain response of the test article during the prebuckling and post-buckling phases of testing. Two types of Micro-Measurements gage were used: CEA-06-187UW-350 (uniaxial) and CEA-06-125UT-350 (biaxial). The gage patterns and labeling convention are specified in Figure A-7 of Appendix A. Each gage was installed per manufacturer's recommendations for graphite-epoxy composite material and MSFC standard installation procedures.

2.5.3 Three-Dimensional Digital Image Correlation (3D-DIC)

A photogrammetry technique, known as 3D-DIC was implemented during the test. This photogrammetry technique is used to track pixel subsets through a series of images, from the undeformed to deformed state, and to measure displacements from which test article shape and strains can be calculated. This technique utilizes pairs of cameras, in a stereo configuration, to view and monitor the speckle pattern as it changes during loading and deformation. In order to do so, the outer surface of the entire test article had a high contrasting speckle pattern of black speckles on a white background applied. Using such a high-contrasting speckle pattern, along with proper lighting, camera system calibrations, and camera parameters (e.g., sensor resolution direction, focus, lens aperture settings and depth-of-field, and relative angles (stereo angles) per system) allows high quality, high resolution displacement and strain data to be generated. Figure 10 shows the location of the global 3D low-speed camera systems, which were equally spaced around the circumference of the OML (centered approximately 45° apart), with an overlapping field-of-view in order to fully capture and characterize the behavior of the test article. All of the DIC systems were synchronized and the synchronization was verified and documented. The analog load signal

from load line #1 and a triangle-wave synchronization signal were recorded for posttest correlation.

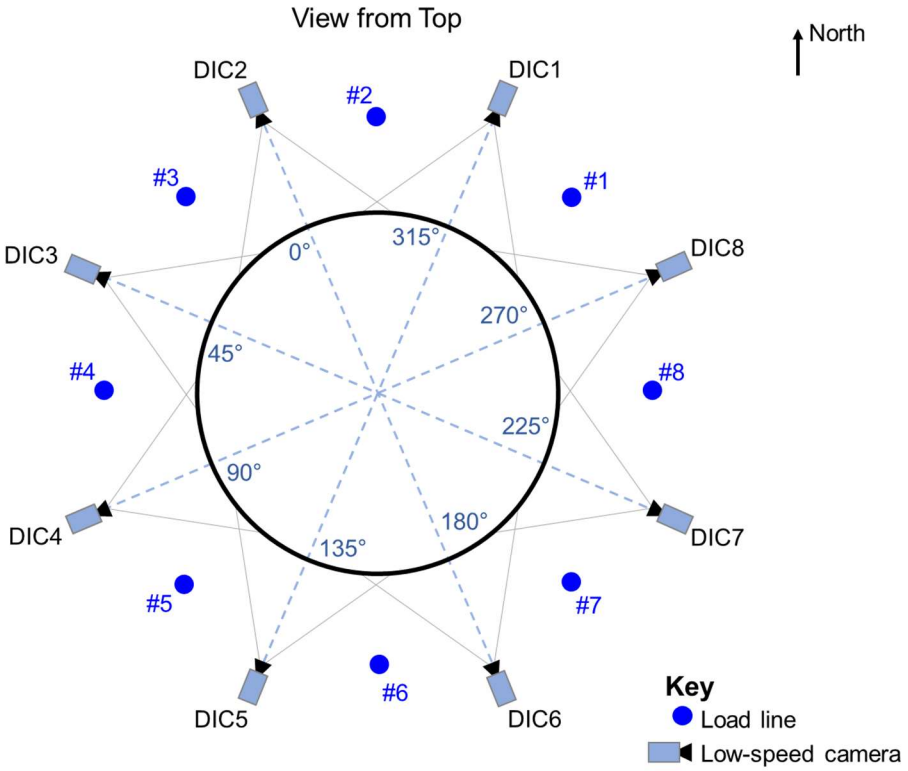

Figure 10. The low-speed DIC system.

2.5.4 Low-speed Digital Image Correlation (Global)

A total of eight low-speed camera pairs were set-up and continuously recorded at 5 frames per second (fps) during the test around the circumference of the OML, centered approximately 45° apart, for the global view of the test article. Each field-of-view was approximately 100 in. tall (including the test-article acreage and the attachment rings) and 70° wide (allowing for 15° overlap between adjacent systems). Due to the resolution of the low-speed cameras, and the field-of-view, a speckle size of 0.1 to 0.2 in. was ideal for the best resolution of measurement; however, due to the high-speed camera systems with the lower resolution (to be discussed later), a speckle size of 0.3 to 0.5 in. was used on the test article (as discussed below) and a speckle size of 0.15 to 0.25 in. was used on the attachment rings.

2.5.5 Low-Speed Digital Image Correlation (Local)

Based upon the NDE inspection discussed in Section 2.2.2, a number of damage locations were detected, measured, and reported. Two specific locations were selected and marked as key areas of interest, and these were centered at the 86.5° and 163.5° circumferential OML locations, both in AFT acreage region of the test article, as shown in Figure 11. Therefore, two additional low-speed camera pairs were set-up at these locations to more closely monitor the behavior of the test article at these locations. Due to the size of the damage areas, a much smaller field-of-view was required in order to maximize the resolution of the local systems. However, with a smaller field-of-view, a smaller speckle pattern was also required, and a new technique was implemented in order to measure the local areas of interest without jeopardizing the correlation and accuracy of

the global DIC systems. This was achieved by using an optimized multiscale pattern via local greyscale variation as discussed in [6], where the local pattern was embedded within the larger global pattern, as shown in Figure 12. This approach allowed for the low-speed local DIC systems to be utilized alongside the low-speed and high-speed global DIC systems without correlation and accuracy issues. For local system 1 (86.5°) and local system 2 (163.5°), the field-of-view was approximately 24 in. tall and 22.5° wide, with a speckle size of 0.04 to 0.06 in., approximately a factor of 10 smaller than the global speckle pattern size.

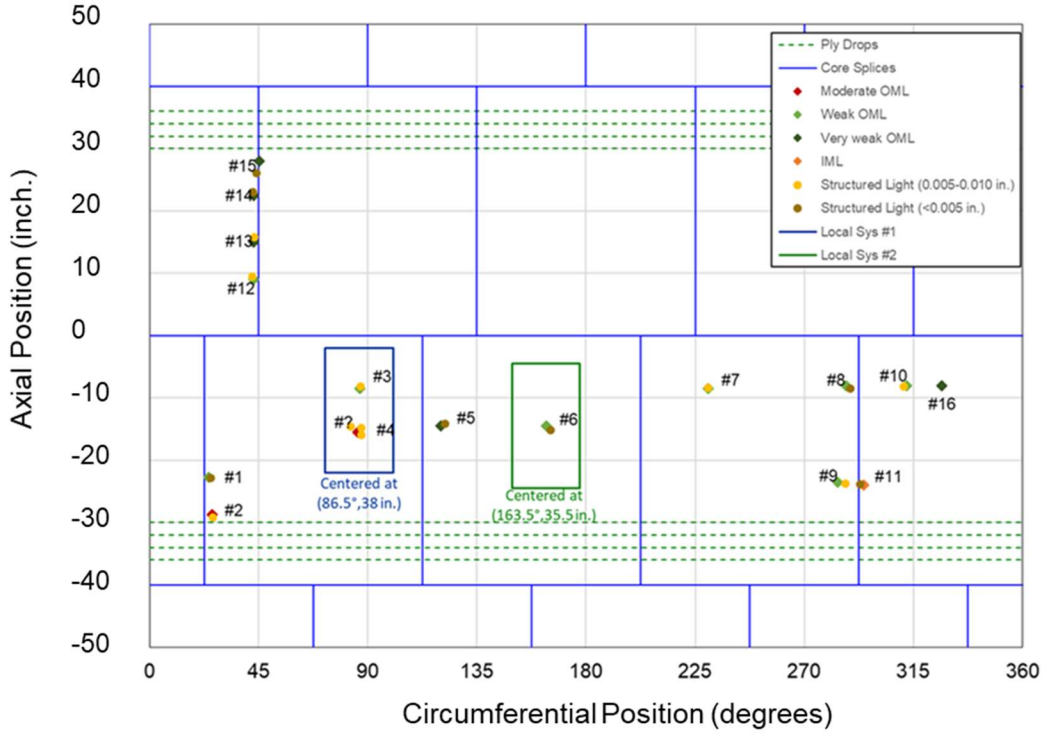

Figure 11. Two local regions for local DIC systems.

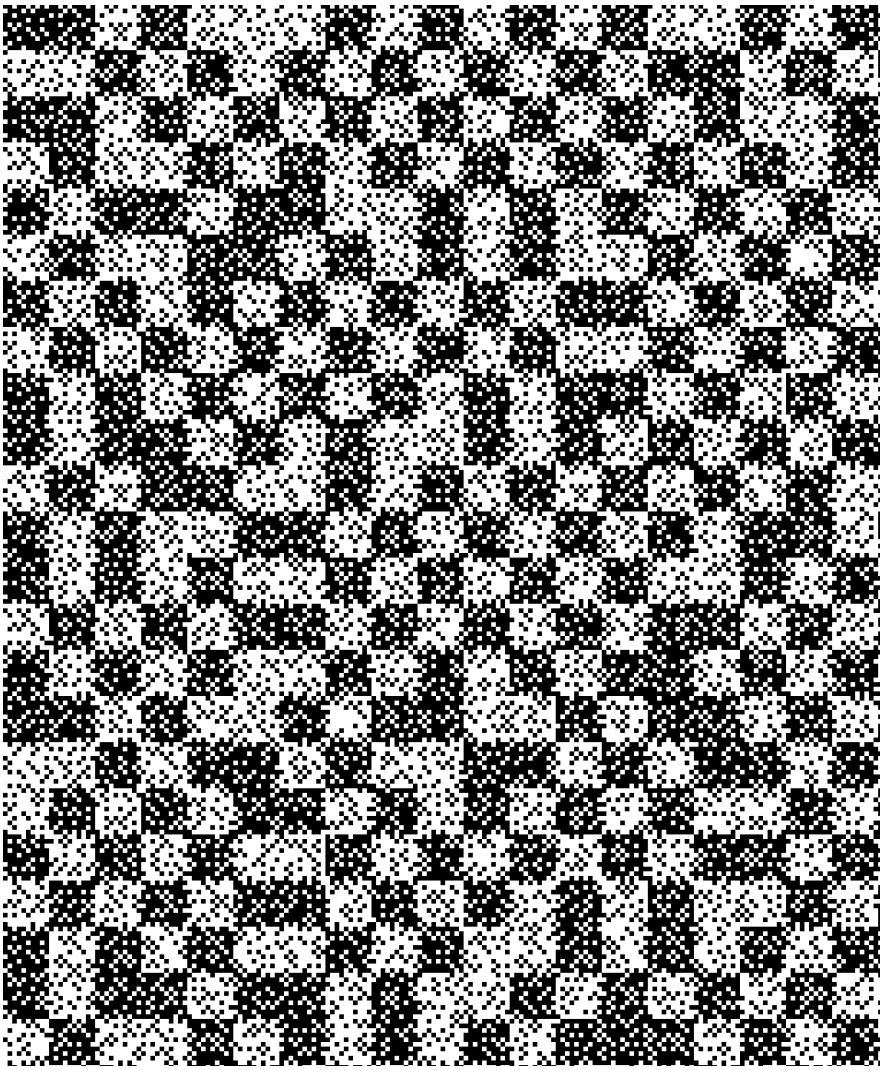

Figure 12. Optimized global-local DIC pattern.

2.5.6 High-Speed Digital Image Correlation (Global)

A total of six high-speed camera pairs were set-up around the circumference of the OML, as shown in Figure 13, to continuously record at 10,000 frames per second (fps). Due to the number of camera pairs and the test stand (camera mounting locations), the camera systems were not equally spaced; however, they were still located in positions to allow for overlapping coverage between adjacent camera systems. The high-speed camera systems were available to measure the buckling displacement response of the entire OML during all load sequences, but were primarily used during the failure load sequence to capture the dynamic failure event and damage initiation and propagation. Due to the high frame rate (10,000 fps) and the limited resolution of the cameras, the optimal speckle size was larger than that of the low-speed systems, 0.45 to 0.65 in. In order to properly correlate over the entire field-of-view, and provide the best accuracy and data for all DIC systems (low-speed global and local), the speckle pattern of the global low-speed system was adjusted to be closer to the lower end of the optimal size for the global high speed, which is why a global speckle pattern of 0.3 to 0.5 in. was chosen for the entire acreage of the test article. The

cameras were synchronized with respect to each other and had a common, manual, post-trigger recording function (i.e., all data from before the trigger and no data after the trigger). The cameras were programmed to acquire images at a rate of 10,000 fps in a continuous write-overwrite loop, with a total recording time of approximately 2.55 sec, to each camera's buffer until the high-speed DIC operator triggered the manual post-trigger recording after the buckling or failure event.

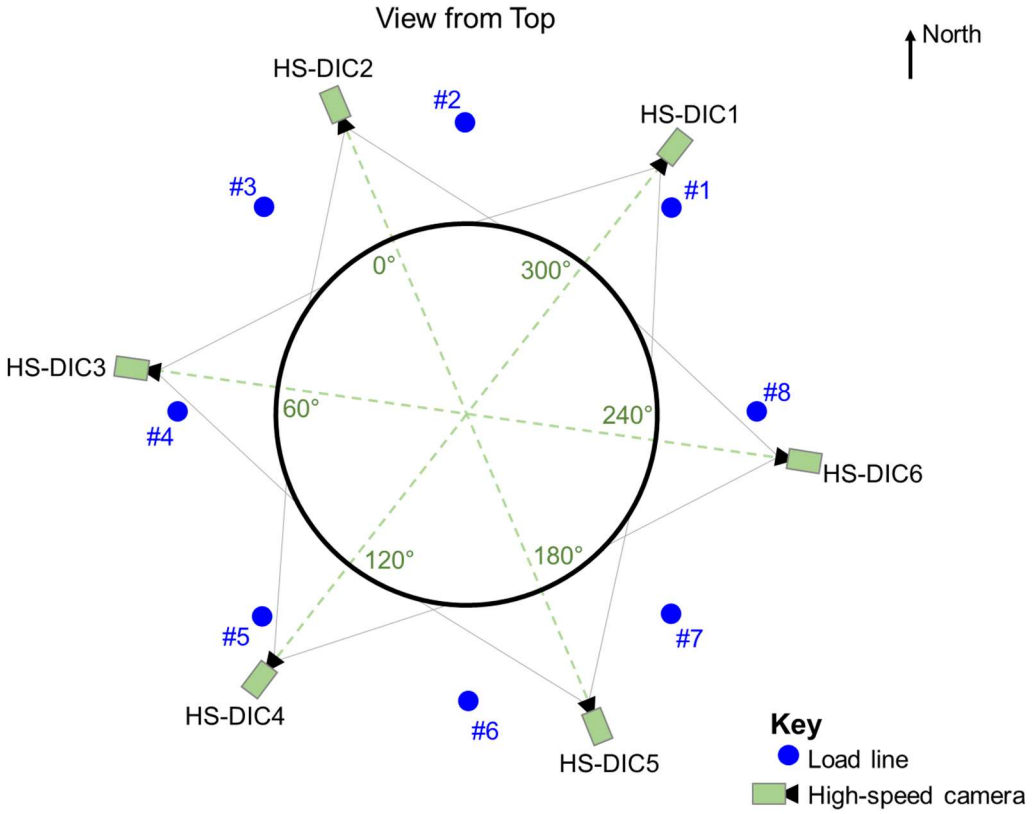

Figure 13. The high-speed DIC system.

2.6 Test Load Sequence

A series of eight load sequences (LS1 – LS6, LS9, and LS 12) were performed during testing. Seven of the load sequences, LS1 – LS6 and LS9, were considered subcritical in that the load levels applied to the test article were not expected to cause buckling or structural failure. The combined compression and bending load sequence to failure was designated LS12. The predicted axial linear buckling load, P_{cr}, for the idealized, geometrically perfect test article with the attachment rings and nominal material properties subjected to a uniform compression load is 554,716 lbf, and was obtained using an eigen analysis. Using geometrically nonlinear analyses of the FEM with the as-manufactured measured radial and thickness imperfections and the entire test apparatus gave a predicted axial buckling load, P_{cr}^{NL}, equal to 507,240 lbf. For the purposes of this test, the critical bending moment, M_{cr}, was defined as the bending moment that produces a maximum compressive line load that is the same as the uniform line load at P_{cr} for uniform axial compression. As such, M_{cr} was calculated to be 13.31×10^6 in-lbf. Each load sequence is defined in terms of a percentage of the critical axial compression load, P_{cr}, and percentage of critical bending moment, M_{cr}. As will be discussed, the final critical load sequence, LS12, was combined

loading for 90% axial compression and 10% bending in the 180° direction. The predicted linear buckling load for LS12, P_{cr}^{CL}, was 499,246 lbf, and the predicted nonlinear buckling load was 462,410 lbf for LS12 using the FEM with the as-manufactured measured radial and thickness imperfections and the entire test apparatus. The eight load sequences are described in the following sections.

2.6.1 Load Sequence 1 (LS1): 0.2 P_{cr}

A uniform axial compression load was applied to the test article to a maximum of 110,944 lbf total applied load in the load steps specified in Table 6, and then unloaded to tare load. A pause occurred at the end of each load step to assess the behavior of the test article and test system. The purposes of this test were to exercise the test apparatus, remove slack from the system, check for uniformity of load application, and check the functionality of all control and measurements systems involved in the test. The control system loaded the test article in load control up to the designated total load with an average load rate of 7,500 lbf/min based on the total load (an average load rate of 937.5 lbf/min in each load line). Actuator loads for LS1 are summarized in Table 6.

Table 6. Actuator Loads (lbf) for LS1

Load Step	Actuator #1	Actuator #2	Actuator #3	Actuator #4	Actuator #5	Actuator #6	Actuator #7	Actuator #8	Total Load
#1	2,774	2,774	2,774	2,774	2,774	2,774	2,774	2,774	22,192
#2	5,547	5,547	5,547	5,547	5,547	5,547	5,547	5,547	44,376
#3	8,321	8,321	8,321	8,321	8,321	8,321	8,321	8,321	66,568
#4	11,094	11,094	11,094	11,094	11,094	11,094	11,094	11,094	88,752
#5	13,868	13,868	13,868	13,868	13,868	13,868	13,868	13,868	110,944

2.6.2 Load Sequence 2 (LS2): 0.4 P_{cr}

A uniform axial compression load was applied to the test article in LS2. The test load was increased to a maximum of 221,888 lbf compression in the load steps specified in Table 7, and then unloaded to tare load. A pause occurred at the end of each load step to assess the behavior of the test article and test system. The purposes of this test were to exercise the test system, and to assess that the applied loads and strains match closely the desired input loads and predicted strains and displacements. The control system loaded the test article in load control up to the designated total load with an average load rate of 15,000 lbf/min based on the total load (an average load rate of 1,875 lbf/min in each load line). Actuator loads for LS2 are summarized in Table 7.

Table 7. Actuator Loads (lbf) for LS2

Load Step	Actuator #1	Actuator #2	Actuator #3	Actuator #4	Actuator #5	Actuator #6	Actuator #7	Actuator #8	Total Load
#1	5,547	5,547	5,547	5,547	5,547	5,547	5,547	5,547	44,376
#2	11,094	11,094	11,094	11,094	11,094	11,094	11,094	11,094	88,752
#3	16,641	16,641	16,641	16,641	16,641	16,641	16,641	16,641	133,128
#4	22,189	22,189	22,189	22,189	22,189	22,189	22,189	22,189	177,512
#5	27,736	27,736	27,736	27,736	27,736	27,736	27,736	27,736	221,888

2.6.3 Load Sequence 3 (LS3): 0.2 P_{cr} + 0.2 M_{cr} (Maximum Compression at the 0° Circumferential Location)

A combined axial and bending load was applied to the test article in LS3. The test load was a total load of 110,944 lbf (total of all load line loads) with maximum compression load occurring at the 0° circumferential location in the load steps specified in Table 8 and then unloaded to tare load. A pause occurred at the end of each load step to assess the behavior of the test article and test system. The purposes of this test were to exercise the test system in the presence of combined axial compression and bending (bending in which maximum compression loads were applied to the test article between load lines 2 and 3), and to assess that the applied loads and strains match closely the desired input loads and predicted strains and displacements. The control system loaded the test article in load control up to the designated total load with an average load rate of 15,000 lbf/min based on the total load (an average load rate of 1,875 lbf/min in each load line). Actuator loads for LS3 are summarized in Table 8.

Table 8. Actuator Loads (lbf) for LS3

Load Step	Actuator #1	Actuator #2	Actuator #3	Actuator #4	Actuator #5	Actuator #6	Actuator #7	Actuator #8	Total Load
#1	3,546	4,637	4,637	3,546	2,002	910	910	2,002	22,190
#2	7,091	9,274	9,274	7,091	4,003	1,820	1,820	4,003	44,376
#3	10,637	13,912	13,912	10,637	6,005	2,730	2,730	6,005	66,568
#4	14,182	18,549	18,549	14,182	8,007	3,640	3,640	8,007	88,756
#5	17,728	23,186	23,186	17,728	10,008	4,550	4,550	10,008	110,944

2.6.4 Load Sequence 4 (LS4): 0.2 P_{cr} + 0.2 M_{cr} (Maximum Compression at the 90° Circumferential Location)

A combined axial and bending load was applied to the test article in LS4. The test load was a total load of 110,944 lbf (total of all load line loads) with maximum compression load occurring at the 90° circumferential location in the load steps specified in Table 9 and then unloaded to tare load. A pause occurred at the end of each load step to assess the behavior of the test article and test system. The purposes of this test were to exercise the test system in the presence of combined axial compression and bending (bending in which maximum compression loads were applied to the test article between load lines 4 and 5), and to assess that the applied loads and strains match closely the desired input loads and predicted strains and displacements. The control system loaded the test article in load control up to the designated total load with an average load rate of 15,000 lbf/min based on the total load (an average load rate of 1,875 lbf/min in each load line). Actuator loads for LS4 are summarized in Table 9.

Table 9. Actuator Loads (lbf) for LS4

Load Step	Actuator #1	Actuator #2	Actuator #3	Actuator #4	Actuator #5	Actuator #6	Actuator #7	Actuator #8	Total Load
#1	910	2,002	3,546	4,637	4,637	3,546	2,002	910	22,190
#2	1,820	4,003	7,091	9,274	9,274	7,091	4,003	1,820	44,376
#3	2,730	6,005	10,637	13,912	13,912	10,637	6,005	2,730	66,568
#4	3,640	8,007	14,182	18,549	18,549	14,182	8,007	3,640	88,756
#5	4,550	10,008	17,728	23,186	23,186	17,728	10,008	4,550	110,944

2.6.5 Load Sequence 5 (LS5): 0.2 P_{cr} + 0.2 M_{cr} (Maximum Compression at the 180° Circumferential Location)

A combined axial and bending load was applied to the test article in LS5. The test load was a total load of 110,944 lbf (total of all load line loads) with maximum compression load occurring at the 180° circumferential location in the load steps specified in Table 10 and then unloaded to tare load. A pause occurred at the end of each load step to assess the behavior of the test article and test system. The purposes of this test were to exercise the test system in the presence of combined axial compression and bending (bending in which maximum compression loads are applied to the test article between load lines 6 and 7), and to assess that the applied loads and strains match closely the desired input loads and predicted strains and displacements. The control system loaded the test article in load control up to the designated total load with an average load rate of 15,000 lbf/min based on the total load (an average load rate of 1,875 lbf/min in each load line). Actuator loads for LS5 are summarized in Table 10.

Table 10. Actuator Loads (lbf) for LS5

Load Step	Actuator #1	Actuator #2	Actuator #3	Actuator #4	Actuator #5	Actuator #6	Actuator #7	Actuator #8	Total Load
#1	2,002	910	910	2,002	3,546	4,637	4,637	3,546	22,190
#2	4,003	1,820	1,820	4,003	7,091	9,274	9,274	7,091	44,376
#3	6,005	2,730	2,730	6,005	10,637	13,912	13,912	10,637	66,568
#4	8,007	3,640	3,640	8,007	14,182	18,549	18,549	14,182	88,756
#5	10,008	4,550	4,550	10,008	17,728	23,186	23,186	17,728	110,944

2.6.6 Load Sequence 6 (LS6): 0.2 P_{cr} + 0.2 M_{cr} (Maximum Compression at the 270° Circumferential Location)

A combined axial and bending load was applied to the test article in LS6. The test load was a total load of 110,944 lbf (total of all load line loads) with maximum compression load occurring at the 270° circumferential location in the load steps specified in Table 11 and then unloaded to tare load. A pause occurred at the end of each load step to assess the behavior of the test article and test system. The purposes of this test were to exercise the test system in the presence of combined axial compression and bending (bending in which maximum compression loads are applied to the test article between load lines 1 and 8), and to verify that the applied loads and strains match closely the desired input loads and predicted strains and displacements. The control system loaded the test article in load control up to the designated total load with an average load rate of 15,000 lbf/min based on the total load (an average load rate of 1,875 lbf/min in each load line). Actuator loads for LS6 are summarized in Table 11.

Table 11. Actuator Loads (lbf) for LS6

Load Step	Actuator #1	Actuator #2	Actuator #3	Actuator #4	Actuator #5	Actuator #6	Actuator #7	Actuator #8	Total Load
#1	4,637	3,546	2,002	910	910	2,002	3,546	4,637	22,190
#2	9,274	7,091	4,003	1,820	1,820	4,003	7,091	9,274	44,376
#3	13,912	10,637	6,005	2,730	2,730	6,005	10,637	13,912	66,568
#4	18,549	14,182	8,007	3,640	3,640	8,007	14,182	18,549	88,756
#5	23,186	17,728	10,008	4,550	4,550	10,008	17,728	23,186	110,944

2.6.7 Load Sequence 9 (LS9): 0.54 P_{cr} + 0.06 M_{cr} (maximum compression at the 180° circumferential location Load)

A combined axial and bending load (90% compression, 10% bending) was applied to the test article in LS9. The test load was increased to a total load of 299,546 lbf (total of all load line loads) with maximum compression load occurring at the 180° circumferential location in the load steps specified in Table 12 and then unloaded to tare load. A pause occurred at the end of each load step to assess the behavior of the test article and test system. The purpose of this test was to exercise the test system in the presence of combined axial compression and bending in the same ratio and maximum compression direction as the final load sequence (bending in which maximum compression loads are applied to the test article between load lines 6 and 7), and to assess that the applied loads and strains match closely the desired input loads and predicted strains and displacements. It is also to remove slack and settle the test article in the same loading ratio and direction as the final critical load sequence. The control system loaded the test article in load control up to the designated total load with an average load rate of 15,000 lbf/min based on the total load (an average load rate of 1,875 lbf/min in each load line). Actuator loads for LS9 are summarized in Table 12.

Table 12. Actuator Loads (lbf) for LS9

Load Step	Actuator #1	Actuator #2	Actuator #3	Actuator #4	Actuator #5	Actuator #6	Actuator #7	Actuator #8	Total Load
#1	6,048	5,775	5,775	6,048	6,434	6,706	6,706	6,434	49,926
#2	12,095	11,549	11,549	12,095	12,867	13,413	13,413	12,867	99,848
#3	18,143	17,324	17,324	18,143	19,301	20,119	20,119	19,301	149,774
#4	24,190	23,099	23,099	24,190	25,734	26,826	26,826	25,734	199,698
#5	30,238	28,873	28,873	30,238	32,168	33,532	33,532	32,168	249,622
#6	36,285	34,648	34,648	36,285	38,601	40,239	40,239	38,601	299,546

2.6.8 Load Sequence 12 (LS12): Test to Failure under 1.08 P_{cr} + 0.12 M_{cr}, (maximum compression at the 180° circumferential location)

A combined 90% axial and 10% bending load with maximum compression load occurring at the 180° circumferential location was applied to the test article in LS12 until a failure of the test article resulting in a significant drop in load occurred; the programmed load sequence is summarized in Table 13. A pause occurred at the end of each load step to assess the behavior of the test article and test system. During the test, CTA8.3 was loaded without a pause after load step 6 was completed, until failure occurred. The control system loaded the test article in load control up to the designated total load with an average load rate of 15,000 lbf/min based on the total load (an average load rate of 1,875 lbf/min in each load line).

Table 13. Actuator Loads (lbf) for LS12

Load Step	Percent Critical Line Load	Actuator #1	Actuator #2	Actuator #3	Actuator #4	Actuator #5	Actuator #6	Actuator #7	Actuator #8	Total Load
#1	20%	12,095	11,549	11,549	12,095	12,867	13,413	13,413	12,867	99,848
#2	30%	18,143	17,324	17,324	18,143	19,301	20,119	20,119	19,301	149,774
#3	40%	24,190	23,099	23,099	24,190	25,734	26,826	26,826	25,734	199,698
#4	50%	30,238	28,873	28,873	30,238	32,168	33,532	33,532	32,168	249,622
#5	60%	36,285	34,648	34,648	36,285	38,601	40,239	40,239	38,601	299,546
#6	70%	42,333	40,423	40,423	42,333	45,035	46,945	46,945	45,035	349,472
#7	80%	48,381	46,197	46,197	48,381	51,468	53,652	53,652	51,468	399,396
#8	90%	54,428	51,972	51,972	54,428	57,902	60,358	60,358	57,902	449,320
#9	100%	60,476	57,747	57,747	60,476	64,335	67,065	67,065	64,335	499,246
#10	110%	66,523	63,521	63,521	66,523	70,769	73,771	73,771	70,769	549,168
#11	120%	72,571	69,296	69,296	72,571	77,202	80,477	80,477	77,202	599,092
Facility max load		187,500	187,500	187,500	187,500	187,500	187,500	187,500	187,500	1,500,000

3.0 Results And Discussion

After CTA8.3 was fabricated and mounted in the attachment rings, the as-manufactured geometry was measured using structured-light scanning. The FEM of CTA 8.3 was developed to obtain the converged mesh and the boundary conditions of CTA8.3 test. The geometric imperfections of CTA8.3, including as-manufactured radial imperfection and thickness variation, were then incorporated into the FEM to develop pretest predictions for each load sequence.

The physical testing of CTA8.3 took place at MSFC from December 16, 2019 through December 19, 2019. The first load sequence, LS1, was conducted on December 16, 2019 and the final failure load sequence, LS12, was completed on December 19, 2019. During subcritical cases, test data were obtained and the structural response of the test frame and CTA8.3 was observed. The measured load-displacement response and strain data of CTA8.3 for each subcritical case were compared with the predicted pretest analysis results. Because no unexpected failures were observed during the subcritical tests, only LS12 will be thoroughly discussed herein.

In this section, first, the pretest predicted buckling and failure response of CTA8.3 obtained from the FEM with the as-manufactured radial and thickness imperfections are compared with the experimental test results. Second, posttest analyses that were performed to investigate anomalous behavior of the test article that was observed in the EDI and DIC data during the tare loading and load sequences are discussed. Third, the implementation into FEMs of different radial imperfection shapes that were measured at different stages of the test procedure is explained. Finally, the comparison of posttest analysis of the global FEM and test data are discussed.

3.1 Finite Element Model with Measured CTA8.3 Geometric Imperfection

A finite element model, which consisted of the test article and the test fixture, was developed to predict the prebuckling and postbuckling of CTA 8.3 [7]. Abaqus S4R shell elements were used to model the CTA8.3 test article and the attachment rings. This model is herein referred to as the global FEM. For the mesh of global FEM, the element size was 0.5 in. in the axial direction and

0.5° (or approximately 0.41 in.) in the circumferential direction. This resulted in approximately 154,000 elements and 932,000 degrees of freedom (DoFs). For test-analysis comparisons, the FEM of the test fixture was developed using Abaqus S4R shell elements, T3D2 truss, and B31 beam elements and tied to the global FEM. The bottom nodes of the lower spider fixture were attached via kinematic constraints to a reference node located on the cylinder axis. The bottom reference node was fixed, effectively simulating the clamped boundary condition of the lower spider fixture. For each loading sequence, axial loads were applied at the bottom end of the truss elements, simulating the load lines, putting them in tension. The global FEM with the test fixture and CTA8.3 is shown in Figure 14.

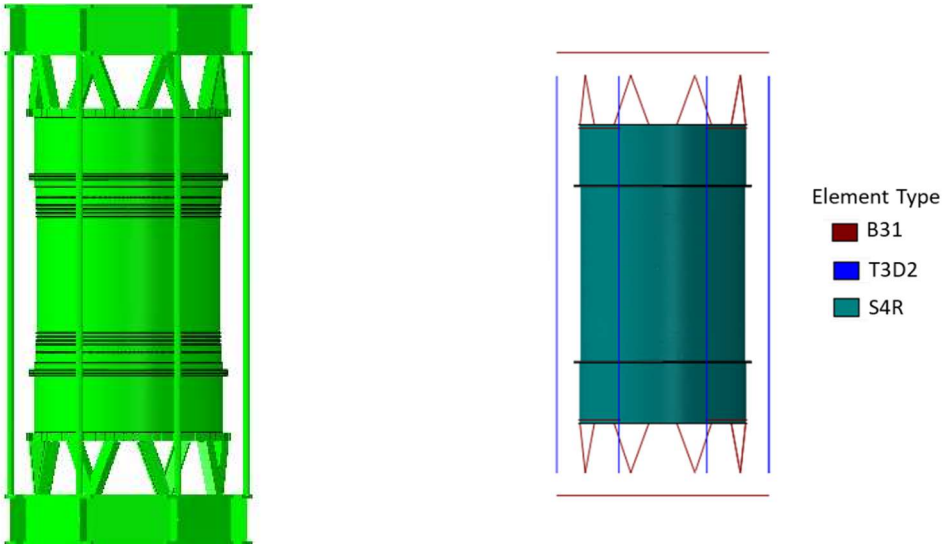

a) Represented CTA8.3 and the fixture b) The global FEM with test fixture

Figure 14. Test setup and global FEM for CTA8.3.

For FEMs with radial imperfections, the as-measured geometric imperfections and shell-thickness variation were imposed on the global FEM. The Python script Py_TIGIRS [8] was used to modify the nominal geometry of the global FEM to implement both radial and shell thickness imperfections. The processed radial imperfection contour plot of CTA8.3 with the combined radial and shell thickness imperfection values calculated using Py_TIGIRS are shown in Figure 15. These as-manufactured imperfections can be compared with the measured radial imperfections of Figure 2. Including both the radial and thickness imperfections in numerical models has been demonstrated to improve the agreement between analysis predictions and the experimentally observed response in both prebuckling and buckling-initiation behavior [9, 10]. Nonlinear buckling analyses were performed on the FEM using a general static solver preload step followed by a transient dynamic step to capture buckling and postbuckled response.

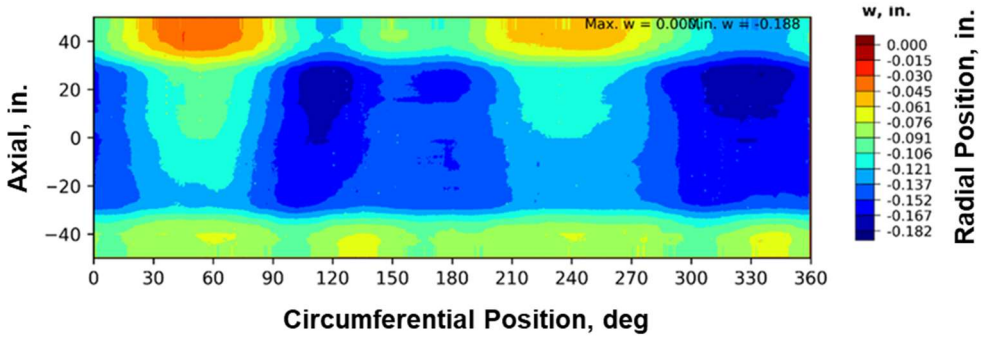

Figure 15. CTA8.3 as-manufactured imperfection contour plot contains combined radial and shell thickness imperfections.

The comparisons of the predicted global response and the failure load of the FEM and test results are discussed for the final combined 90% axial compression and 10% bending loading case, LS12. Predicted linear critical buckling load of combined axial compressive force and bending moment obtained from the perfect FEM is defined as P_{cr}^{CL}. During LS12, CTA8.3 failed with the total applied load 432.0 kips, i.e., during load step 8, at 86.4% of P_{cr}^{CL}. The failure occurred approximately 27 in. from the midline and near the 240° circumferential location. The failure location is pictured in Figure 16. After buckling initiated, material failure followed and propagated around the circumference of the cylinder from the edges of the dimple; as it was propagating around the circumference, the material failure moved from the buckling initiation axial position to the axial position of the last padup ply drop (30 in. from the midline). Test data suggest that the damage present in CTA8.3 prior to testing did not influence the failure mode or behavior of the test article.

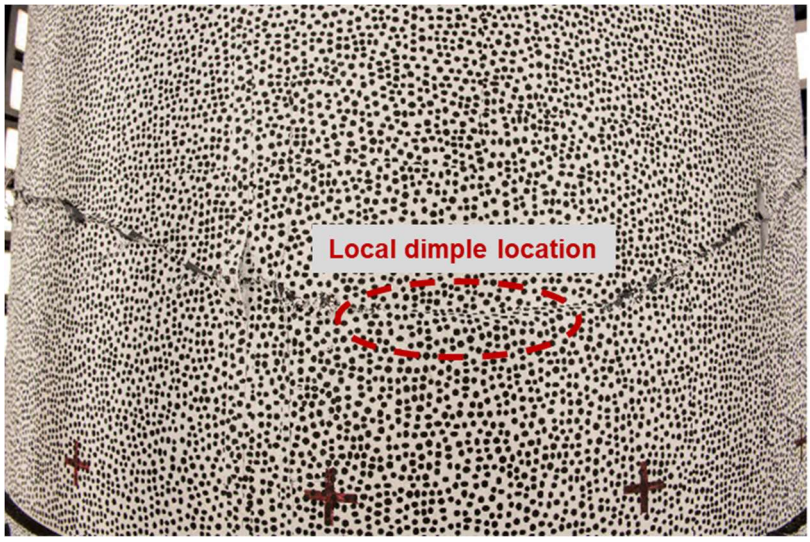

Figure 16. Final failure location at 240° location.

The CTA8.3 predicted LS12 failure load obtained from the FEM with as-manufactured imperfection and nonlinear transient analysis was 462.4 kips, which is 7% higher than the failure

load observed from the test. The test and predicted total applied load versus end-shortening response of each pair of load lines with test data are shown in Figures 17 through 20. The dotted lines represent the test results and the solid lines represent FEM predictions obtained from the nonlinear transient dynamic analysis. As shown in these figures, the axial displacements of load lines 6 and 7 show the largest axial displacement and the axial displacements of load lines 2 and 3 show the smallest axial displacement as expected because the maximum compression load was applied to the test article at the 180° circumferential location.

From Figures 17 through 20, it can also be seen that as the test article was loaded, an anomalous nonlinear flattening response was observed in the axial displacement of each load line. This anomalous behavior in each load line continued until the middle of load step 1, which was to 10% of P_{cr}^{CL}. In other words, the associated displacement was not proportional to the applied load as expected. This nonlinearity may be attributed at least in part to the excess movement (slop) at lower load levels of the pins that connect the hydraulic jacks and load lines to the upper and lower spiders. After 10% of P_{cr}^{CL}, the excess slop in the test fixture may have been removed. The load versus end-shortening response of each pair of load lines shows a linear response for the rest of LS12 until the buckling failure of the test article. As seen in Figures 17 through 20, the finite-element-analysis-predicted total applied load versus end-shortening responses of each pair of load lines were linear and coincided with each other from the initial loading until the buckling event; the predicted and test-measured slopes were consistent after the anomalous response seen during load step 1 of the test.

In addition to the nonlinear behavior at the beginning of the load sequence, some of the load line pairs did not have the similar total applied load versus displacement responses. For example, there is an offset between the curves for lines 2 and 3 after the anomalous behavior. During the test, the responses for load lines 1 and 4 tracked together well. On the other hand, there was a large deviation in the total applied load versus displacement response for load lines 2 and 3, specifically that L3 displaced approximately 0.025 in. more than L2. Load line pairs 5-8 and 6-7 show the relatively small differences in offset displacement of 0.004 in. and 0.002 in., respectively, and even less for load line pair 1-4. The offsets in paired load lines may be attributed to anomalous behavior of the upper test hardware observed during the test that is discussed in the next section.

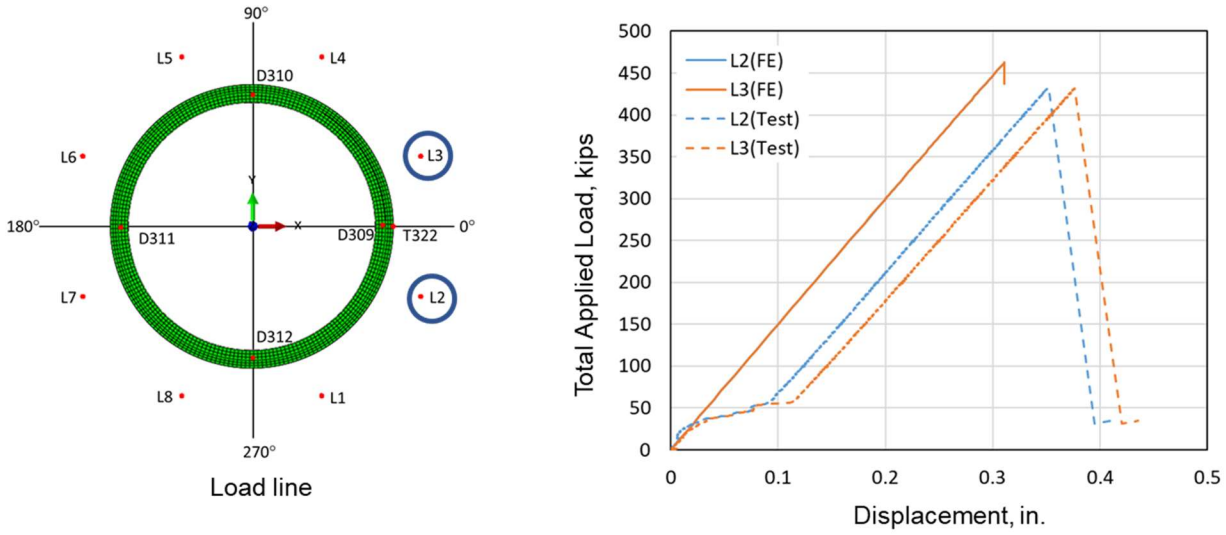

Figure 17. The predicted load versus end-shortening curves of FEM and test data (Load lines 2 and 3).

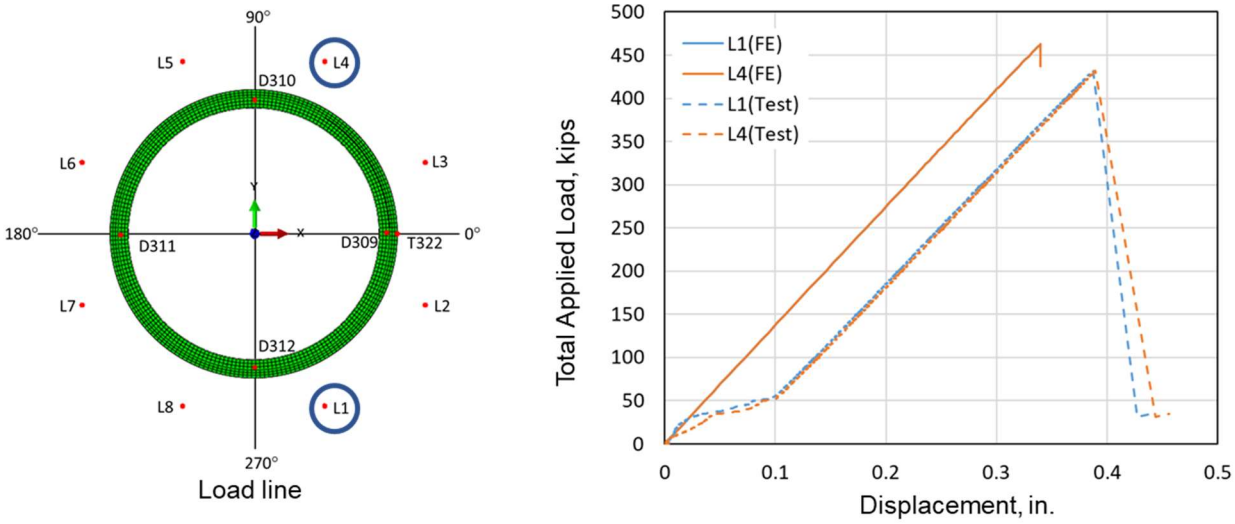

Figure 18. The predicted load versus end-shortening curves of FEM and test data (Load lines 1 and 4).

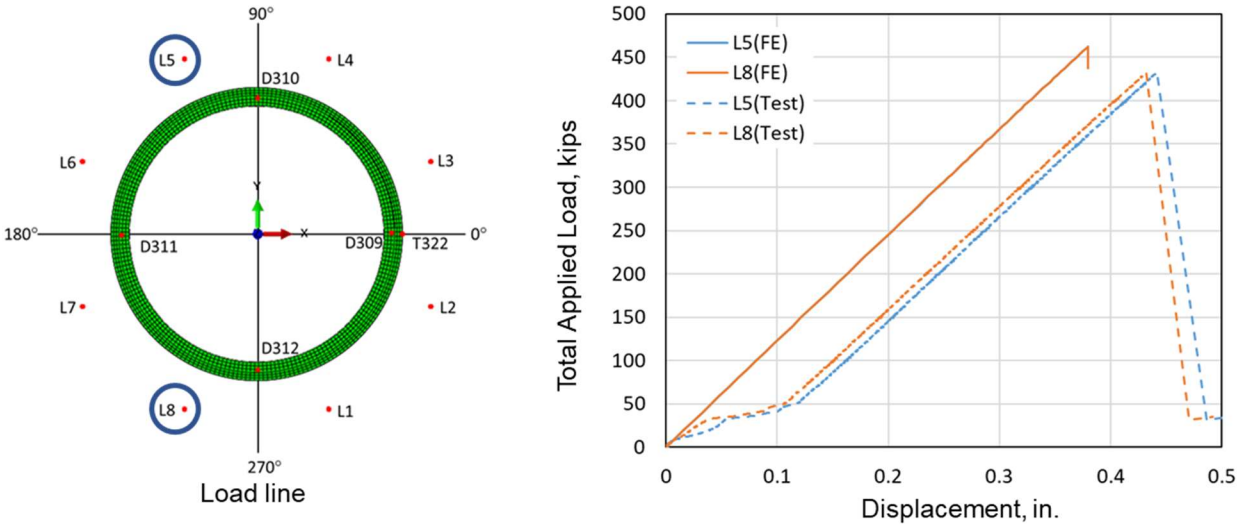

Figure 19. The predicted load versus end-shortening curves of FEM and test data (Load lines 5 and 8).

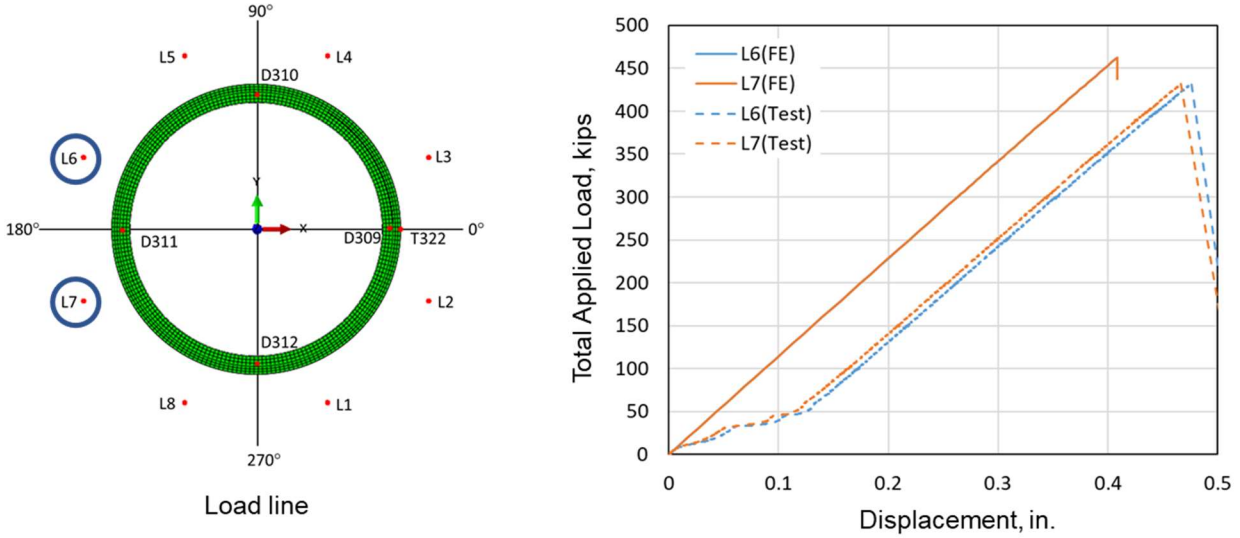

Figure 20. The predicted load versus end-shortening curves of FEM and test data (Load lines 6 and 7).

The predicted total applied load versus average axial end-shortening response of CTA8.3 (the average of δ_{D000A}, δ_{D090A}, δ_{D180A}, and δ_{D270A}) are shown in Figure 21. The average axial end-shorting response of CTA8.3 shows better agreement with test data compared to the end-shorting response of each load line, which suggests that the anomalous behavior of the upper test hardware and excess movement in the pins caused much of the discrepancy between the measured and predicted end-shorting response of each load line.

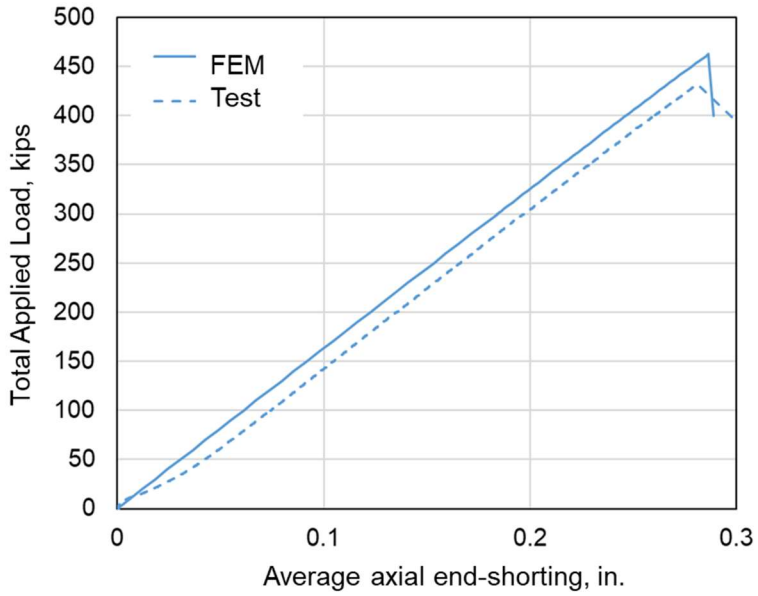

Figure 21. The tested and predicted total load versus average axial end-shortening measured at the attachment rings.

As seen in Figure A-7 of Appendix A, the axial strains were measured on the IML and OML surface every 45° at axial positions 29, 31, 33, 35, and 38 in. above and below the midline. The IML and OML axial strains measured from back-to-back strain-gage pairs located 29 in. AFT from the midline were compared with the predictions as shown in Figures 22 and 23, respectively. The solid curves with the "×" markers in Figures 22 and 23 represent the predicted axial strain at the end of each load step of LS12. The dashed curves with the triangle markers in Figures 22 and 23 represent the measured axial strain at the end of each load step of LS12. In Figure 22, the predicted IML axial strains at the end of each load step of LS12 showed a generally sinusoidal pattern with the maximum compressive axial strain at the 180° circumferential location through load step 6 (60% of P_{cr}^{CL}), at which time the maximum compressive axial strain shifted to the 225° circumferential location by the end of load step 7 (70% of P_{cr}^{CL}). In Figure 23, the predicted OML axial strains at the end of each load step show a sinusoidal pattern with the maximum compressive axial strain at 180° for all load steps. The measured IML and OML axial strains at the end of each load step show a pattern with two waves and the maximum compressive axial strain established at 225° by the end of load step 2 (20% of P_{cr}^{CL}). The predicted strains were greater than the observed strains. The measured IML and OML axial strains indicate off-nominal loading at the end of each load step of LS12. This off-nominal loading is likely related to the uneven displacements that were seen in the total applied load versus displacement plots for the load line pairs in Figures 17 through 20. The cause of the off-nominal loading during LS12 is discussed further in the next section.

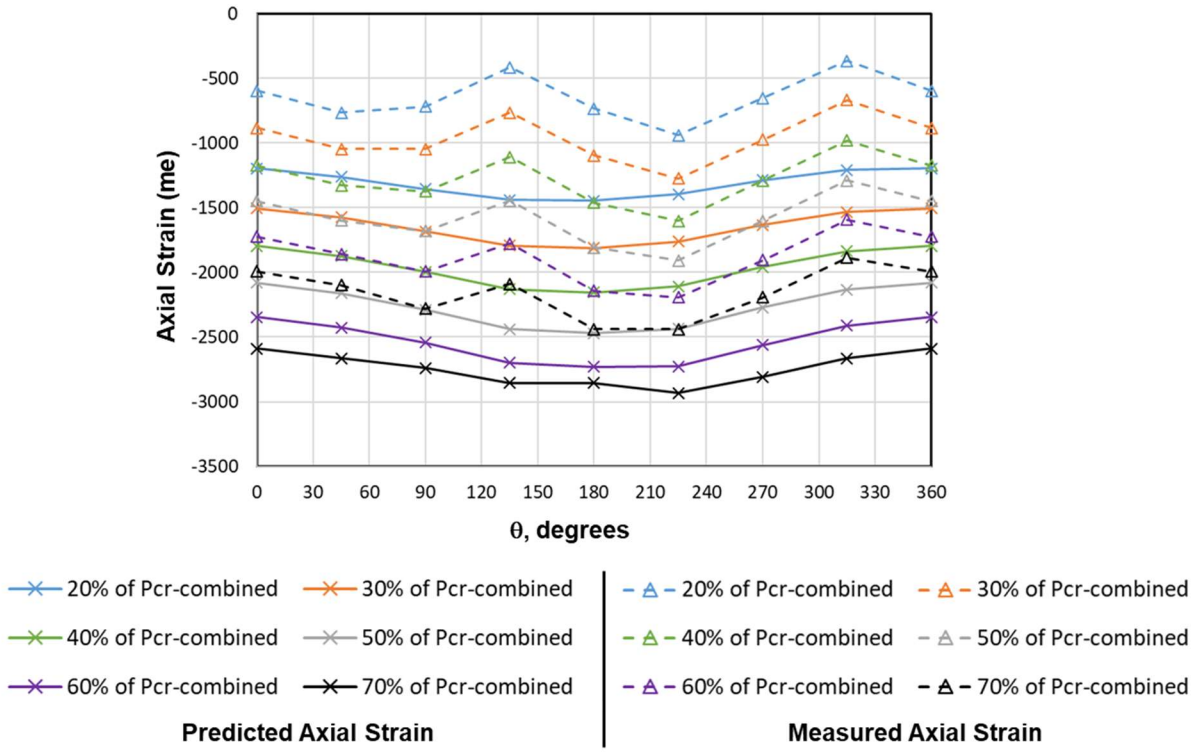

Figure 22. Predicted and measured IML axial strain gage along the AFT end ply-drop (29 in. below the midline).

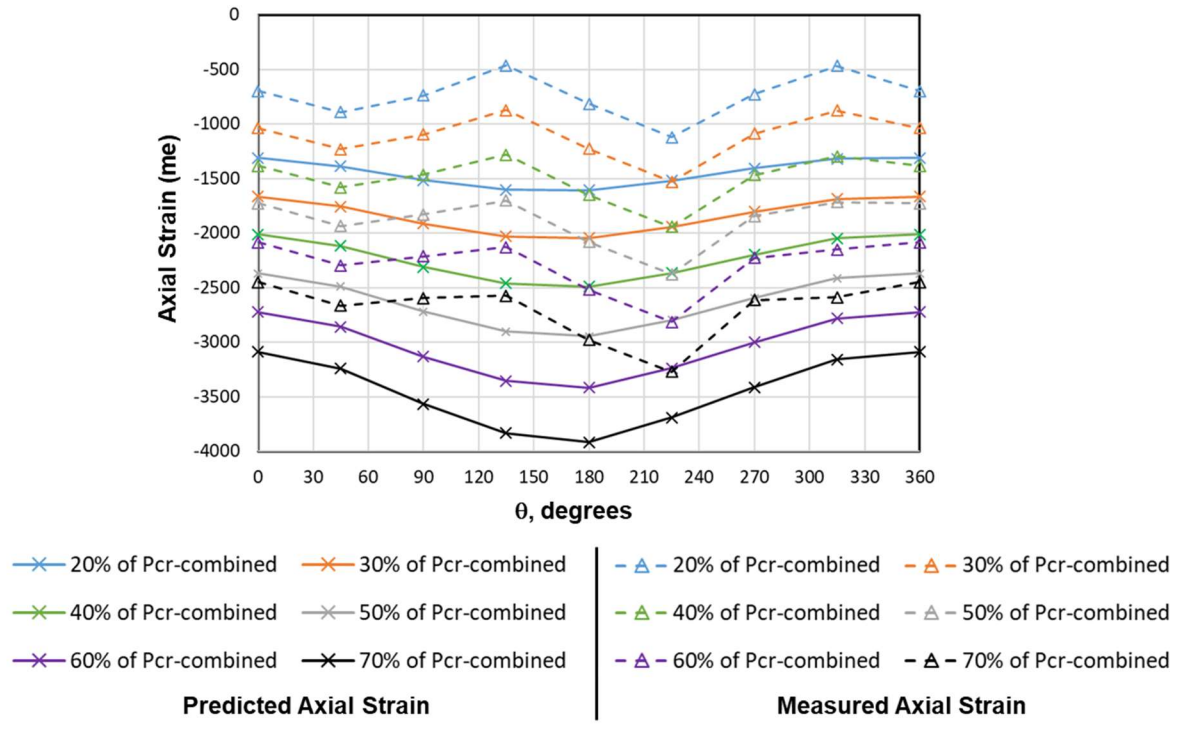

Figure 23. Predicted and measured OML axial strain gage along the AFT end ply-drop (29 in. below the midline).

The contour plots of the predicted radial deformations from the FEM and the measured radial deformations just prior to buckling are presented in Figures 24 and 25, respectively. The warmer (red) colors represent relative outward deformation, and the cooler (blue) colors represent relative inward deformation. A comparison of the measured and predicted radial deformation of CTA8.3 show major elements of agreement. Specifically, both contours show the largest radial outward deformation in the FWD ply-drop region between 150° and 210° circumferential location. In addition, a series of inward dimples appear at similar axial positions for the predicted and measured radial displacements, ±26 in. and ±27 in., respectively. However, the dominant inward deformation was predicted from the FEM to be at the 190° circumferential location and the dominant inward deformation observed during test was at the 240° circumferential location. The off-nominal loading observed in the axial strain plots in Figures 22 and 23 was likely associated with this difference in radial deformation pattern. In addition, the measured radial deformation shows a deformation pattern more skewed with respect to the z-axis than the predicted radial deformation. While there were some discrepancies related to the radial deformation pattern, both contour plots have similar minimum to maximum deformation ranges.

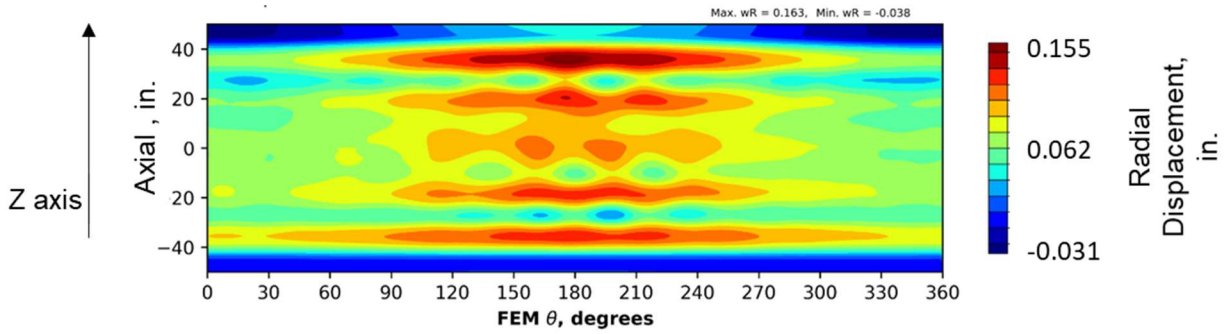

Figure 24. Predicted radial deformation contours of FEM before failure (Load = 462 kips).

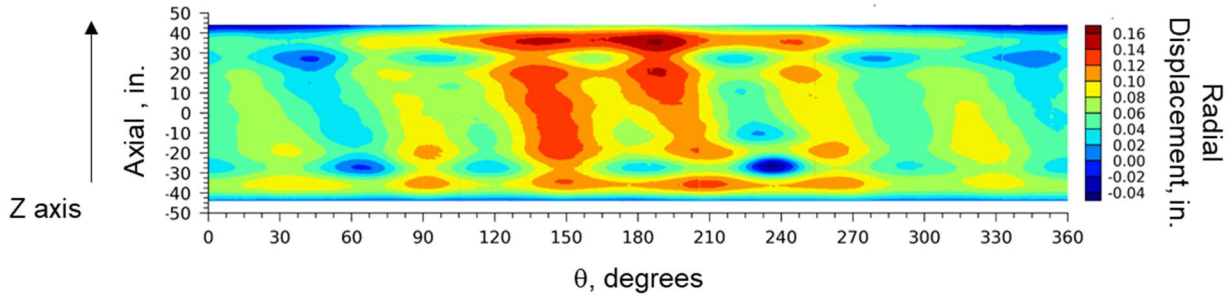

Figure 25. Measured radial deformation contours of CTA3.8 before failure (Load = 432 kips).

3.2 Anomalous Behavior of Load Frame Observed from DIC System (LS12)

During the ramp to tare (prior to load step 1), an anomalous behavior was observed in real-time DIC measurements. After observing this, the DIC test data were post-processed and compared

with the data from the four EDI locations on the FWD ring at the 0°, 90°, 180°, and 270° circumferential locations with excellent agreement, which confirmed that the behavior occurred.

To help characterize this anomalous movement in CTA8.3, the ramp to tare was completed twice for LS12 with full instrumentation recording. The resulting displacements and rotations from this ramp-to-tare cycle are presented in Figures 26 through 28, where the solid lines represent the DIC data extracted at the FWD ring, the dotted black lines represent the DIC data extracted in the acreage just below the FWD ring, and the EDI data are shown with dashed lines. During the ramps to tare, the FWD end of the test article moved in the 0° direction (x-direction) approximately 0.015 in. (as shown in Figure 26) and in the 270° (negative y-direction) 0.01 in. (as shown in Figure 27). This combined movement towards the 0° and 270° circumferential location was combined with an overall shear/twist of approximately 0.01° in the negative theta direction as shown in Figure 28.

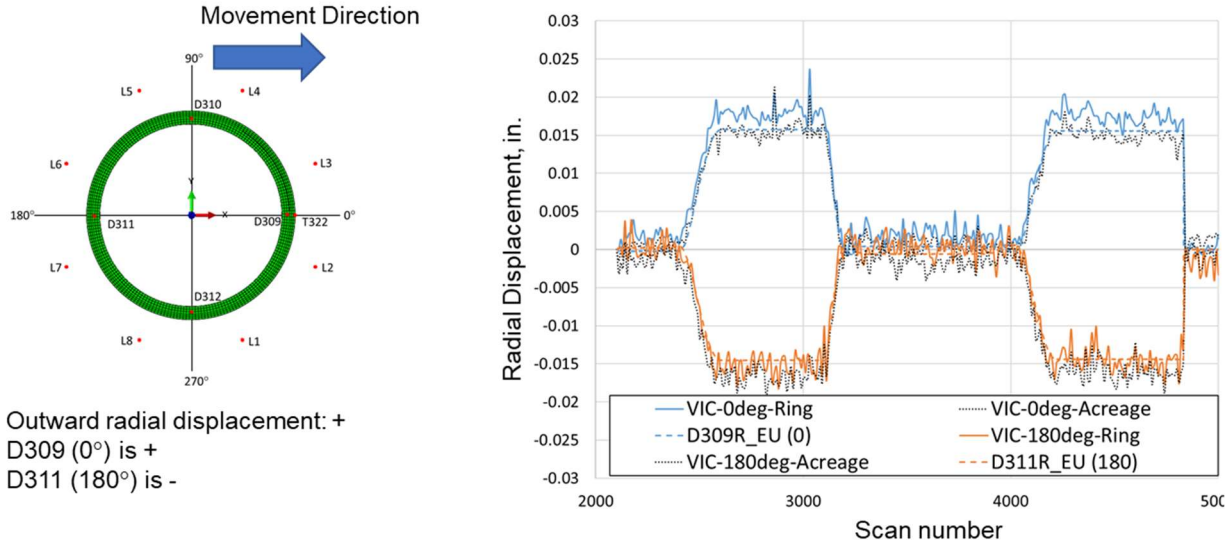

Figure 26. D309 and D311 Radial EDI Data versus DIC (including first and second tare).

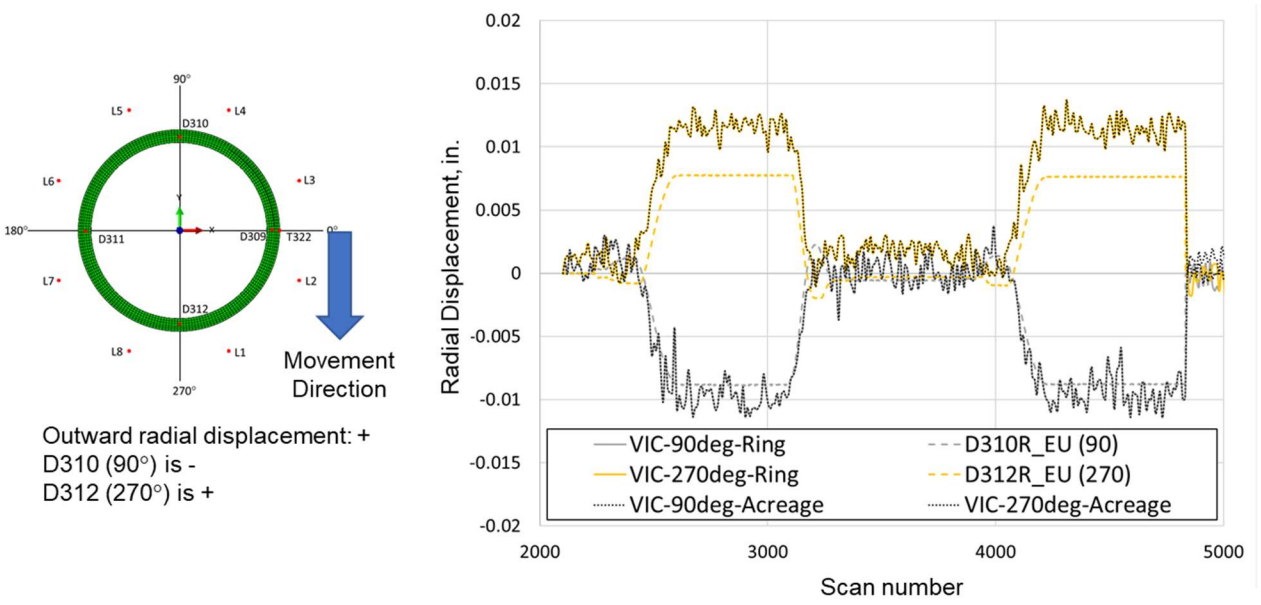

Figure 27. D310 and D312 Radial EDI Data versus DIC (including first and second tare).

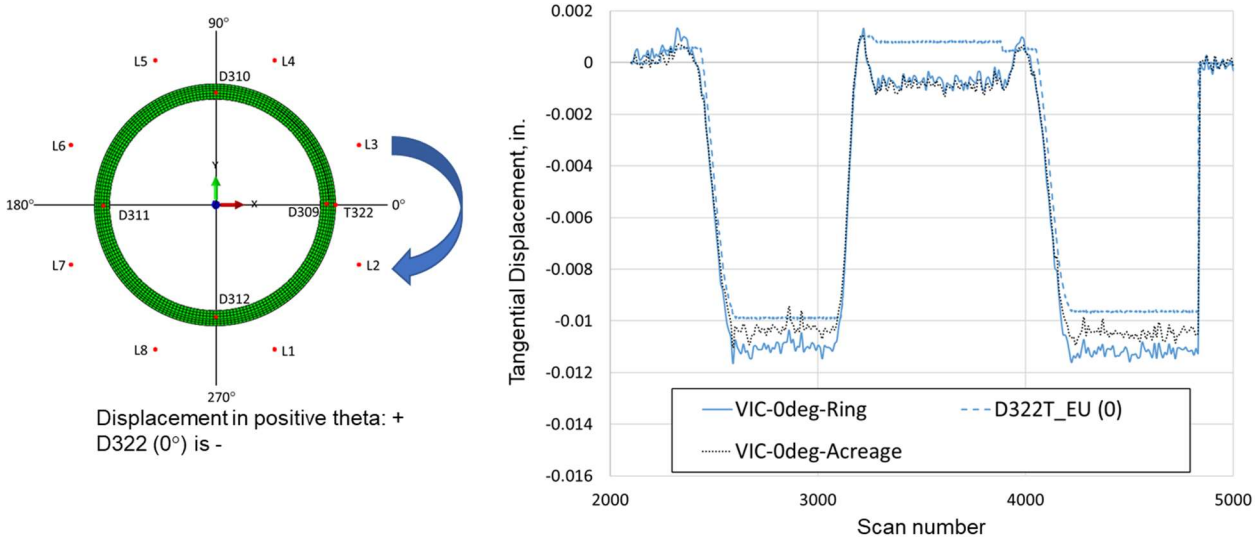

Figure 28. D322 radial EDI data vs DIC (including first and second tare).

Another interesting observation was made when looking at the axial displacement of the cylinder just past the termination of the attachment rings at the forward and aft end (45 in. from the midline). Figures 29 and 30 show circumferential line traces that were extracted from DIC at tare. The individual FWD and AFT test-article displacements near the rings are shown in Figure 29, while the difference in the FWD and AFT test-article displacement behavior, i.e., total shortening of the test article between measurement locations (subtracting the AFT displacements from the FWD displacements), is shown in Figure 30 (herein called a *delta plot*).

The FWD attachment ring and FWD end of the test article were expected to move uniformly up in the axial direction when the weight of the upper test hardware was removed from the test article during the ramp to the tare. In contrast, the AFT attachment ring should be essentially fixed and there should be very little, but uniform, displacement in the AFT end of the test article. It can be observed from Figure 29 that the AFT end of the test article did not behave as expected—the displacements were nonuniform, and they were not small compared to the FWD displacements. Specifically, the test article near the AFT attachment ring showed axial displacements of approximately –0.035 in. at approximately 150° and approximately –0.015 in. between 275° < θ < 345°, with a near zero displacement at 60° and 240°. Measurements indicate that the AFT attachment ring remained essentially fixed. Therefore, these test-article displacements indicate that the test article was moving independently from the AFT attachment ring, that there was some slipping of the test article in the AFT attachment ring. However, the uneven local axial displacements indicate that there was an uneven local axial displacement, which may indicate that there is a residual bond between the inner channel surface of the rings and the test article in some locations.

It is interesting to note that the delta plot in Figure 30, which corresponds to the total end shortening of the test article at a given circumferential location, is a similar shape to the axial strain plots in Figures 22 and 23, specifically the axial strain plots at 20% of P_{cr}^{CL}. Specifically, the areas of the lowest compressive axial strain observed in Figures 22 and Figure 23 (approximately 140° and 315°) correspond with the areas that had the least amount of end shortening, end shortening less than 0.01 in. The maximum axial compressive strain is near the circumferential location (60° and 240°) that had the greatest amount of end shortening of just over 0.03 in. The uneven local axial displacements and end shortening may have influenced the overall buckling pattern and/or failure load.

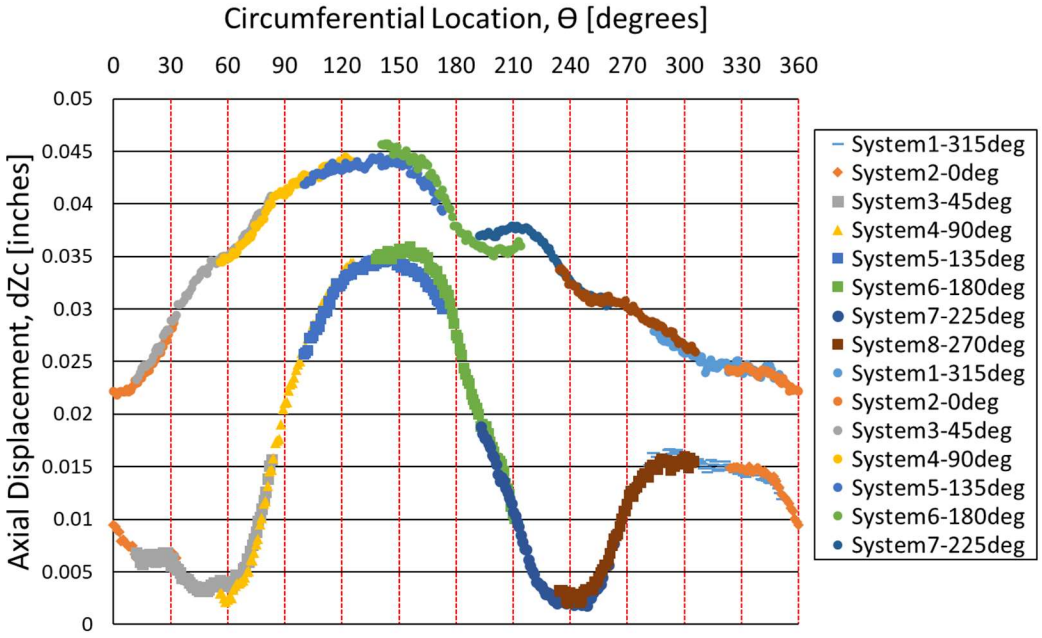

Figure 29. Circumferential line traces at AFT and FWD near ring location at tare.

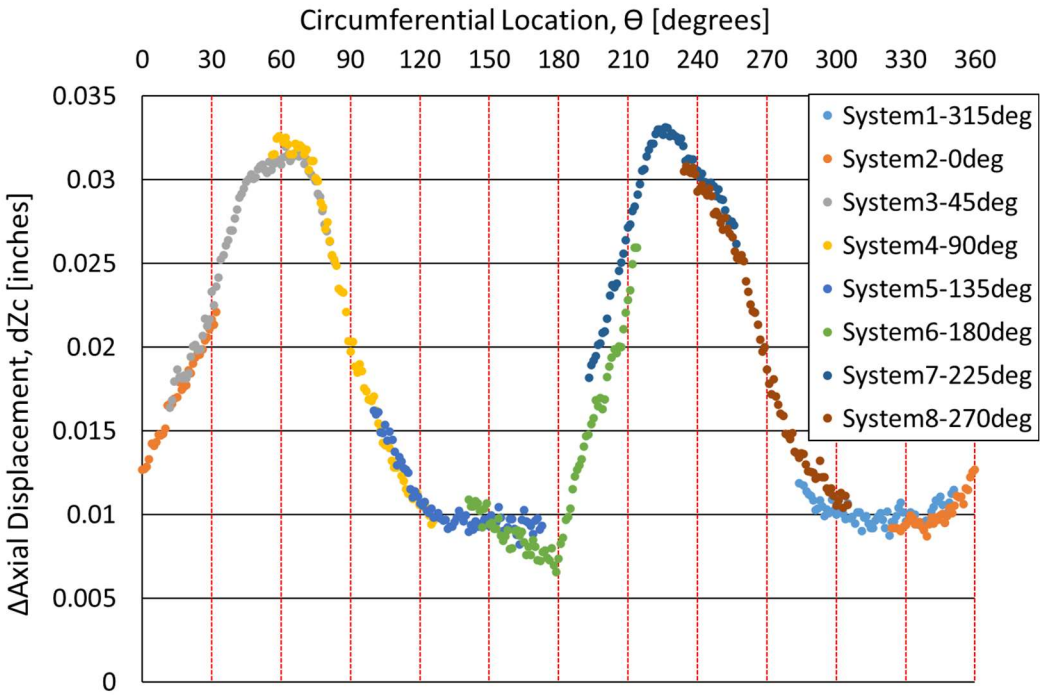

Figure 30. Delta plot [FWD-AFT] of circumferential line traces at ring location at tare.

3.3 Posttest Analysis of Global FEM with Load Frame Movement

After testing, additional analyses were executed to help determine reasons for the differences between the analysis results and test. The nonlinear transient dynamic analysis of CTA8.3 with the as-manufactured radial imperfections was repeated, but using the measured movements and twist of the FWD ring rather than the nominal movements. The objectives of the analysis described in this section was to simulate the observed movement of the FWD attachment ring during the ramp to tare and then the combined axial compression and bending loading, and to interrogate the effect of this anomalous FWD movement on the predicted buckling response.

The revised analysis discussed in this section was broken into two steps, both of which were nonlinear transient dynamic analysis steps. The ramp to tare, including the displacement of the FWD attachment ring observed during in the ramp to tare load, was simulated during the first step. The ramp to tare was simulated by applying a ramp load to 4.2 kips in each load line, and the rigid-body motion of the FWD ring was applied by ramping the observed displacements. The measured movements of the FWD ring were 0.015 in. toward the 0° direction and 0.01 in. toward the 270° direction during the ramp to the tare load, as discussed in Section 3.2. The reference node at the top of each load line was displaced by the prescribed amount. The implementation of the rigid body rotation in the analysis is illustrated in Figure 31.

The predicted and measured axial movement of the FWD ring at 0° and 180° (EDI 309 and 311) during the ramp to tare and the first step of the combined axial and bending load of LS12 are shown in Figure 32. The predicted and measured axial movement of the FWD ring at 90° and 270° (EDI 310 and 312) during ramp to tare and the first step of the combined axial and bending load of LS12 are shown in Figure 33. The dashed lines represent the test results and the solid lines represent prediction of FEM obtained from nonlinear transient dynamic analysis. Point A in both figures represents the initial condition of the test with the weight of the upper test hardware on the test

article. Point B and B' represent the predicted and measured end of the tare load when the weight of the upper test hardware and attachment ring is lifted off the test article, respectively. It should be noted that the data sensors (gages, EDIs, DIC, etc.) are zeroed at the tare load (points B and B') because the test article is in a nominally unloaded condition, but this is not simulated in the FEM. Therefore, point A is also the start of load step 1 for the plotted test data. At points B and B' the load lines are in compression, hence the negative total applied load of –32.2 kips. In all other total load vs displacement plots, the sensors are "zeroed" at point B', so negative values do not appear in any other plot with total applied load. Points C and C' represent the state of the test article at the end of load step 1 of LS12 for the pretest predictions and the test.

In both Figures 32 and 33, the load lines were predicted to displace in a linear manner as the FEM simulates the ramp to tare load from point A to B. During the test, the paths to the end of tare load for L2 and L3 were also linear, but reached the end of tare load with different axial displacements, B`. As the second step of the analysis is executed with the combined axial and bending loading, the predicted load-line displacements track linearly some slight deviation from point B towards point C at 100.0 kips. At the end of the tare load during the test, all instrumentation (i.e., load cells and EDIs) are re-zeroed so the test data plotted proceeds from point A to C' during load step 1. At the beginning of load step 1, the load increases without any measurable displacement until nearly 10 kips. After this point, the load and displacements increase proportionally until approximately 20 kips, at which point the load increases but the displacement of each load line oscillates about –0.02 in. until approximately 60.0 kips. After approximately 60.0 kips, the loading behavior is linear. The FEM was unable to capture this observed behavior, and the addition of the rigid body motion in the FEM did improve model correlation with respect to the total applied load versus displacement.

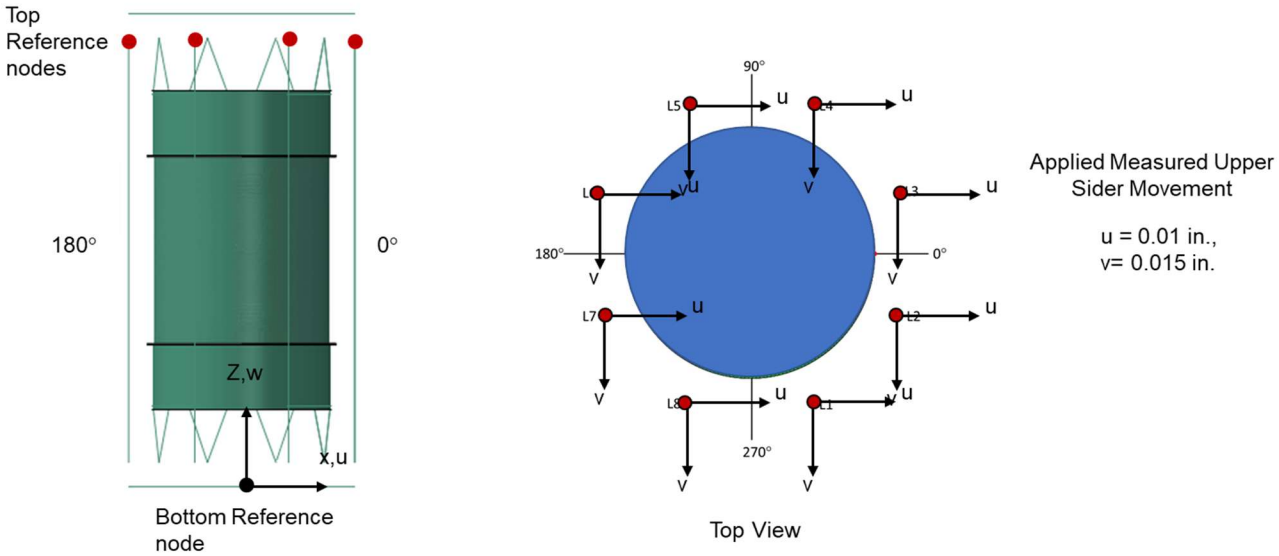

Figure 31. FWD ring fixture movement.

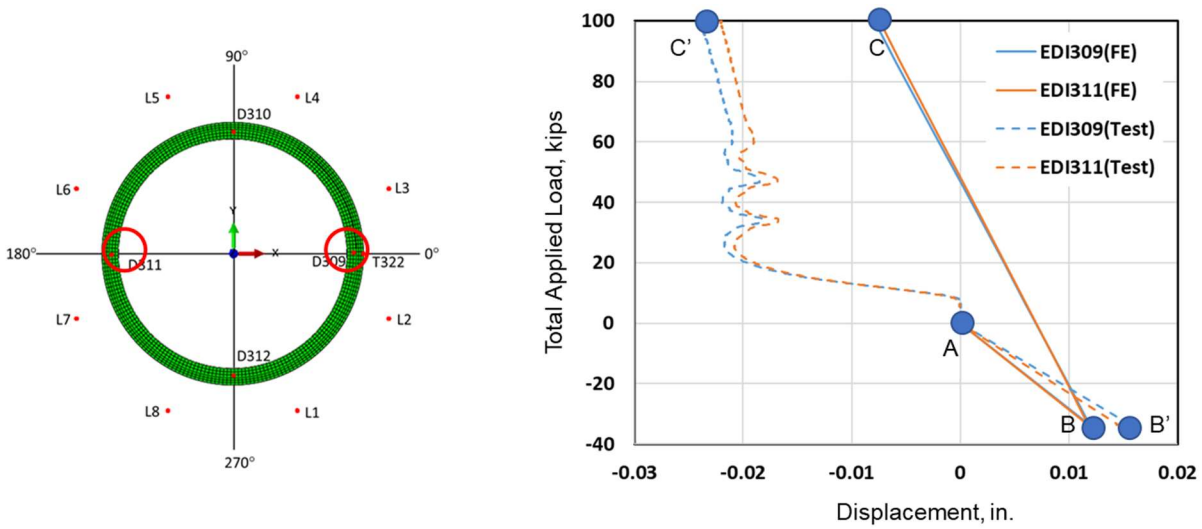

Figure 32. The predicted load versus radial displacement curves of EDI and test data (EDI 309 at 0° and EDI 311 at 180°).

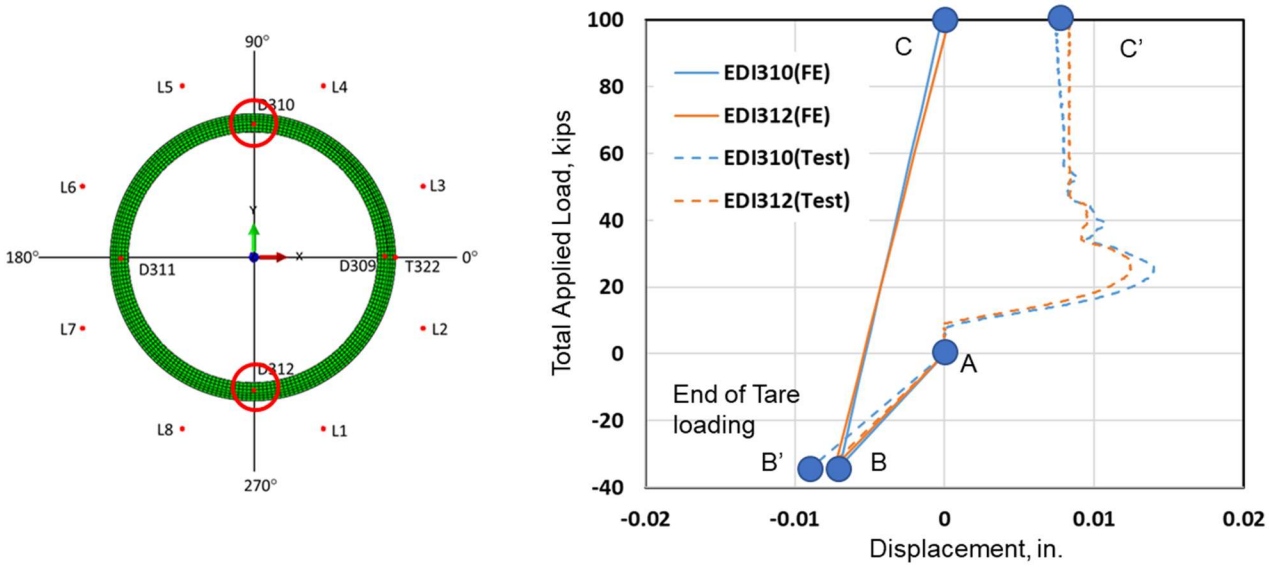

Figure 33. The predicted load versus radial displacement curves of EDI and test data (EDI 309 at 90° and EDI 311 at 270°).

The FEM discussed in this section with the observed movement of the FWD ring led to a predicted buckling load of 462.4 kips, which is the same as the pretest prediction from the FEM without the movement of the FWD ring. The radial deformation pattern and magnitudes predicted using the present model were also similar to the previous prediction. Therefore, the anomalous movement of the FWD ring did not seem to significantly affect the predicted failure load and global buckling response. As previously mentioned, the test article moved independently in a nonuniform manner from the AFT ring, which may influence the overall buckling pattern and/or failure load. This unanticipated independent motion cannot be correctly characterized by the FWD ring movement

of CTA8.3 because the FEM was built using shell elements with the attachment rings rigidly connected to the test article.

3.4 As-installed Radial Imperfections Pre-Tare and At Tare

During posttest data processing, it was noticed that the DIC-measured radial imperfections of CTA8.3 once installed in the test facility were significanlty different than those measured with structured-light scanning in the as-manufactured configuration. Recall that the as-manufactured imperfections, measured with the attachment rings installed but outside the test fixture, were used to make the pretest predictions. The as-installed configurations refer to the states of the test article when the test article was installed in the test frame either with or without the weight of the upper test hardware—that is, in the *pre-tare* and *tare* conditions. The discrepancies between the as-manufactured and as-installed radial imperfections could be caused by a combination of handling, securing (bolting) the attachment rings to test frame, and the relatively thin facesheets. In an attempt to improve correlation, the influence on the structural response was investigated by including the as-installed shapes of the test article in the FEM.

The DIC systems were used to measure the as-installed pre-tare and tare configurations. The thickness was presumeed not to have changed during the installation, so the as-manufactured thickness imperfections were used in these analyses with these as-installed imperfections.

To show the changes that occurred between the as-manufactured (structured light-based data) geometry and the as-installed (DIC-based data) geometry, contour plots of the test-article exterior surface (OML) are provided in Figure 34 through 36. (Note that Figure 34 shows the exterior radial shape, while the similar Figure 2 showed the midsurface radial shape.) It can be observed that the ranges of the exterior surface radial position are very similar across all three figures. There is a significant difference, however, in the patterns of the contours between the as-manufactured and the as-installed surfaces, but both as-installed contour plots have qualitatively similar imperfection shapes. (Note that the repeating vertical features in the as-installed plots are numerical effects caused by interpolation over strain gage wire bundles and by stitching multiple DIC camera systems together.)

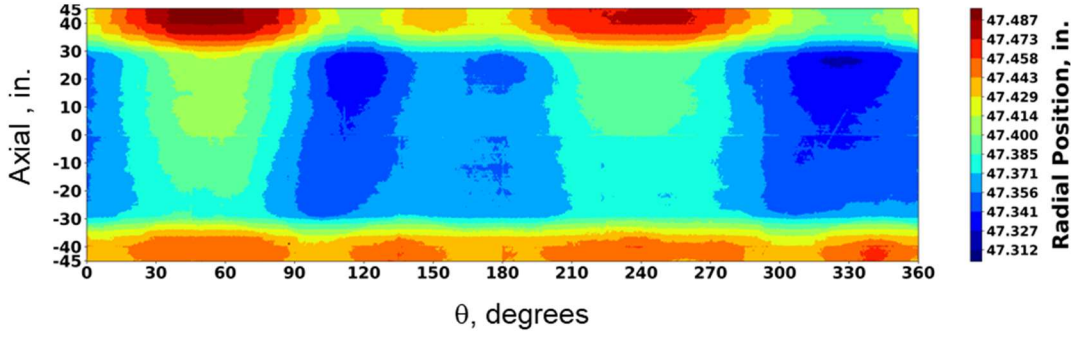

Figure 34. As-manufactured (structured light scan data) exterior surface.

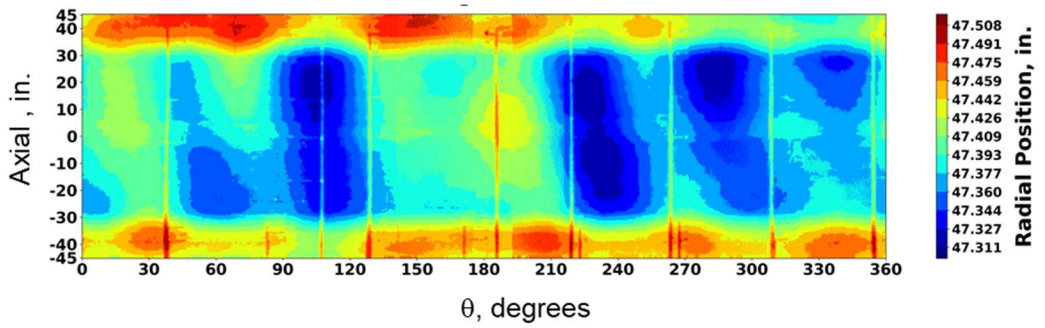

Figure 35. As-installed (DIC data) exterior surface with the weight of the loading structure on the test article, the pre-tare radial shape.

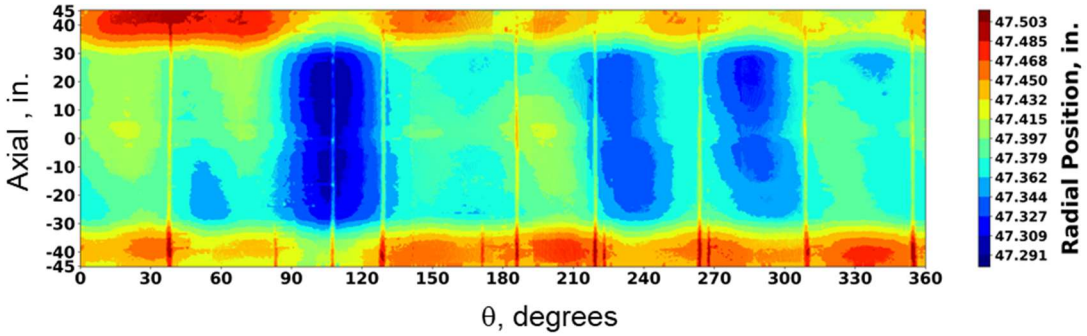

Figure 36. As-installed (DIC data) exterior surface with the weight of the loading structure removed from the test article, the tare radial shape.

3.5 Posttest Analysis of Global FEM with As Installed Radial Imperfection

The DIC-measured exterior surface geometry of CTA8.3 in the *pre-tare* and *tare* as-installed configurations and the structured-light as-manufactured thickness imperfections were used to generate two additional global FEMs for the two as-installed configurations. The comparisons of the predicted global buckling response of these FEMs with these as-installed geometries with the test results from LS12 are presented in this section.

Nonlinear transient buckling analyses were performed in a manner similar to the pretest predictions to interrogate the influence of the pre-tare and tare radial imperfections on the prebuckling and postbuckling response of the test article for LS12. However, for this set of posttest analyses, the measured axial load line displacements from each load step of LS12 were applied to the FEM in an attempt to more accurately model the loading conditions during test and match the asymmetry for each load line pair. Since the movement of the FWD ring had negligible effect on the predicted response of FEMs, it was not included in these as-installed analyses.

The test and predicted total applied load versus end-shortening response of each pair of load lines are shown in Figures 37 through 40. The predicted total applied load versus average axial end-shortening response of CTA8.3 (the average of δ_{D000A}, δ_{D090A}, δ_{D180A}, and δ_{D270A}) are shown in Figure 41. In these figures, solid lines represent the odd numbered load lines and dashed lines represent the even numbered load lines. Also, in these figures, "IMG160" refers to the FEM with the pre-tare radial imperfection and "IMG380" refers to the FEM with the tare radial imperfection.

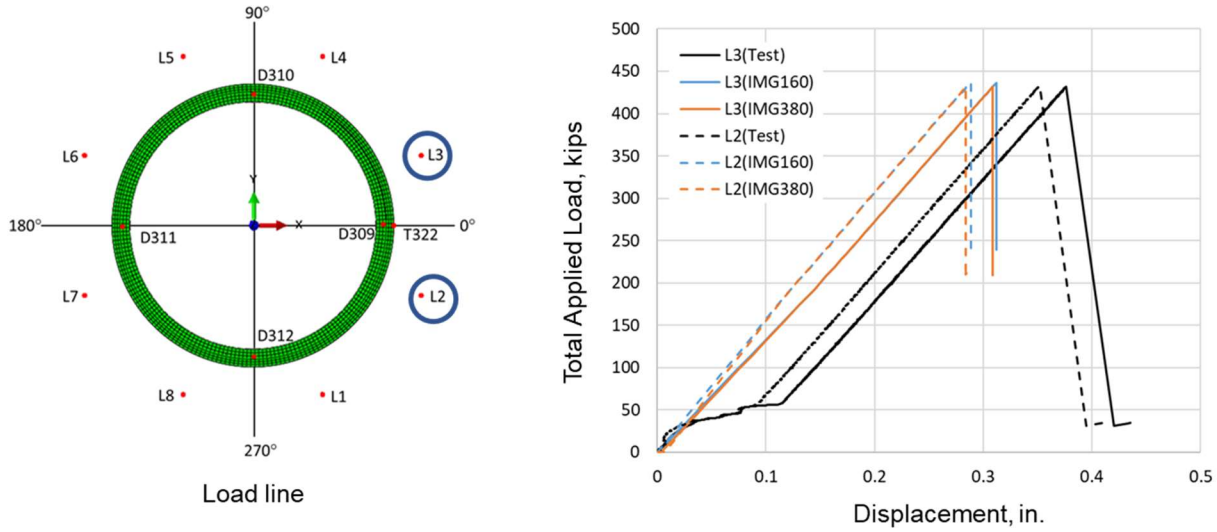

Figure 37. The predicted load versus end-shortening curves of FEM and test data (Load lines 2 and 3).

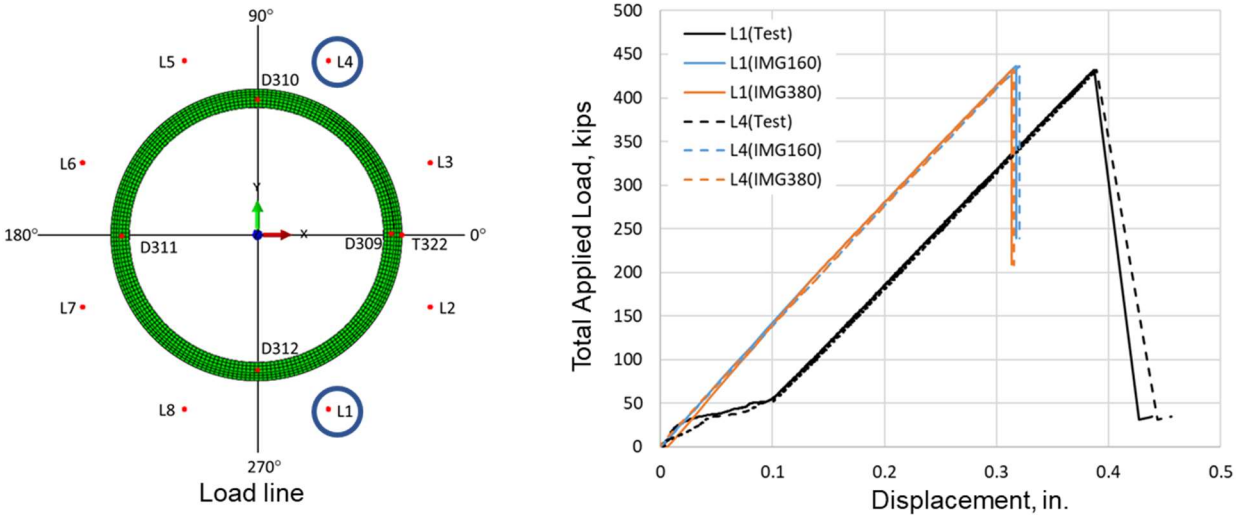

Figure 38. The predicted load versus end-shortening curves of FEM and test data (Load lines 1 and 4).

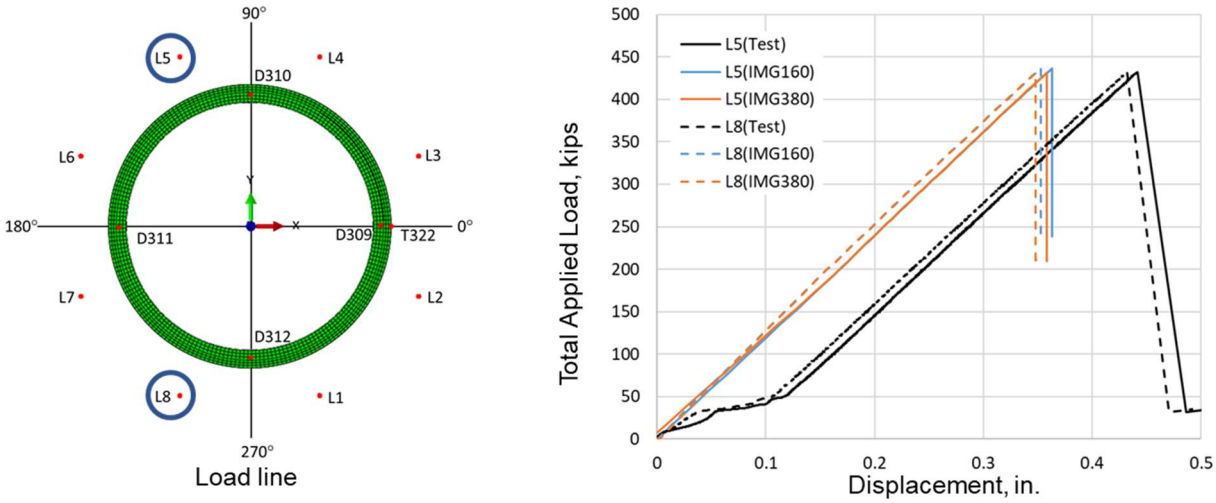

Figure 39. The predicted load versus end-shortening curves of FEM and test data (Load lines 5 and 8).

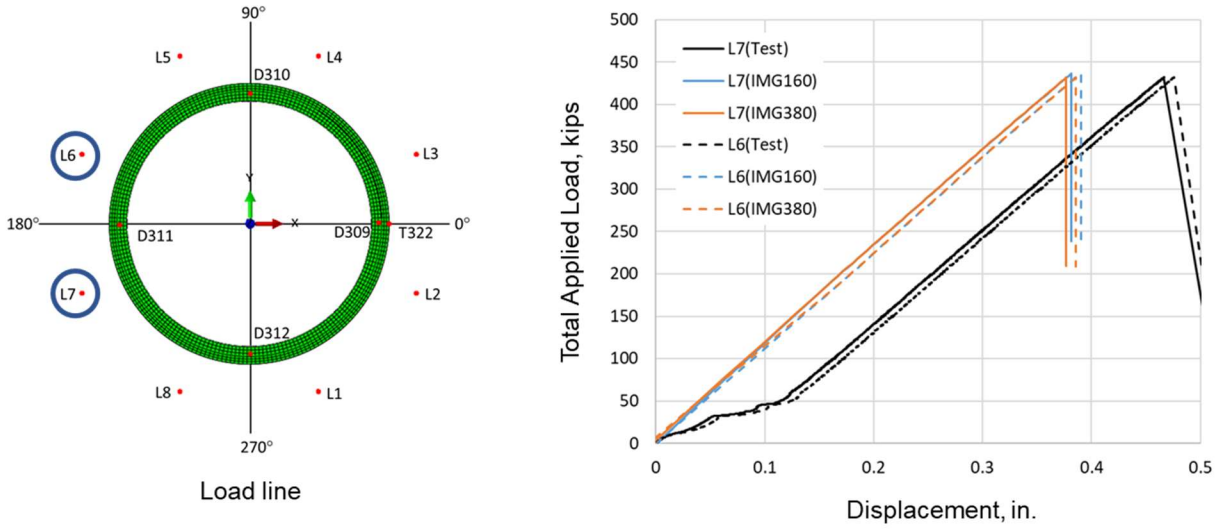

Figure 40. The predicted load versus end-shortening curves of FEM and test data (Load lines 6 and 7).

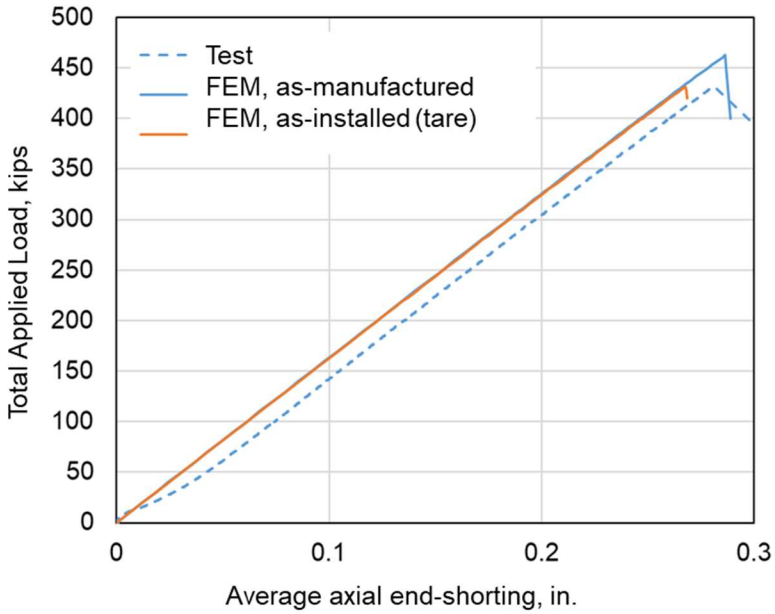

Figure 41. The tested and predicted total load versus average axial end-shortening measured at the attachment rings.

The predicted buckling load for CTA8.3 obtained from the FEM with pre-tare radial imperfections was 436.7 kips, 1% greater than the buckling load observed from the test. The predicted buckling load for CTA8.3 obtained from the FEM with the tare radial imperfections was 431.6 kips, 0.1% less than the buckling load observed from the test. Therefore, the predicted buckling loads of both FEMs with the as-installed imperfections were much closer to the test data and show significant improvement as compared with the pretest analysis prediction with the as-manufactured imperfection that was 7% higher than the test data, as shown in Figure 41.

The contour plots of the predicted radial deformations of the FEMs with as-installed imperfections and the measured radial deformations at the buckling load are presented in Figure 42. All results show the largest radial outward deformation in the FWD ply-drop region between the 120° and 240° circumferential locations. The predicted and measured buckling initiation sites (indicated by the most inwardly displaced dimple in these plots) were also between 120° and 240°, but just within the acreage near the AFT padup. The buckling initiation sites predicted from the FEMs with the as-installed imperfections from pre-tare and tare are at 190° and 175°, respectively. In contrast, the buckling initiation site seen in the test article was observed at the 240° circumferential location. In addition, the measured radial deformation shows a more twisted or skewed deformation pattern than the predicted radial deformation. The deformation magnitudes for both as-installed imperfection shapes were similar in magnitude as measured during test.

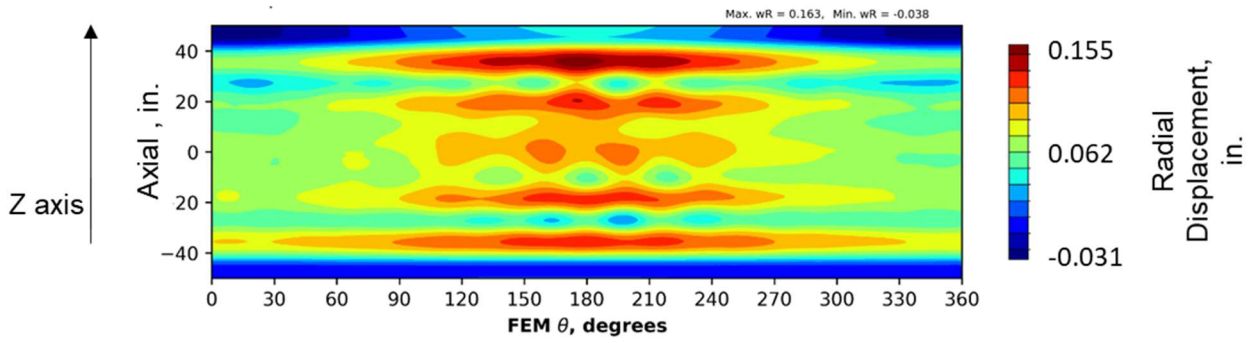

a. Radial deformation contour of FEM with the pre-tare imperfection before buckling (Load = 436.7 kips).

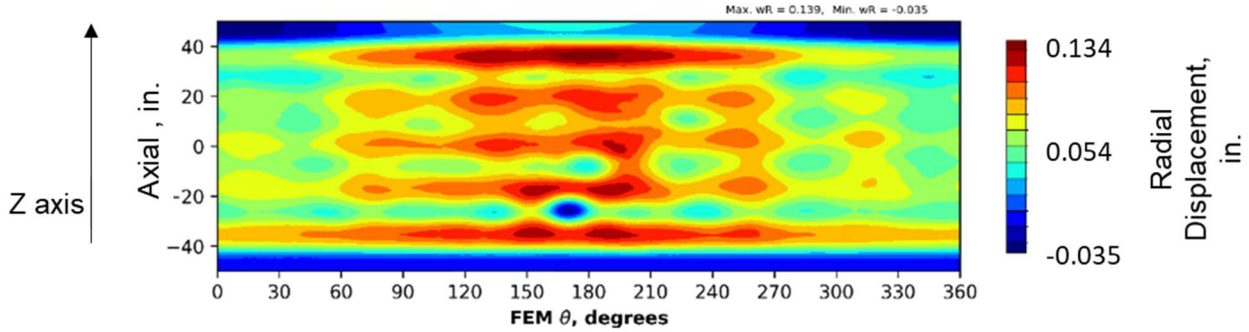

b. Radial deformation contour of FEM with the tare imperfection before buckling (Load = 431.6 kips).

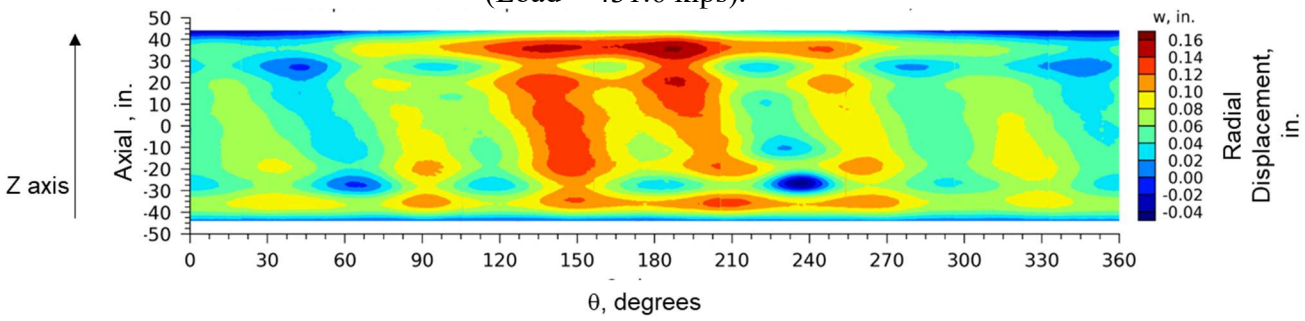

c. Measured radial deformation contours of CTA3.8 before buckling (Load = 432.0 kips).

Figure 42. Predicted radial deformation contours of the FEM with measured radial deformation contours of CTA8.3.

Next, the predicted axial stains of posttest FEM with the as-installed imperfections and measured axial strain data of various strain-gage locations on CTA8.3 are compared. The predicted axial strains from the FEMs with the pre-tare and tare imperfections showed similar patterns and magnitudes; therefore, only one set of predicted strains (tare imperfection) are presented to compare with measured strains. In Figure 43, axial gages that had good agreement between analysis and test are circled in black, and the axial gages that did not have good agreement between test and analysis are circled in red. Most of the predicted IML and OML axial strains shown in Figure 43 are consistent with test data. The strain gages on the *FWD 38-in. line* and the *AFT 38-*

in. line were located +/-38 in. from the center line of CTA8.3, and strain gages on the *FWD 29-in. line* and *AFT 29-in. line* were located +/-29 in. from the center line of CTA8.3. First, the axial strains at the 90° and 270° degree locations that had good agreement are discussed and compared for reference, and then the axial strains on AFT 38-in. line and AFT 29-in. line at 135° and 225° are discussed and compared to indicate differences between prediction and test.

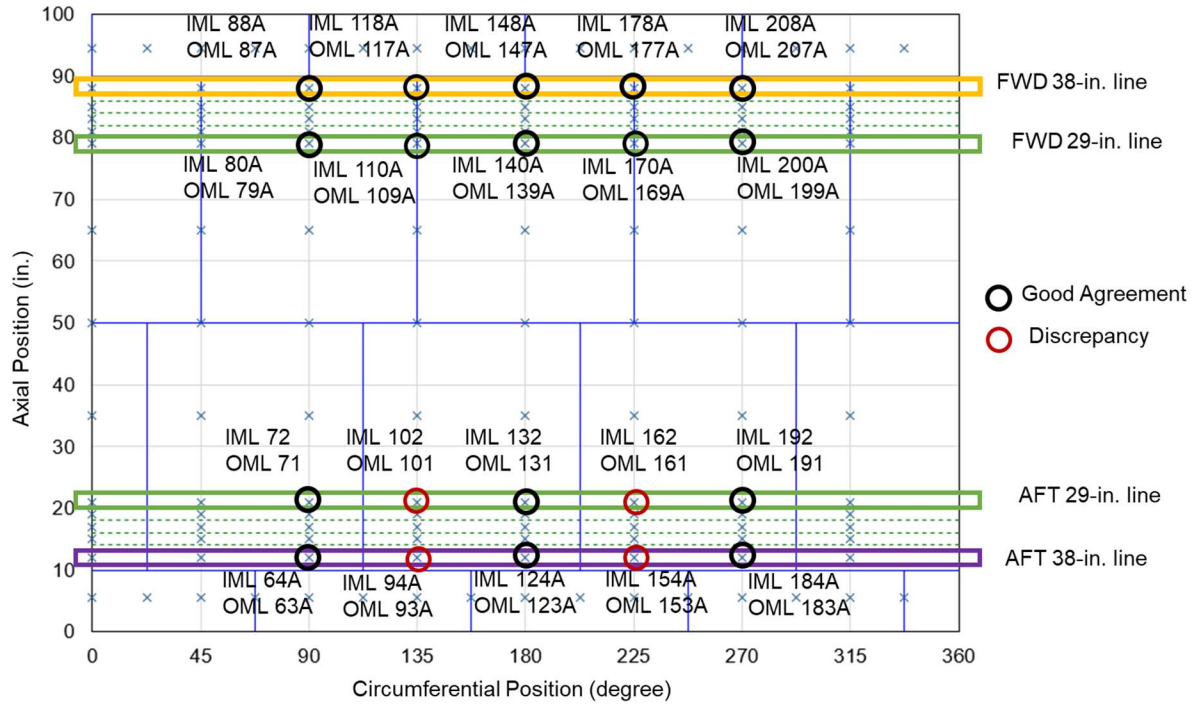

Figure 43. Axial strain gage location on the CTA8.3.

The predicted back-to-back axial strains from the FEM and the measured axial strains are shown in Figures 44 through 47 where the predicted axial strain and test data of IML and OML gages 63, 64, 71, 72, 79, 80, 87 and 88 are presented. These gages are at the 90° circumferential location of AFT 38-in. line, AFT 29-in. line, FWD 29-in. line, and FWD 38-in. line regions and show good agreement between predicted and test axial strain data. The maximum deviation between the predicted and observed strains was 8%.

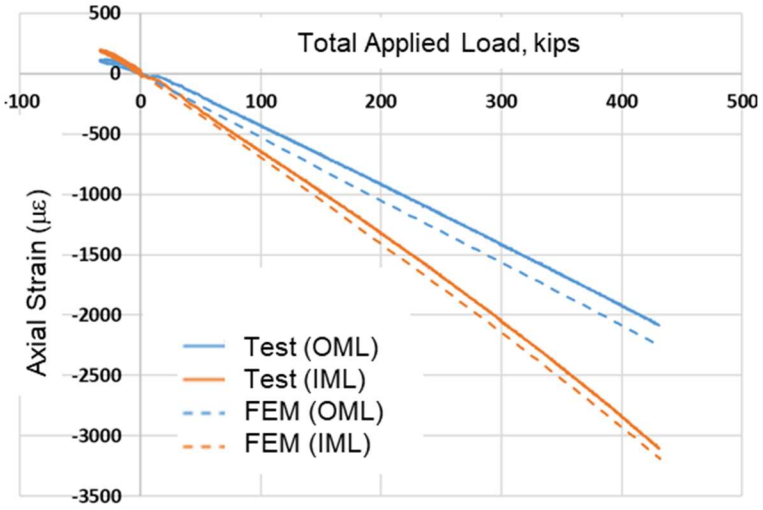

Figure 44. Predicted axial strain and test data of IML gage 64 and OML gage 63 (AFT 38-in. line).

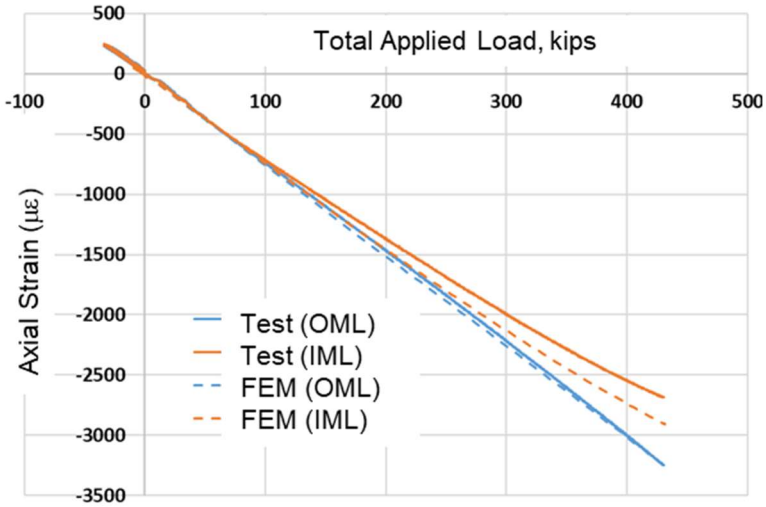

Figure 45. Predicted axial strain and test data of IML gage 72 and OML gage 71 (AFT 29-in. line).

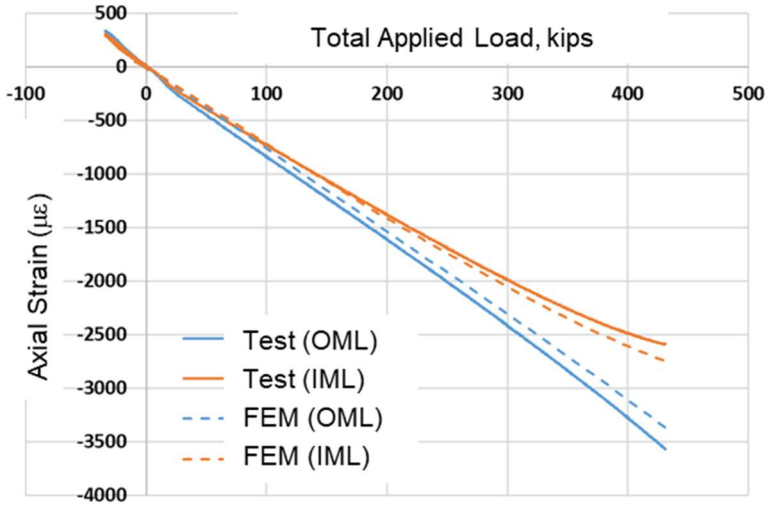

Figure 46. Predicted axial strain and test data of IML gage 80 and OML gage 79 (FWD 29-in. line).

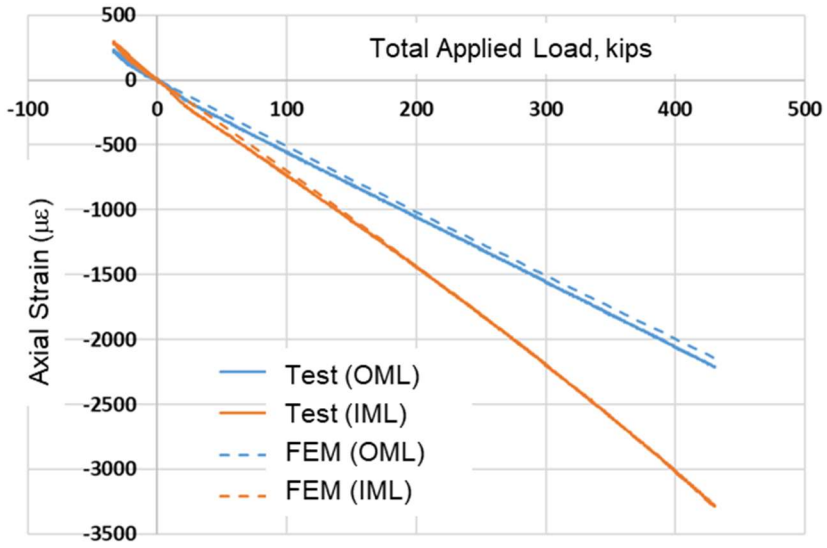

Figure 47. Predicted axial strain and test data of IML gage 88 and OML gage 87 (FWD 38-in. line).

The predicted axial strain and test data of IML and OML gages 183, 184, 191, 192, 199, 200, 207 and 208 are shown in Figures 48 through 51. These gages are at the 270° circumferential location of AFT 38-in. line, AFT 29-in. line, FWD 29-in. line, and FWD 38-in. line regions. In general, there was good agreement between predicted axial strain and test data as presented in these figures. The maximum deviation between the predicted and observed is 9.6%. However, small oscillating axial strain responses were observed from test at AFT 38-in. line and AFT 29-in. line during load step 1 of LS12, while predicted axial strains displayed more linear responses. These small oscillating axial strain responses were also observed from 180° circumferential location of AFT

38-in. line, AFT 29-in. line locations and are a function of the load control system when the applied load transitions from tension to compression, and are likely triggered by pin slop in the load line connections.

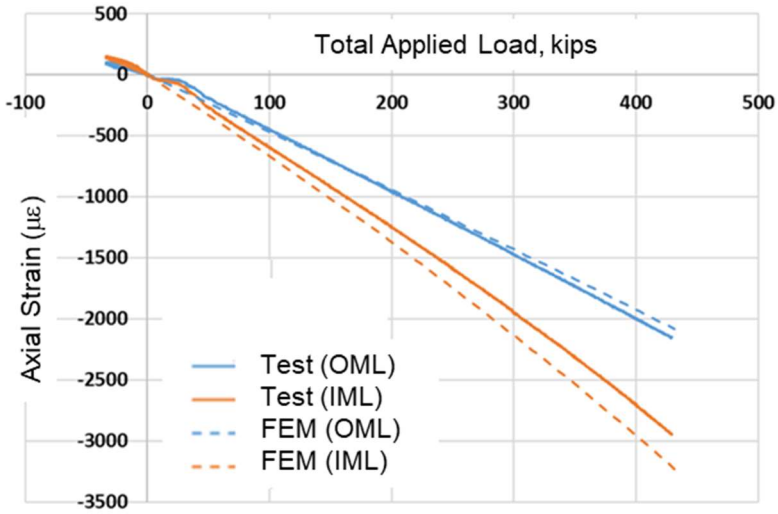

Figure 48. Predicted axial strain and test data of IML gage 184 and OML gage 183 (AFT 38-in. line).

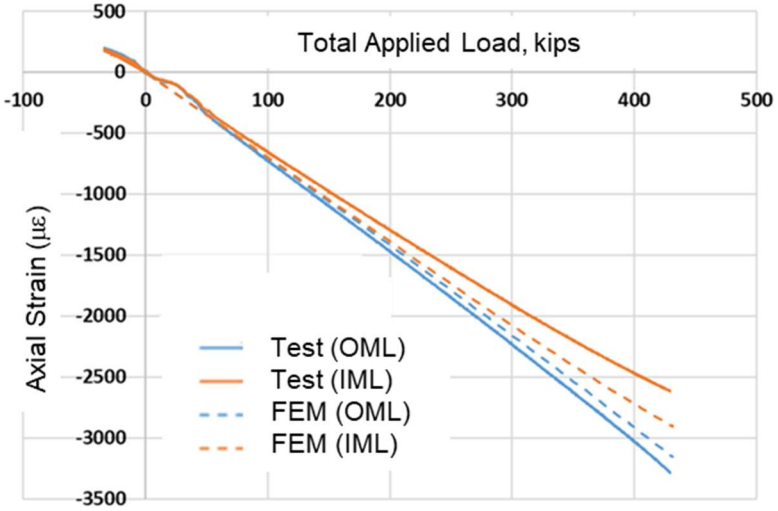

Figure 49. Predicted axial strain and test data of IML gage 192 and OML gage 191 (AFT 29-in. line).

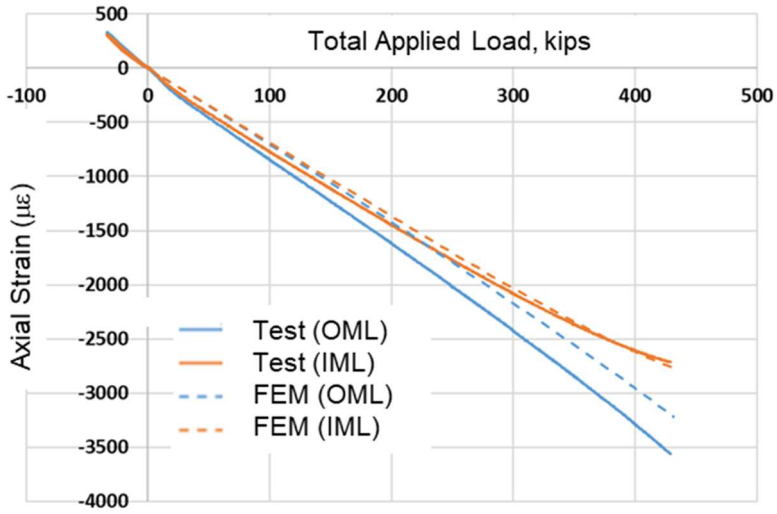

Figure 50. Predicted axial strain and test data of IML gage 200 and OML gage 199 (FWD 29-in. line).

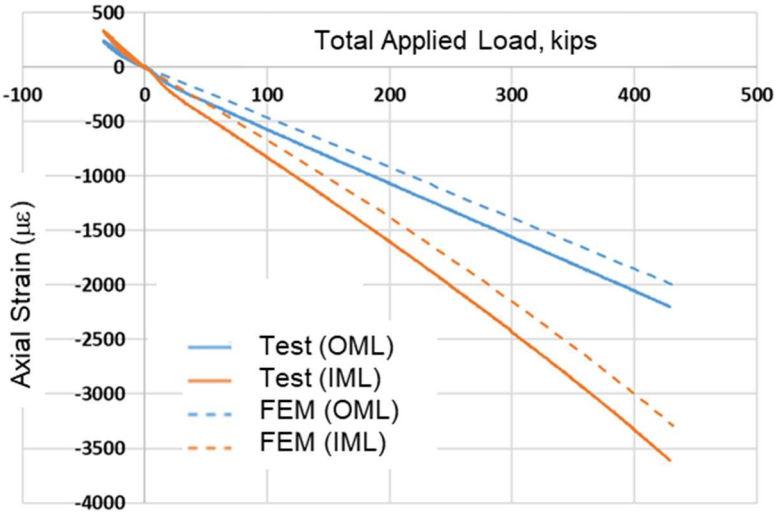

Figure 51. Predicted axial strain and test data of IML gage 208 and OML gage 207 (FWD 38-in. line).

The predicted IML and OML axial strains on AFT 38-in. line and AFT 29-in. line at 135° and 225° circumferential locations show larger discrepancies with measured axial strains, as shown in Figures 52 through 55. Figures 52 and 53 show compressive axial strain plateaus in the test data on AFT 38-in. line and AFT 29-in. line at the 135° circumferential locations during load step 1 of LS12. This is consistent with the DIC data previously discussed that revealed the movement of the test article from the AFT ring near the 135° circumferential location during the ramp to tare and the settling back into the AFT ring during load step 1 of LS12. Therefore, the strain plateaus observed in the gages at the AFT 38-in. line and AFT 29-in. line at the 135° circumferential locations could be related to the test article slipping in the attachment rings. Other than the plateaus

in the axial strains, which were not predicted, the predicted IML and OML axial strain curves are similar to the corresponding test-data curves, as they exhibit the same stiffness that is demonstrated by the comparable slopes. The global FEM was built using shell elements and did not allow for separation between the test article and the load-introduction ring, which prevented the ability to simulate the separation event during load step 1 of LS12.

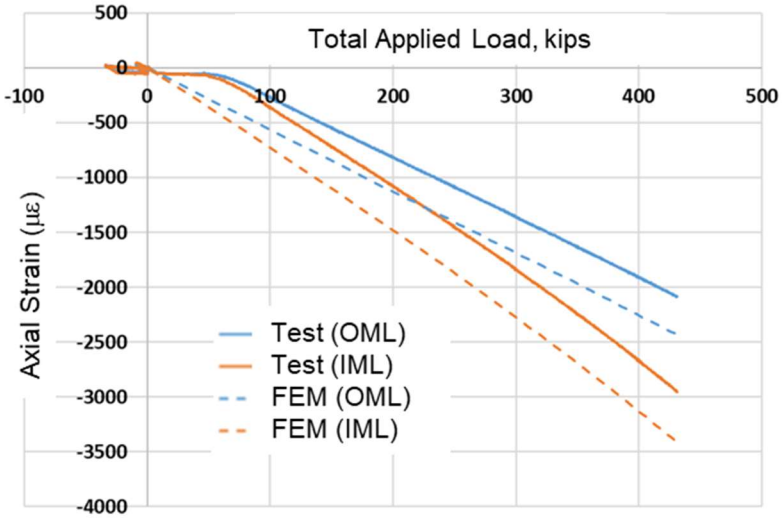

Figure 52. Predicted axial strain and test data of IML gage 94 and OML gage 93 (AFT 38-in. line 135°).

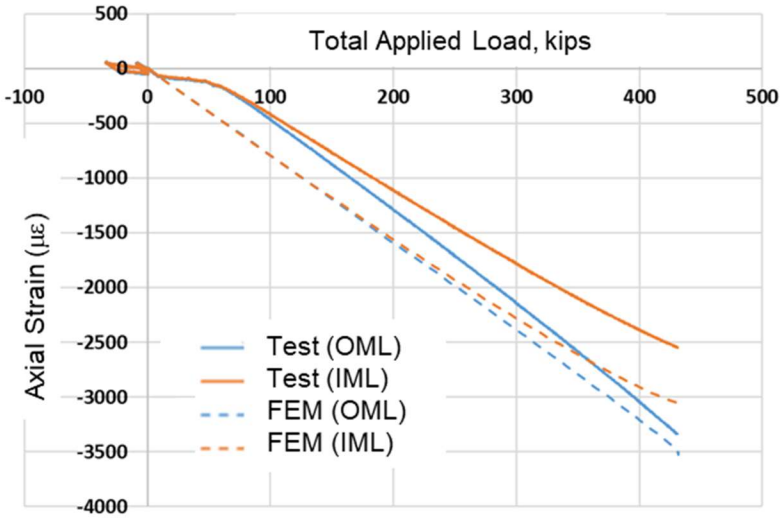

Figure 53. Predicted axial strain and test data of IML gage 102 and OML gage 101 (AFT 29-in. line 135°).

In Figures 54 and 55 different axial OML and IML axial strain growth patterns are observed. In Figure 54, at AFT 38-in. line 225°, test data show that the divergence in the back-to-back strains began at the beginning of load step 1 of LS12, then OML and IML axial strain curves had a

consistent slope. Predicted back-to-back axial strain show that the divergence in the back-to-back strains began at the end of load step 1 of LS12, then the slop of both OML and IML axial strains continually diverged. In Figure 55, at AFT 29-in. line 225°, the predicted back-to-back axial strain curves have a consistent slope at the beginning of load step 1 of LS12, then the OML strain magnitude increases at a faster rate than the IML at higher loads. The test data showed a similar pattern, but the divergence in the back-to-back strains began at the beginning of the load sequence.

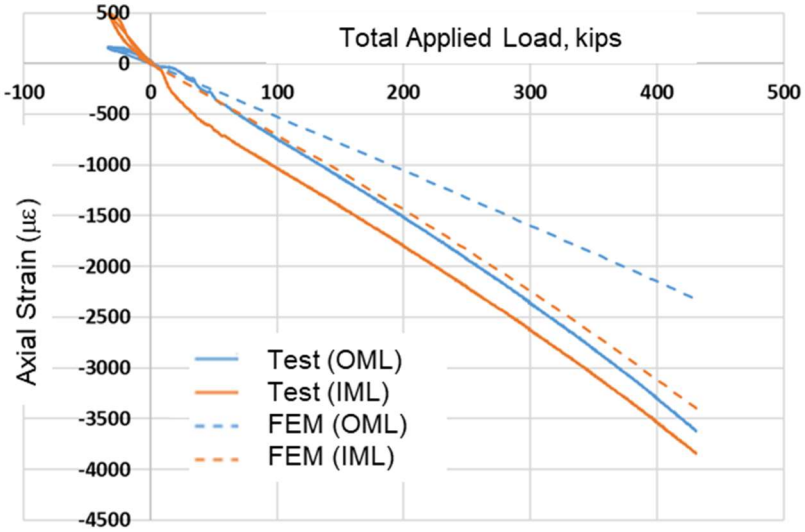

Figure 54. Predicted axial strain and test data of IML gage 154 and OML gage 153 (AFT 38-in. line 225°).

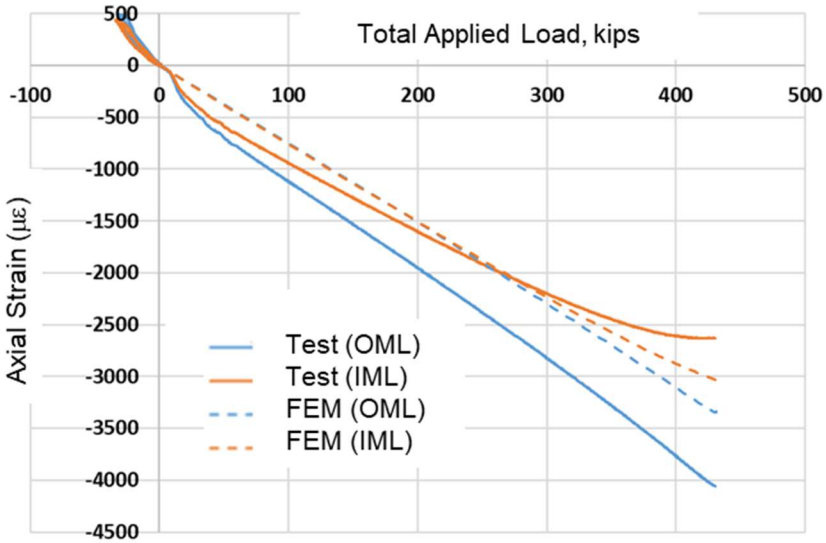

Figure 55. Predicted axial strain and test data of IML gage 162 and OML gage 161 (AFT 29-in. line 225°).

Although the predicted buckling loads from both FEMs with the as-installed radial imperfections, pre-tare and tare, were within ±1% of the experimental buckling load, the predicted buckling initiation site was not consistent with test data. The test data, including EDI, strain, and DIC,

indicated that CTA8.3 unexpectedly separated from AFT ring near 135° circumferential locations and settled back into the AFT ring during the ramp to tare and the first step of LS12, which contributed to the development of additional geometry and loading imperfections. This separation event of CTA8.3 during the tare and the first step of LS12 was not simulated using the FEMs with the pre-tare and tare radial imperfections due to the modeling approach used in the FEM. Despite this shortcoming in the analysis, the agreement between these revised analyses and the test was better compared to the results from the analysis with the manufactured radial and thickness imperfections.

3.6 Summary of the influence of geometric imperfection of CTA8.3

FEMs of CTA8.3 were developed utilizing various geometric imperfection inputs, and nonlinear transient dynamic analyses were performed to predict the prebuckling and buckling response of CTA8.3. The predicted buckling loads from the FEMs with different geometric imperfections, and the percent differences between the test load and each analysis, are presented in Figure 56. During LS12, CTA8.3 failed with the total applied load 432.0 kips at 86.4% of the predicted critical load. The predicted nonlinear buckling load obtained from the FEM with the geometrically perfect mesh was 494.0 kips, 14% higher than the test results. The predicted nonlinear buckling load obtained from the FEM with as-manufactured radial and thickness imperfections was 462.4 kips, 7% higher than test results. The predicted nonlinear buckling load obtained from the FEM with the as-manufactured radial and thickness imperfections and the movement of the FWD ring observed during the ramp to tare was 462.2 kips, also 7% higher than test results. After the measured surface imperfection of CTA8.3 in the test facility was reviewed, revised radial imperfections based on these data (at the pre-tare and tare loads) were generated. The predicted buckling load obtained from the FEMs with the as-installed radial imperfection before tare (i.e., pre-tare) and the as-manufactured thickness imperfection was 436.7 kips, 1% higher than test results. The predicted buckling load obtained from the FEM with as-installed imperfection at tare and the as-manufactured thickness imperfection was 431.6 kips, 0.1% lower than the test result. FEMs with as installed radial imperfection on the test stand and tare loading condition accurately predicted the buckling load of CTA8.3.

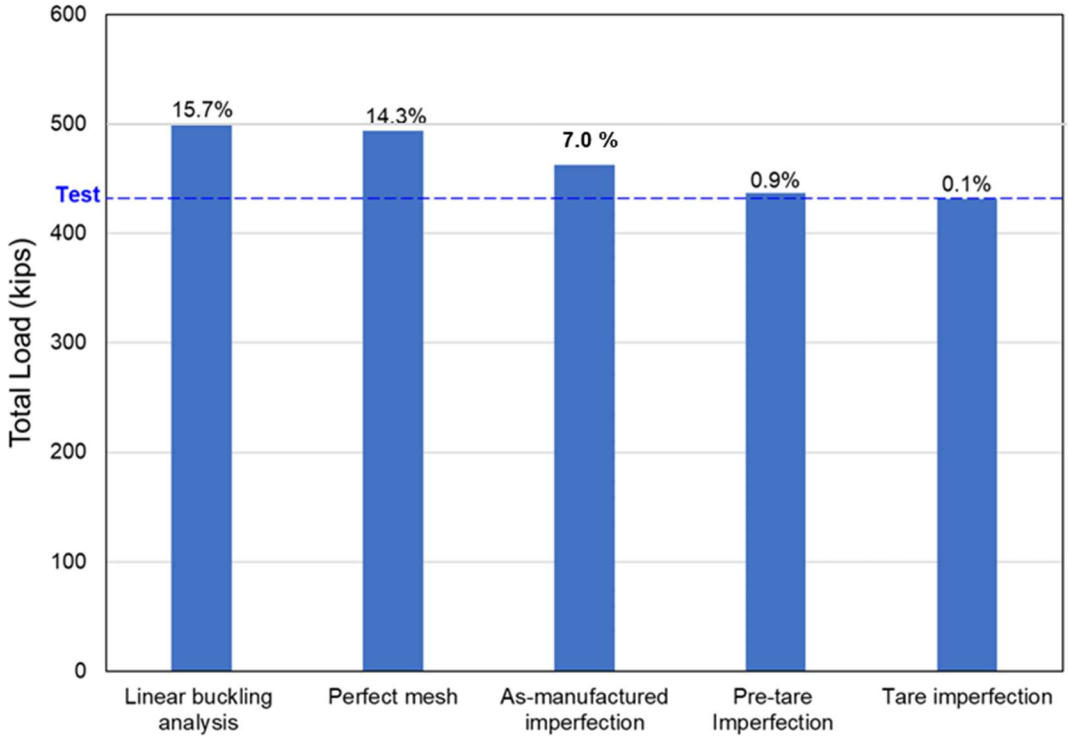

Figure 56. Predicted buckling loads of FEMs with different geometric imperfections.

A summary of the radial deformations just prior to buckling for the test and all FEMS with radial imperfections are presented in Figure 57. In general, a comparison of the radial deformations just prior to buckling during the test (Figure 55a) and the predicted radial deformations of the FEMs with different radial imperfections (Figures 57b-57d) demonstrate qualitative agreement. All results from the FEMs with radial imperfections show the largest radial outward deformation in the FWD ply-drop region between the 150° and 210° circumferential location. They also show a similar axisymmetric pattern with bands of inward dimples centered about the ±27-in. and ±26-in. axial positions in the measured and predicted radial deformations, respectively. However, the predicted global buckling initiation sites predicted with the FEMs were different for different radial imperfections. The FEM with the as-manufactured imperfection (Figure 57c) predicted potential initiation sites at 15° and 345° circumferential locations near the FWD ply-drop region, as well as at approximately the 200° circumferential location near the AFT ply-drop. The FEMs with as-installed radial imperfections predicted that the most likely locations for global buckling to initiate were at 190° and 170° near the AFT ply-drop.

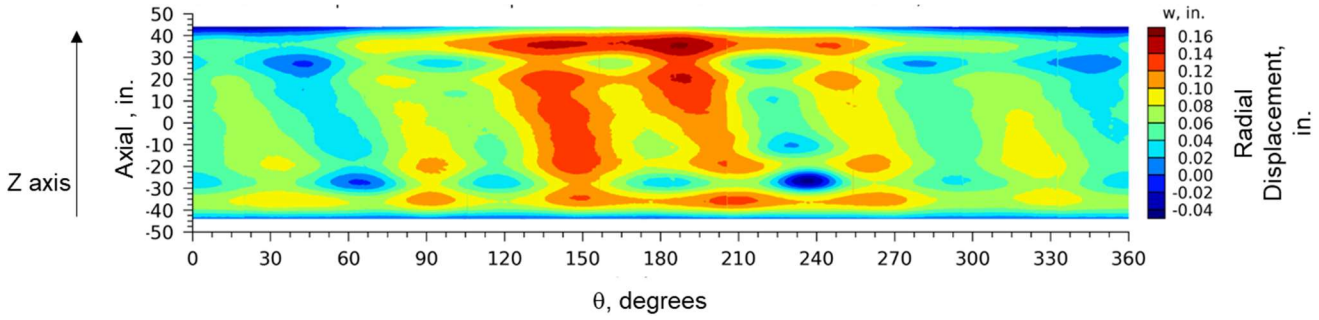

a) Measured radial deformation.

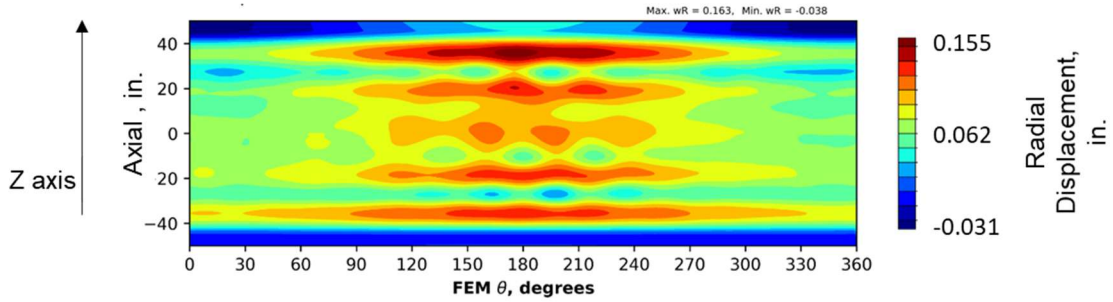

b) As-manufactured imperfection.

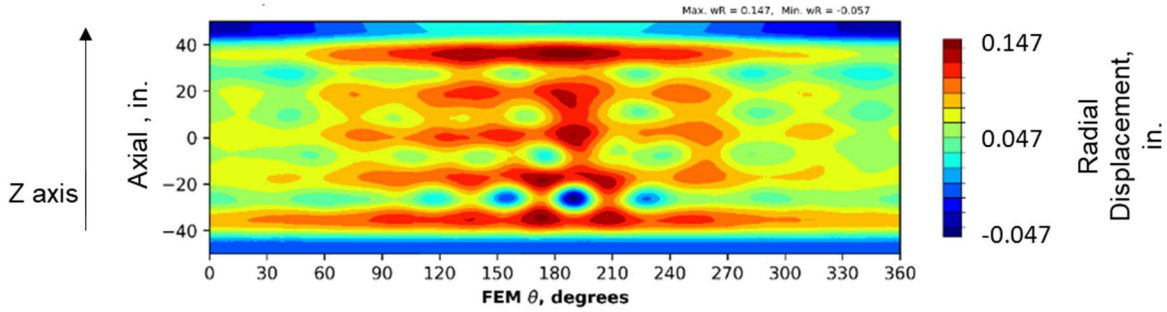

c) Pre-tare imperfection.

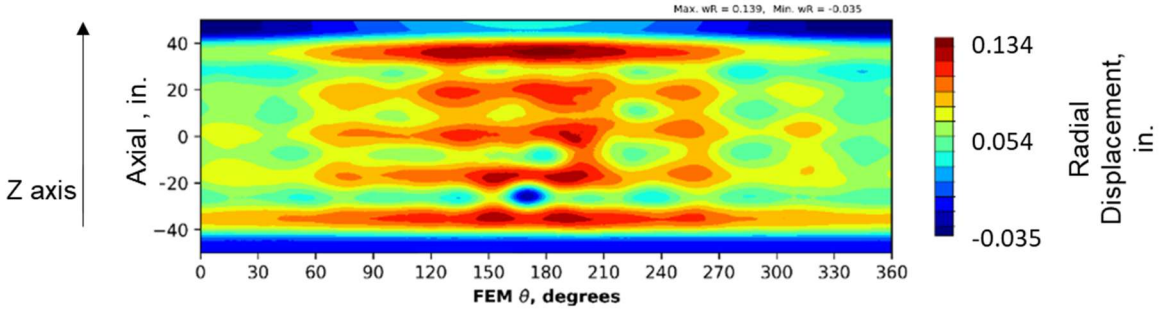

d) Tare imperfection.

Figure 57. Measured and predicted radial deformation contour of CTA3.8.

In summary, the influence of geometric imperfection on the prediction of buckling and global response of the CTA8.3 sandwich composite cylinder is presented in Figures 56 and 57. Although the FEM with the as-manufactured imperfection had the predicted buckling load within 7% of test results and buckling initiation near AFT ply-drop, the FEMs with as-installed radial imperfections matched the test buckling load within 0.1% and had a similar buckling pattern to test results. These finite element analysis results demonstrate the importance of obtaining realistic geometric imperfection input for nonlinear buckling analysis to predict the buckling response of a sandwich composite cylinder.

4.0 Concluding Remarks

The NASA Engineering and Safety Center (NESC) Shell Buckling Knockdown Factor (SBKF) Project is revisiting the NASA buckling design recommendations for a select class of composite launch-vehicle structures. A key part of this effort is the testing of large-scale composite buckling test articles and the prediction of the buckling response of test article SBKF-P3-CYL-CTA8.3 (Shell Buckling Knockdown Factor Phase 3 CYLinder Composite Test Article 8-ft-diamter design #3 or CTA8.3). Herein was presented a discussion of structural testing and analysis of CTA8.3, a sandwich composite cylindrical test article loaded to failure in combined axial compression and bending. During the final failure load sequence (LS12) conducted on December 19, 2019, CTA8.3 failed with the total applied load 432.0 kips at 86.4% P_{cr}^{CL}, the predicted linear buckling load for the perfect cylinder under the combined axial and bending loading of LS12 . The buckling occurred in the AFT section, approximately 27 in. below the axial midline and near the 240°circumferential location. Prior to testing, nondestructive evaluation indicated several spots of damage on the test article, but there was nothing in the test data to suggest that this damage influenced the overall response of CTA8.3.

The pretest predictions from geometrically nonlinear finite element analyses developed with the as-manufactured imperfections led to a predicted buckling load of 462 kips, 7% higher than the measured buckling load. While the radial deformation pattern and magnitudes at incipient buckling matched reasonably, the buckling initiation location predicted was different. In attempts to improve the test and analysis correlation, the finite element model (FEM) was modified to simulate the effect of two of the anomalies observed during test. The first anomaly is undesired movement of the upper test hardware during the ramp to tare, but analyses using this undesired movement of the upper test hardware did not give results appreciably different than the pretest predictions. The second anomaly considered was the change in the radial imperfection shape after CTA8.3 was installed in the test stand. The FEM predicted buckling response with as-installed radial imperfections showed excellent agreement with test results. Specifically, the experimental and predicted buckling loads were within 0.1% and the buckling response characteristics were similar. A third significant observation that was noted was uneven local axial displacements and strains near the AFT ring. This was caused at least in part by the test article moving axially in the AFT attachment ring in certain places, and that movement may have influenced the experimental buckling initiation site without changing the bucking load significantly. Due to the idealization in the FEM, this slipping in the attachment rings was not modeled.

5.0 References

1. Hilburger, M. W.: "Developing the Next Generation Shell Buckling Design Factors and Technologies," *53rd AIAA/ASME/ASCE/AHS/ASC Structures, Structural Dynamics and Materials Conference*, AIAA Paper 2012-1686, Honolulu, HI, April 2012.
2. Schultz, M. R.; Sleight, D. L.; Myers, D. E.; Waters, W. A. Jr.; Chunchu, P. B.; Lovejoy, A. E.; and Hilburger, M. W.: "Buckling Design and Imperfection Sensitivity of Sandwich Composite Launch-Vehicle Shell Structures," *Proceedings of the American Society for Composites: Thirty-First Technical Conference*, Williamsburg, Virginia, September 19–21, 2016. DEStech Publications, Inc., CD-ROM.
3. Schultz, M. R.; and Song, K.: "SBKF-P3-CYL-CTA8.3 Test Plan," NASA Langley Research Center, Hampton, VA, December 16, 2019.
4. Day, L.: "Test and Checkout Procedure: Shell Buckling Knockdown Factor Test #11 CTA8.3, SST-TCP-FP17.1," NASA Marshall Space Flight Center, Huntsville, AL, December 16, 2019.
5. Przekop, A.; Schultz, M. R.; Kosztowny, C. J.; Song, K., Lindell; M. C., Hilburger, M. W.; and Rudd, M. T.: "Design and Analysis of Buckling-Critical Large-Scale Sandwich Composite Cylindrical Test Articles," NASA/TM−20205008667, November 1, 2020.
6. Bomarito, G. F.; Hochhalter, J. D.; and Ruggles, T. J.: "Development of Optimal Multiscale Patterns for Digital Image Correlation via Local Greyscale Variations," *Experimental Mechanics* (2018) 58: 1169-1180. https://doi.org/10.1007/s11340-017-0348-1.
7. Anon.: ABAQUS™ 2016 Analysis User's Guide, Vols. I-V, Version 2016. Dassault Systèmes, Providence, RI, 2016.
8. Kosztowny, C. J. R.: "Implementing Geometric Surface Imperfections into Sandwich Composite Cylinder Finite Element Method Models." AIAA SciTech 2021, AIAA 2021-0439, January 2021, pp. 1–17. https://doi.org/10.2514/6.2021-0439.
9. Hilburger, M. W.; and Starnes, J. H.: "Effects of Imperfections of the Buckling Response of Composite Shells." *Thin-Walled Structures*, Vol. 42, No. 3, 2004, pp. 369–397. https://doi.org/10.1016/j.tws.2003.09.001.
10. Schultz, M. R.; Sleight, D. W.; Gardner, N. W.; Rudd, M. T.; Hilburger, M. W.; Palm, T.; and Oldfield, N. J.: "Test and analysis of a buckling-critical large-scale sandwich composite cylinder." *AIAA/ASCE/AHS/ASC Structures, Structural Dynamics, and Materials Conference*, AIAA 2018-1693, Orland, Florida, USA, 2018. American Institute of Aeronautics and Astronautics. https://doi.org/10.2514/6.2018-1693

Appendix A –Drawings

Contents:

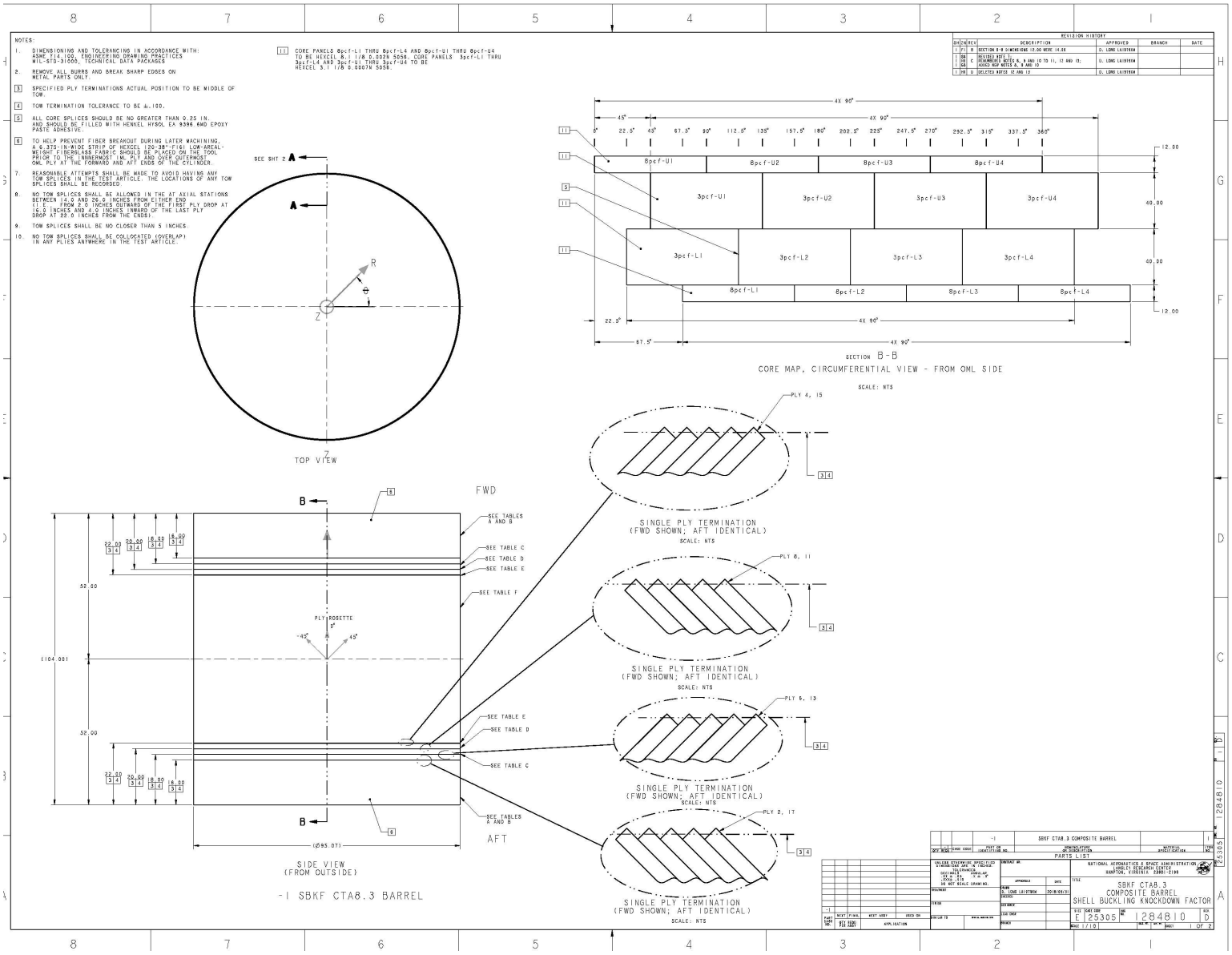

Figure A-1. CTA8.3 fabrication drawing, LaRC Drawing 1284810 Rev. D.

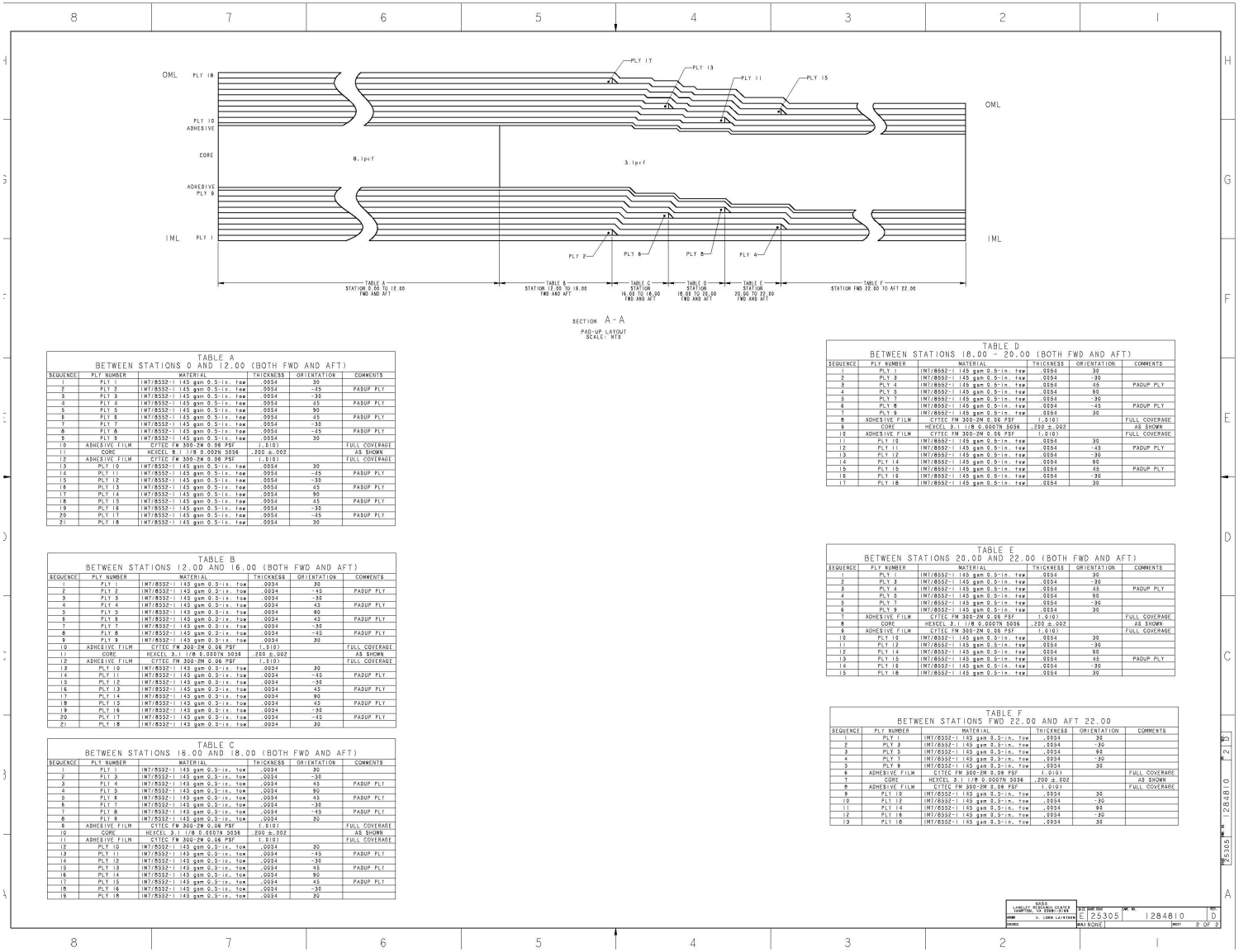

TABLE A
BETWEEN STATIONS 0 AND 12.00 (BOTH FWD AND AFT)

SEQUENCE	PLY NUMBER	MATERIAL	THICKNESS	ORIENTATION	COMMENTS
1	PLY 1	IM7/8552-1 145 gsm 0.5-in. tow	.0054	30	
2	PLY 2	IM7/8552-1 145 gsm 0.5-in. tow	.0054	-45	PADUP PLY
3	PLY 3	IM7/8552-1 145 gsm 0.5-in. tow	.0054	-30	
4	PLY 4	IM7/8552-1 145 gsm 0.5-in. tow	.0054	45	PADUP PLY
5	PLY 5	IM7/8552-1 145 gsm 0.5-in. tow	.0054	90	
6	PLY 8	IM7/8552-1 145 gsm 0.5-in. tow	.0054	45	PADUP PLY
7	PLY 7	IM7/8552-1 145 gsm 0.5-in. tow	.0054	-30	
8	PLY 8	IM7/8552-1 145 gsm 0.5-in. tow	.0054	-45	PADUP PLY
9	PLY 9	IM7/8552-1 145 gsm 0.5-in. tow	.0054	30	
10	ADHESIVE FILM	CYTEC FM 300-2M 0.06 PSF	(.010)		FULL COVERAGE
11	CORE	HEXCEL 3.1 1/8 0.0029 5056	.200 ±.002		AS SHOWN
12	ADHESIVE FILM	CYTEC FM 300-2M 0.06 PSF	(.010)		FULL COVERAGE
13	PLY 10	IM7/8552-1 145 gsm 0.5-in. tow	.0054	30	
14	PLY 11	IM7/8552-1 145 gsm 0.5-in. tow	.0054	-45	PADUP PLY
15	PLY 12	IM7/8552-1 145 gsm 0.5-in. tow	.0054	-30	
16	PLY 13	IM7/8552-1 145 gsm 0.5-in. tow	.0054	45	PADUP PLY
17	PLY 14	IM7/8552-1 145 gsm 0.5-in. tow	.0054	90	
18	PLY 15	IM7/8552-1 145 gsm 0.5-in. tow	.0054	45	PADUP PLY
19	PLY 16	IM7/8552-1 145 gsm 0.5-in. tow	.0054	-30	
20	PLY 17	IM7/8552-1 145 gsm 0.5-in. tow	.0054	-45	PADUP PLY
21	PLY 18	IM7/8552-1 145 gsm 0.5-in. tow	.0054	30	

TABLE B
BETWEEN STATIONS 12.00 AND 16.00 (BOTH FWD AND AFT)

SEQUENCE	PLY NUMBER	MATERIAL	THICKNESS	ORIENTATION	COMMENTS
1	PLY 1	IM7/8552-1 145 gsm 0.3-in. tow	.0034	30	
2	PLY 2	IM7/8552-1 145 gsm 0.3-in. tow	.0034	-45	PADUP PLY
3	PLY 3	IM7/8552-1 145 gsm 0.3-in. tow	.0034	-30	
4	PLY 4	IM7/8552-1 145 gsm 0.3-in. tow	.0034	45	PADUP PLY
5	PLY 5	IM7/8552-1 145 gsm 0.3-in. tow	.0034	90	
6	PLY 8	IM7/8552-1 145 gsm 0.3-in. tow	.0034	45	PADUP PLY
7	PLY 7	IM7/8552-1 145 gsm 0.3-in. tow	.0034	-30	
8	PLY 8	IM7/8552-1 145 gsm 0.3-in. tow	.0034	-45	PADUP PLY
9	PLY 9	IM7/8552-1 145 gsm 0.3-in. tow	.0034	30	
10	ADHESIVE FILM	CYTEC FM 300-2M 0.06 PSF	(.010)		FULL COVERAGE
11	CORE	HEXCEL 3.1 1/8 0.0007N 5056	.200 ±.002		AS SHOWN
12	ADHESIVE FILM	CYTEC FM 300-2M 0.06 PSF	(.010)		FULL COVERAGE
13	PLY 10	IM7/8552-1 145 gsm 0.3-in. tow	.0034	30	
14	PLY 11	IM7/8552-1 145 gsm 0.3-in. tow	.0034	-45	PADUP PLY
15	PLY 12	IM7/8552-1 145 gsm 0.3-in. tow	.0034	-30	
16	PLY 13	IM7/8552-1 145 gsm 0.3-in. tow	.0034	45	PADUP PLY
17	PLY 14	IM7/8552-1 145 gsm 0.3-in. tow	.0034	90	
18	PLY 15	IM7/8552-1 145 gsm 0.3-in. tow	.0034	45	PADUP PLY
19	PLY 16	IM7/8552-1 145 gsm 0.3-in. tow	.0034	-30	
20	PLY 17	IM7/8552-1 145 gsm 0.3-in. tow	.0034	-45	PADUP PLY
21	PLY 18	IM7/8552-1 145 gsm 0.3-in. tow	.0034	30	

TABLE C
BETWEEN STATIONS 16.00 AND 18.00 (BOTH FWD AND AFT)

SEQUENCE	PLY NUMBER	MATERIAL	THICKNESS	ORIENTATION	COMMENTS
1	PLY 1	IM7/8552-1 145 gsm 0.3-in. tow	.0034	30	
2	PLY 3	IM7/8552-1 145 gsm 0.3-in. tow	.0034	-30	
3	PLY 4	IM7/8552-1 145 gsm 0.3-in. tow	.0034	45	PADUP PLY
4	PLY 5	IM7/8552-1 145 gsm 0.3-in. tow	.0034	90	
5	PLY 8	IM7/8552-1 145 gsm 0.3-in. tow	.0034	45	PADUP PLY
6	PLY 7	IM7/8552-1 145 gsm 0.3-in. tow	.0034	-30	
7	PLY 8	IM7/8552-1 145 gsm 0.3-in. tow	.0034	-45	PADUP PLY
8	PLY 9	IM7/8552-1 145 gsm 0.3-in. tow	.0034	30	
9	ADHESIVE FILM	CYTEC FM 300-2M 0.06 PSF	(.010)		FULL COVERAGE
10	CORE	HEXCEL 3.1 1/8 0.0007N 5056	.200 ±.002		AS SHOWN
11	ADHESIVE FILM	CYTEC FM 300-2M 0.06 PSF	(.010)		FULL COVERAGE
12	PLY 10	IM7/8552-1 145 gsm 0.3-in. tow	.0034	30	
13	PLY 11	IM7/8552-1 145 gsm 0.3-in. tow	.0034	-45	PADUP PLY
14	PLY 12	IM7/8552-1 145 gsm 0.3-in. tow	.0034	-30	
15	PLY 13	IM7/8552-1 145 gsm 0.3-in. tow	.0034	45	PADUP PLY
16	PLY 14	IM7/8552-1 145 gsm 0.3-in. tow	.0034	90	
17	PLY 15	IM7/8552-1 145 gsm 0.3-in. tow	.0034	45	PADUP PLY
18	PLY 16	IM7/8552-1 145 gsm 0.3-in. tow	.0034	-30	
19	PLY 18	IM7/8552-1 145 gsm 0.3-in. tow	.0034	30	

TABLE D
BETWEEN STATIONS 18.00 - 20.00 (BOTH FWD AND AFT)

SEQUENCE	PLY NUMBER	MATERIAL	THICKNESS	ORIENTATION	COMMENTS
1	PLY 1	IM7/8552-1 145 gsm 0.5-in. tow	.0054	30	
2	PLY 3	IM7/8552-1 145 gsm 0.5-in. tow	.0054	-30	
3	PLY 4	IM7/8552-1 145 gsm 0.5-in. tow	.0054	45	PADUP PLY
4	PLY 5	IM7/8552-1 145 gsm 0.5-in. tow	.0054	90	
5	PLY 7	IM7/8552-1 145 gsm 0.5-in. tow	.0054	-30	
6	PLY 8	IM7/8552-1 145 gsm 0.5-in. tow	.0054	-45	PADUP PLY
7	PLY 9	IM7/8552-1 145 gsm 0.5-in. tow	.0054	30	
8	ADHESIVE FILM	CYTEC FM 300-2M 0.06 PSF	(.010)		FULL COVERAGE
9	CORE	HEXCEL 3.1 1/8 0.0007N 5056	.200 ±.002		AS SHOWN
10	ADHESIVE FILM	CYTEC FM 300-2M 0.06 PSF	(.010)		FULL COVERAGE
11	PLY 10	IM7/8552-1 145 gsm 0.5-in. tow	.0054	30	
12	PLY 11	IM7/8552-1 145 gsm 0.5-in. tow	.0054	-45	PADUP PLY
13	PLY 12	IM7/8552-1 145 gsm 0.5-in. tow	.0054	-30	
14	PLY 14	IM7/8552-1 145 gsm 0.5-in. tow	.0054	90	
15	PLY 15	IM7/8552-1 145 gsm 0.5-in. tow	.0054	45	PADUP PLY
16	PLY 16	IM7/8552-1 145 gsm 0.5-in. tow	.0054	-30	
17	PLY 18	IM7/8552-1 145 gsm 0.5-in. tow	.0054	30	

TABLE E
BETWEEN STATIONS 20.00 AND 22.00 (BOTH FWD AND AFT)

SEQUENCE	PLY NUMBER	MATERIAL	THICKNESS	ORIENTATION	COMMENTS
1	PLY 1	IM7/8552-1 145 gsm 0.5-in. tow	.0054	30	
2	PLY 3	IM7/8552-1 145 gsm 0.5-in. tow	.0054	-30	
3	PLY 4	IM7/8552-1 145 gsm 0.5-in. tow	.0054	45	PADUP PLY
4	PLY 5	IM7/8552-1 145 gsm 0.5-in. tow	.0054	90	
5	PLY 7	IM7/8552-1 145 gsm 0.5-in. tow	.0054	-30	
6	PLY 9	IM7/8552-1 145 gsm 0.5-in. tow	.0054	30	
7	ADHESIVE FILM	CYTEC FM 300-2M 0.06 PSF	(.010)		FULL COVERAGE
8	CORE	HEXCEL 3.1 1/8 0.0007N 5056	.200 ±.002		AS SHOWN
9	ADHESIVE FILM	CYTEC FM 300-2M 0.06 PSF	(.010)		FULL COVERAGE
10	PLY 10	IM7/8552-1 145 gsm 0.5-in. tow	.0054	30	
11	PLY 12	IM7/8552-1 145 gsm 0.5-in. tow	.0054	-30	
12	PLY 14	IM7/8552-1 145 gsm 0.5-in. tow	.0054	90	
13	PLY 15	IM7/8552-1 145 gsm 0.5-in. tow	.0054	45	PADUP PLY
14	PLY 16	IM7/8552-1 145 gsm 0.5-in. tow	.0054	-30	
15	PLY 18	IM7/8552-1 145 gsm 0.5-in. tow	.0054	30	

TABLE F
BETWEEN STATIONS FWD 22.00 AND AFT 22.00

SEQUENCE	PLY NUMBER	MATERIAL	THICKNESS	ORIENTATION	COMMENTS
1	PLY 1	IM7/8552-1 145 gsm 0.3-in. tow	.0034	30	
2	PLY 3	IM7/8552-1 145 gsm 0.3-in. tow	.0034	-30	
3	PLY 5	IM7/8552-1 145 gsm 0.3-in. tow	.0034	90	
4	PLY 7	IM7/8552-1 145 gsm 0.3-in. tow	.0034	-30	
5	PLY 9	IM7/8552-1 145 gsm 0.3-in. tow	.0034	30	
6	ADHESIVE FILM	CYTEC FM 300-2M 0.06 PSF	(.010)		FULL COVERAGE
7	CORE	HEXCEL 3.1 1/8 0.0007N 5056	.200 ±.002		AS SHOWN
8	ADHESIVE FILM	CYTEC FM 300-2M 0.06 PSF	(.010)		FULL COVERAGE
9	PLY 10	IM7/8552-1 145 gsm 0.3-in. tow	.0034	30	
10	PLY 12	IM7/8552-1 145 gsm 0.3-in. tow	.0034	-30	
11	PLY 14	IM7/8552-1 145 gsm 0.3-in. tow	.0034	90	
12	PLY 16	IM7/8552-1 145 gsm 0.3-in. tow	.0034	-30	
13	PLY 18	IM7/8552-1 145 gsm 0.3-in. tow	.0034	30	

NASA LANGLEY RESEARCH CENTER HAMPTON, VA 23681-2199
DRAWN: D. LONG LAITSTEIN
SIZE: E | DWG NO: 25305 | REV: 1284810 | SHT: D
MATERIAL: NONE | SHEET 2 OF 2

Figure A-1. CTA8.3 fabrication drawing, LaRC Drawing 1284810 Rev. D (concluded).

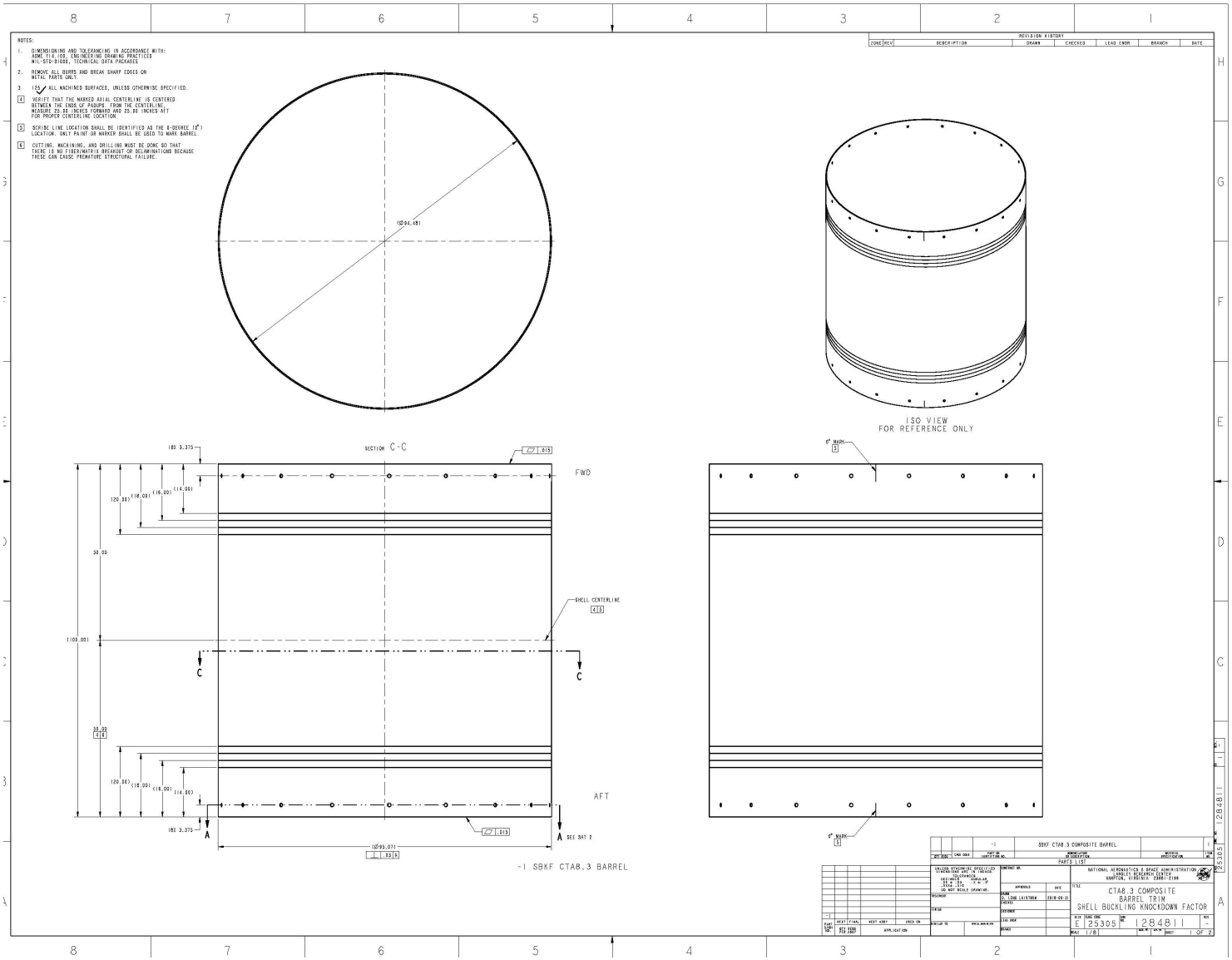

Figure A-1. CTA8.3 trim, LaRC Drawing 1284811.

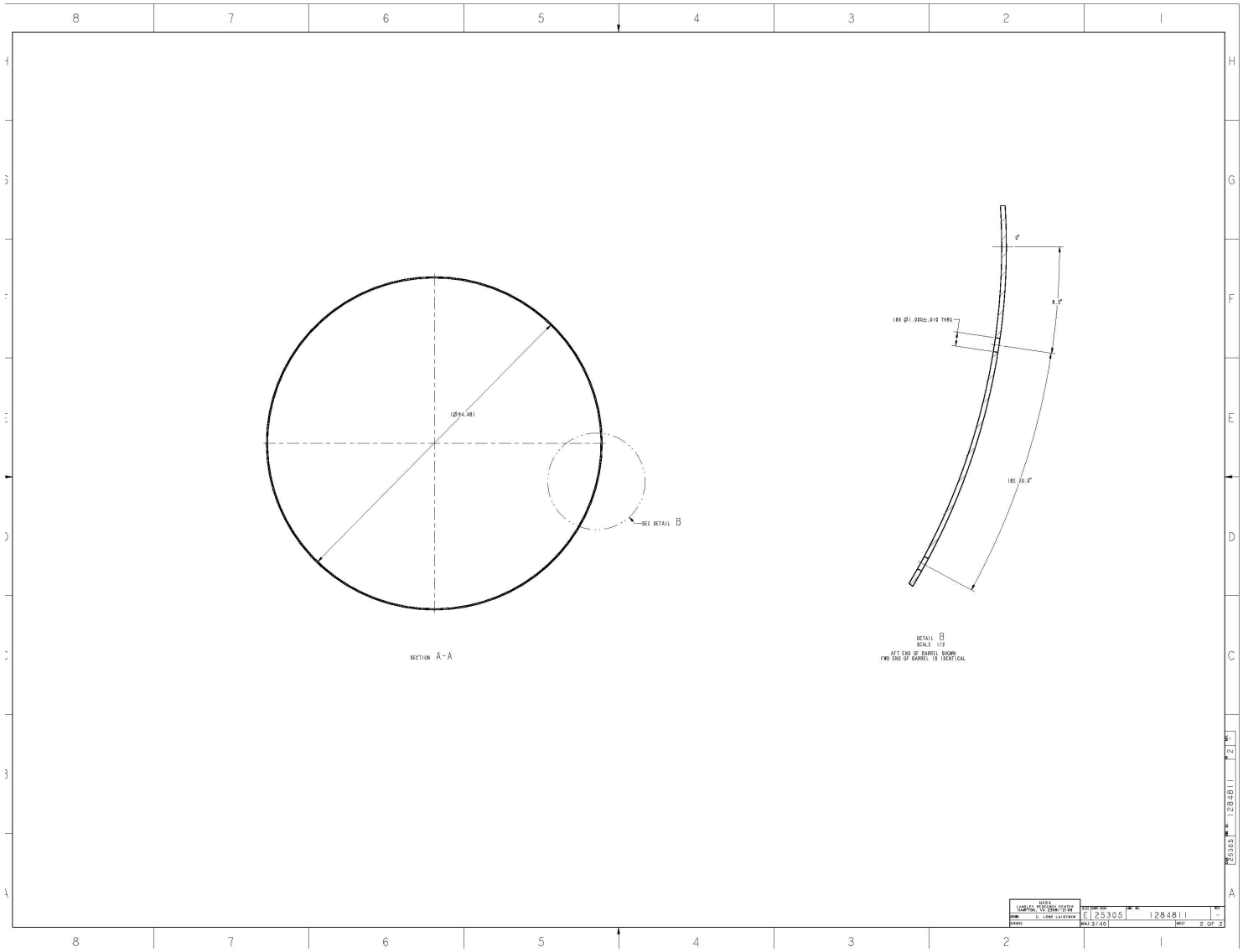

Figure A-2. CTA8.3 trim, LaRC Drawing 1284811 (concluded).

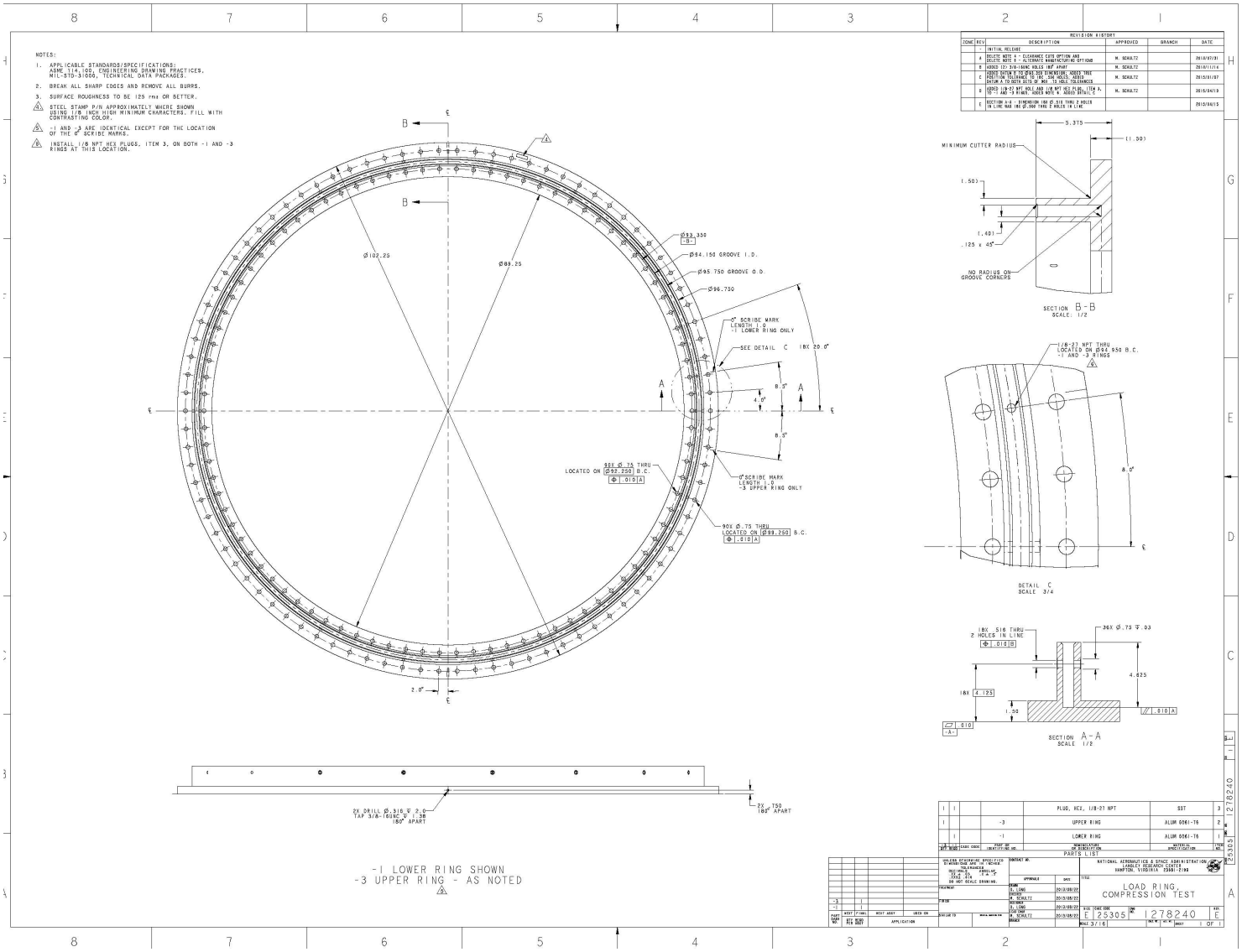

Figure A-3. Test-article attachment ring design, LaRC Drawing 1278240 Rev. E.

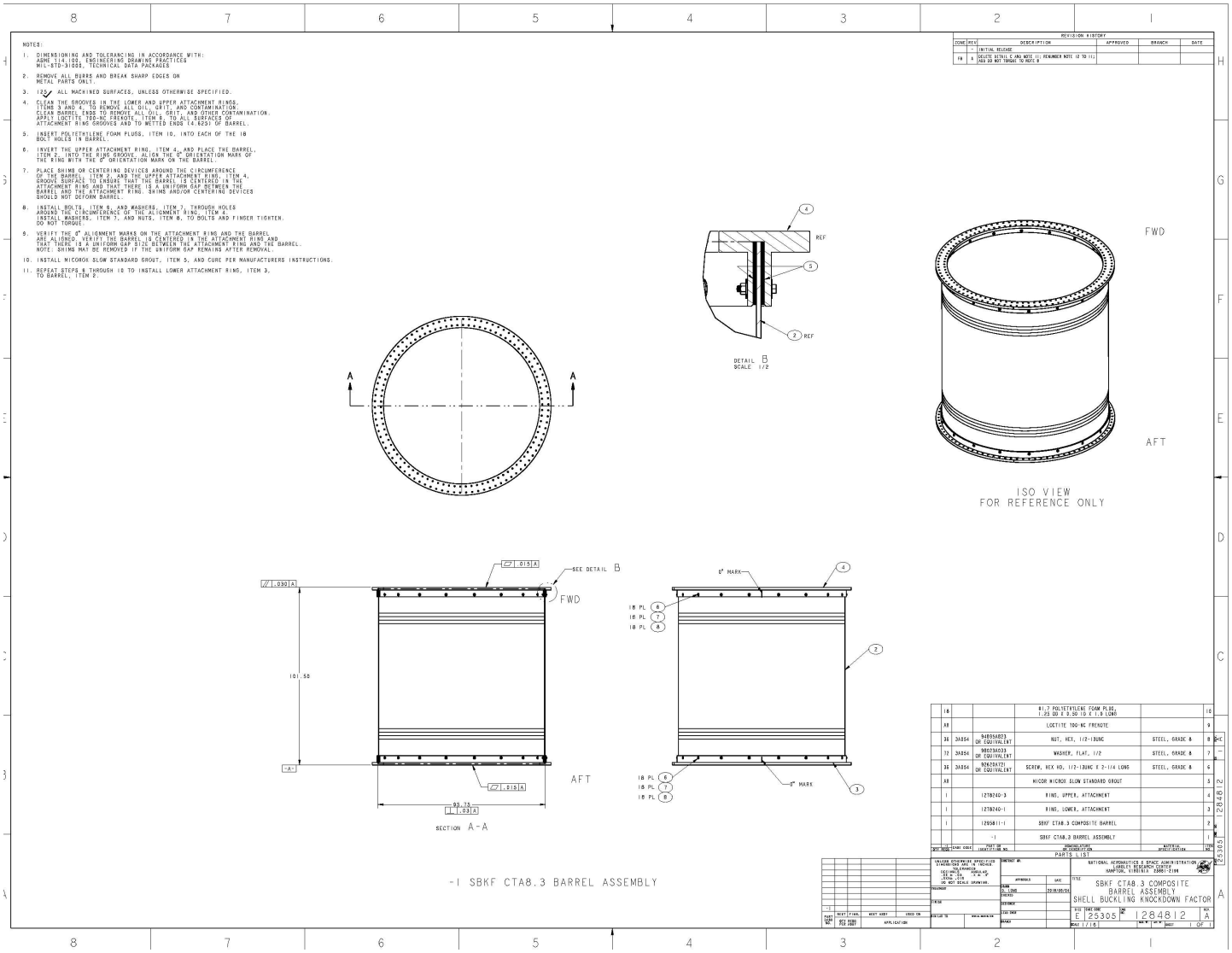

Figure A-4. CTA8.3 assembly drawing, LaRC Drawing 1284812 Rev. E.

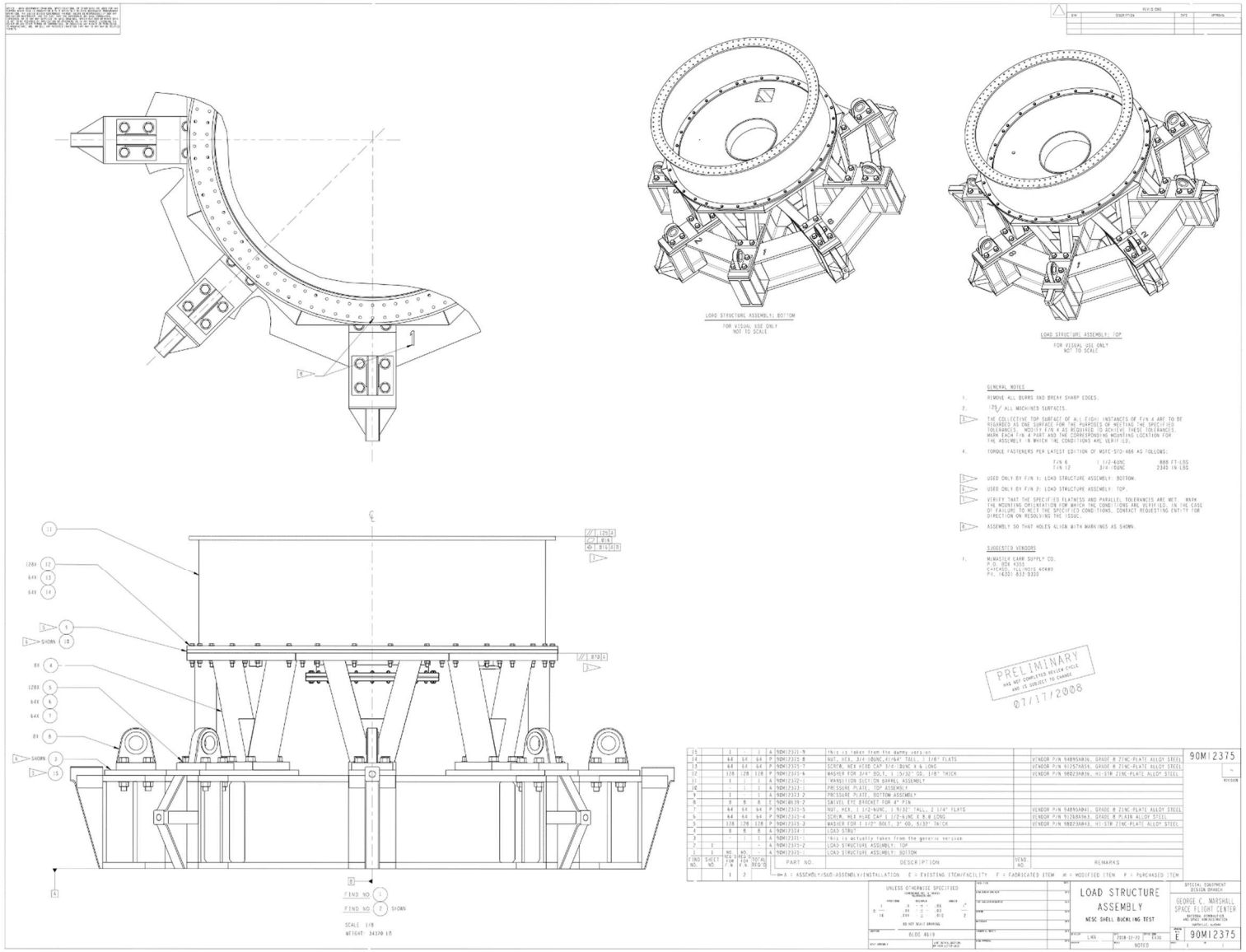

Figure A-5. Load structure assembly, MSFC Drawing 90M12375.

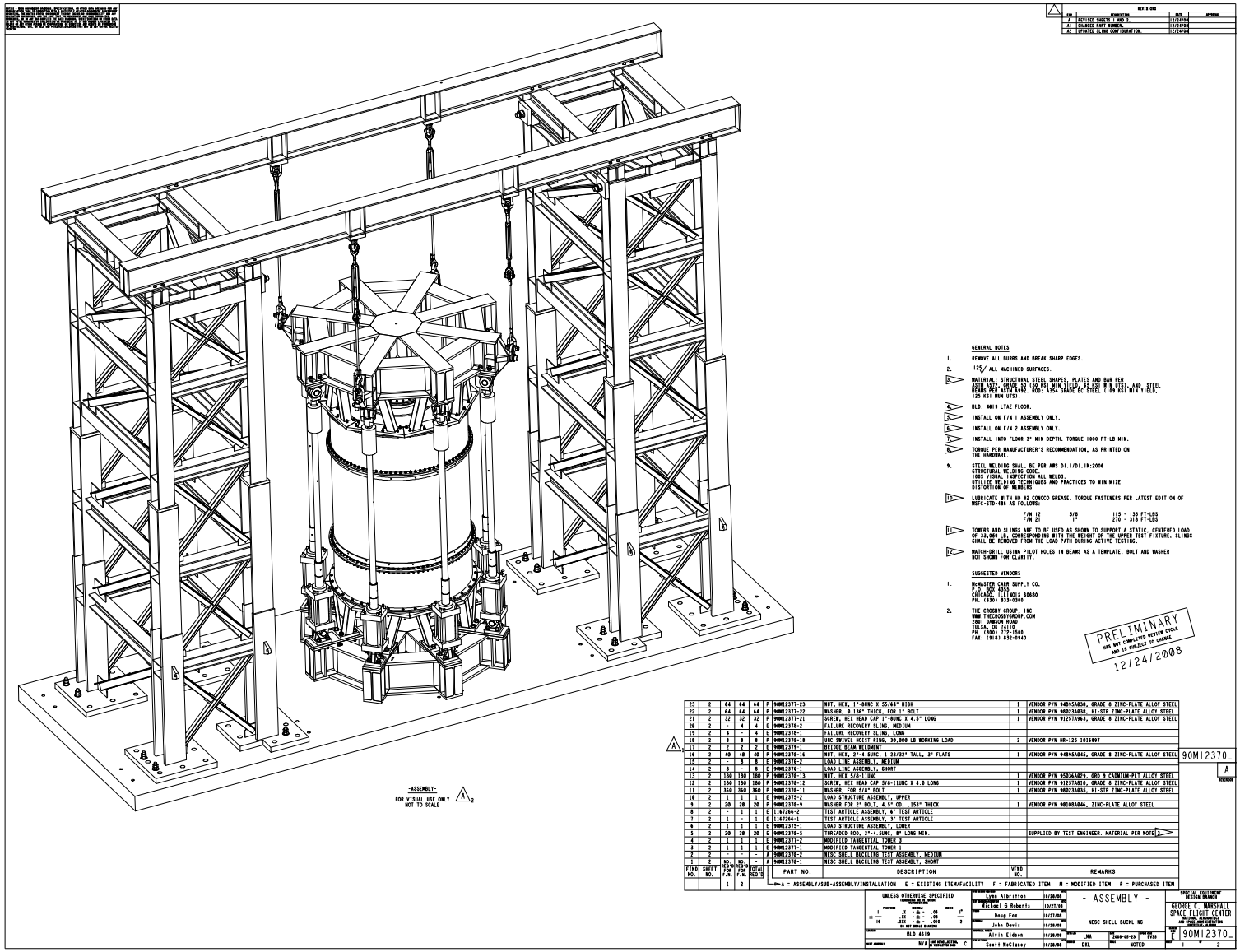

FIND NO.	SHEET NO.	QTY REQ'D FOR F.W.	QTY REQ'D FOR F.W.	TOTAL REQ'D		PART NO.	DESCRIPTION	VEND. NO.	REMARKS
23	2	64	64	64	P	90M12377-23	NUT, HEX, 1"-8UNC X 55/64" HIGH	1	VENDOR P/N 94895A838, GRADE B ZINC-PLATE ALLOY STEEL
22	2	64	64	64	P	90M12377-22	WASHER, 0.134" THICK, FOR 1" BOLT	1	VENDOR P/N 98823A838, H1-STR ZINC-PLATE ALLOY STEEL
21	2	32	32	32	P	90M12377-21	SCREW, HEX HEAD CAP 1"-8UNC X 4.5" LONG	1	VENDOR P/N 91257A963, GRADE B ZINC-PLATE ALLOY STEEL
20	2	-	4	4	E	90M12378-2	FAILURE RECOVERY SLING, MEDIUM		
19	2	4	-	4	E	90M12378-1	FAILURE RECOVERY SLING, LONG		
18	2	8	8	8	P	90M12378-18	UNC SWIVEL HOIST RING, 30,000 LB WORKING LOAD	2	VENDOR P/N HR-125 1816997
17	2	2	2	2	E	90M12379-1	BRIDGE BEAM WELDMENT		
16	2	40	40	40	P	90M12378-16	NUT, HEX, 2"-4.5UNC, 1 23/32" TALL, 3" FLATS	1	VENDOR P/N 94895A845, GRADE B ZINC-PLATE ALLOY STEEL
15	2	-	8	8	E	90M12376-2	LOAD LINE ASSEMBLY, MEDIUM		
14	2	8	-	8	E	90M12376-1	LOAD LINE ASSEMBLY, SHORT		
13	2	100	100	100	P	90M12378-13	NUT, HEX 5/8-11UNC	1	VENDOR P/N 95063A079, GRD 9 CADMIUM-PLT ALLOY STEEL
12	2	100	100	100	P	90M12378-12	SCREW, HEX HEAD CAP 5/8-11UNC X 4.0 LONG	1	VENDOR P/N 91257A818, GRADE B ZINC-PLATE ALLOY STEEL
11	2	360	360	360	P	90M12378-11	WASHER, FOR 5/8" BOLT	1	VENDOR P/N 98823A835, H1-STR ZINC-PLATE ALLOY STEEL
10	2	1	1	1	E	90M12375-2	LOAD STRUCTURE ASSEMBLY, UPPER		
9	2	20	20	20	P	90M12378-9	WASHER FOR 2" BOLT, 4.5" OD, .153" THICK	1	VENDOR P/N 90108A846, ZINC-PLATE ALLOY STEEL
8	2	-	1	1	E	1167266-2	TEST ARTICLE ASSEMBLY, 6' TEST ARTICLE		
7	2	1	-	1	E	1167266-1	TEST ARTICLE ASSEMBLY, 3' TEST ARTICLE		
6	2	1	1	1	E	90M12375-1	LOAD STRUCTURE ASSEMBLY, LOWER		
5	2	20	20	20	E	90M12378-5	THREADED ROD, 2"-4.5UNC, 8' LONG MIN.		SUPPLIED BY TEST ENGINEER. MATERIAL PER NOTE 3
4	2	1	1	1	E	90M12377-2	MODIFIED TANGENTIAL TOWER 3		
3	2	1	1	1	E	90M12377-1	MODIFIED TANGENTIAL TOWER 1		
2	2	-	-	-	A	90M12378-2	NESC SHELL BUCKLING TEST ASSEMBLY, MEDIUM		
1	2	90	90	-	A	90M12378-1	NESC SHELL BUCKLING TEST ASSEMBLY, SHORT		

A = ASSEMBLY/SUB-ASSEMBLY/INSTALLATION E = EXISTING ITEM/FACILITY F = FABRICATED ITEM M = MODIFIED ITEM P = PURCHASED ITEM

Figure A-6. Load structure assembly, MSFC Drawing 90M12370.

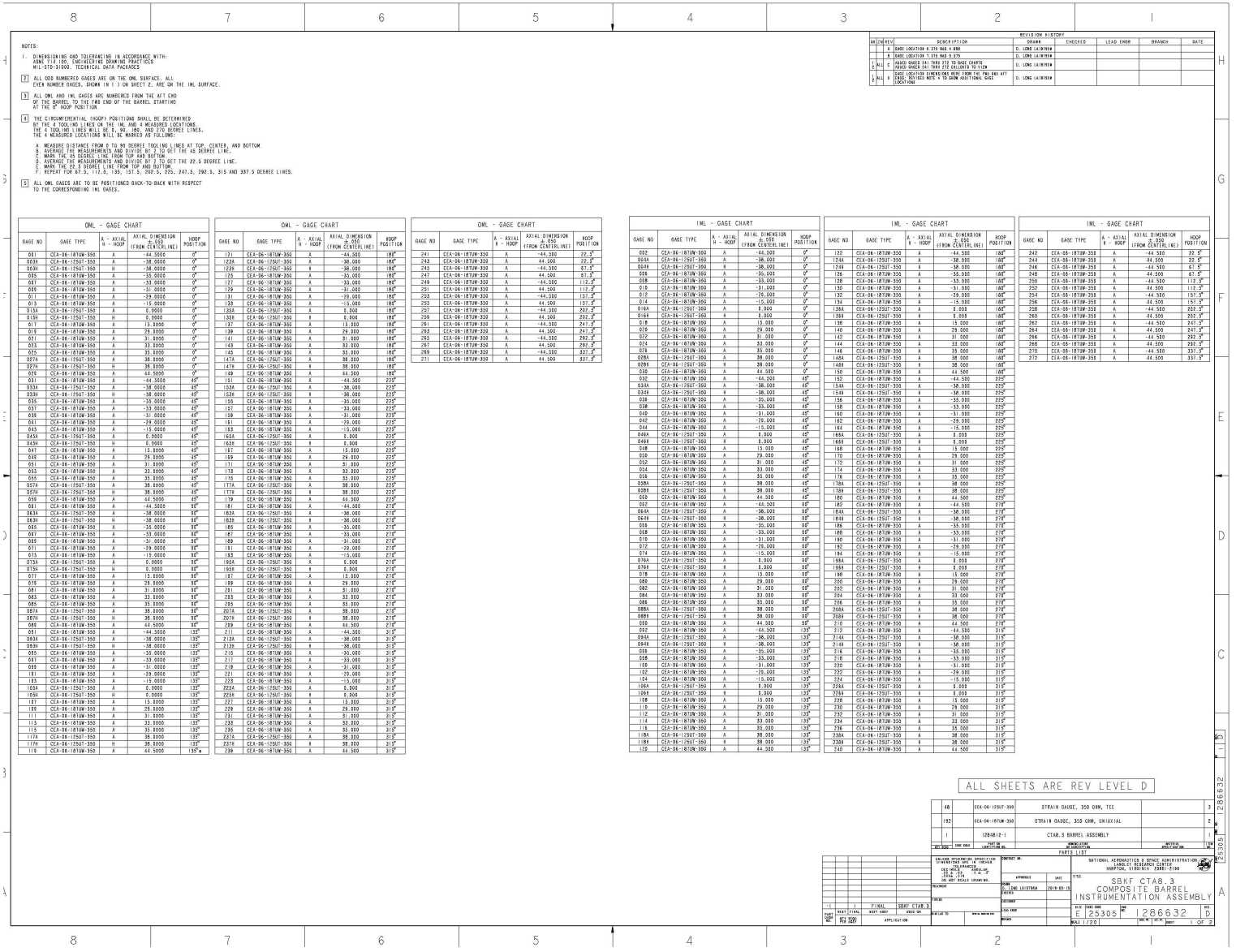

Figure A-7. Strain-gage instrumentation drawing, LaRC Drawing 1286632 RevD.

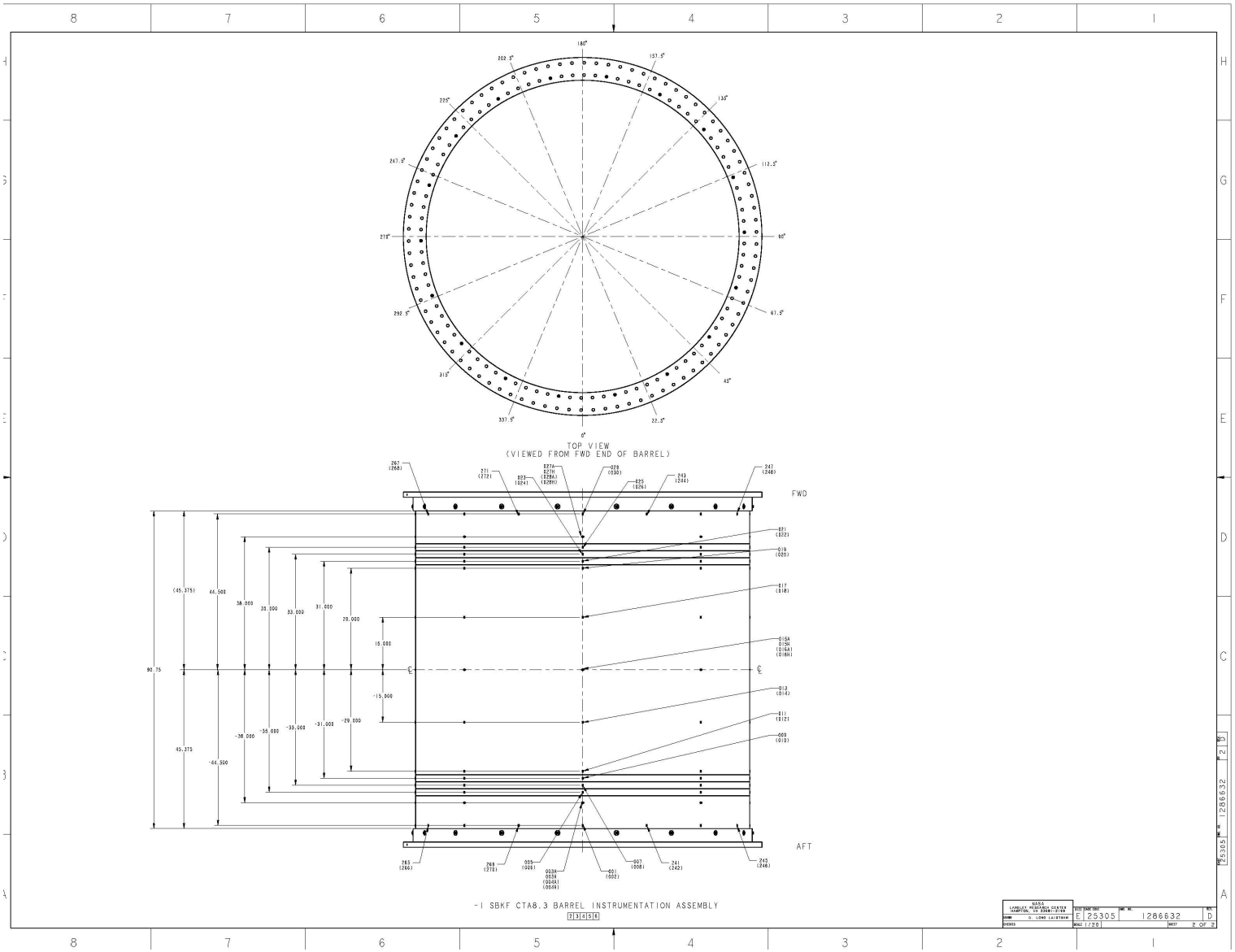

Figure A-7. Strain-gage instrumentation drawing, LaRC Drawing 1286632 RevD (concluded).

Appendix B – Shearography Inspection Report

Work that resulted in the following report was performed under NASA Purchase Order (PO) 19N0299 and contract 80MSFC18C0011.

Inspected June 4/5, 2019

At MSFC

Prepared by

John W. Newman, NAS410 Shearography LIII

Eben C. Arnold, Process Engineer

Laser Technology Inc.

Shearography Inspection Report: NASA Test Barrel Section

Background

LTI was contracted to perform a shearography inspection of a test barrel consisting of 5-core-5 sandwich construction with carbon fiber laminate face sheets and a low density aluminum honeycomb core. The dimensions of the barrel section is: axial length= 100 inches, O.D.= 95.07 inches.

The test procedure was to use vacuum shearography for scanning and both vacuum and thermal stress shearography if any anomaly was detected. A total of (16) anomalies were detected and measured. (15) were located on the Outer Mold Line (OML) also the bag side, and (1) weak indication (#11) was on the Inner Mold Line, also the Tool Side. #16 appeared with both thermal and vacuum tests. We recommend secondary NDT of this indication.

Equipment

The equipment used, was NASA owned LTI-5200 Vacuum /Thermal Shearography System. Although capable of single person operation, speed and data management requirements called for a two-person test. The 5200 uses a fixed shear vector optical system and factory calibration.

Test Parameters were:

1. Vacuum Lock Level of 30 inches H2O
2. Vacuum Test ΔV = 13 in. H2O (0.5 psi)
3. Thermal Stress, RBF, T=8 seconds, t= 6 seconds

Indications were numbered sequentially as detected, measured and a piece of masking take place directly over the center of the tape. The positioning of the tape marker was verified by a vacuum re-test.

Map of Shearography Indication for Test Barrel Section s/n 001 (June 4/5, 2019)

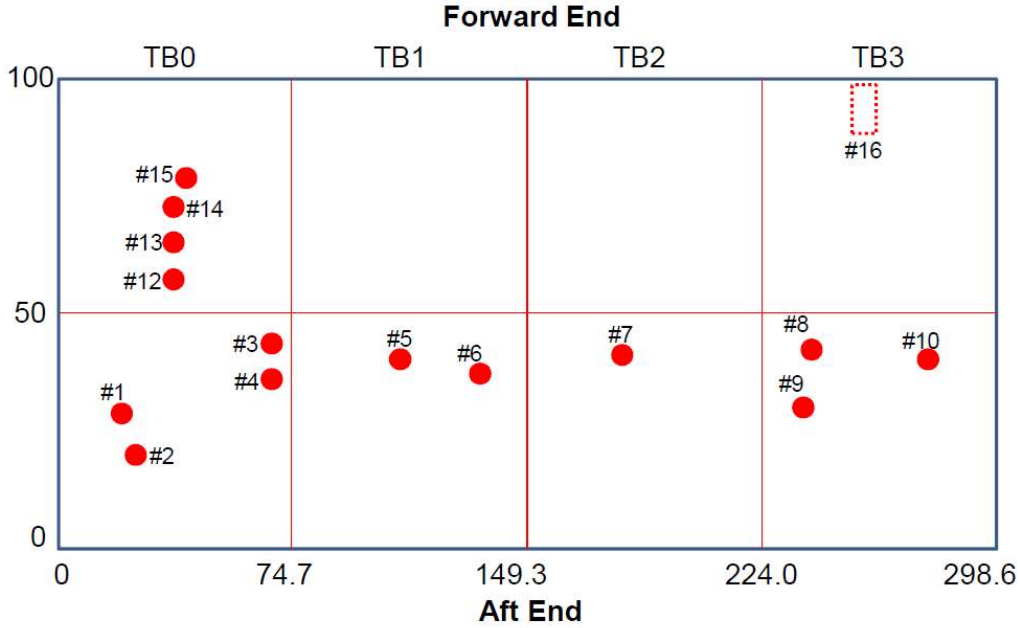

1. Indication Locations are measured from (0,0)
2. All dimensions are in inches.

Test Barrel Section S/N 001
Shearography Test Results

Indication Locations (X,Y) are in inches from
the (0,0) location at the AFT Corner of TBO

Shearography Indications

#001
Dims: Basin 0.8x0.7 inches
Location: AFT OML, TB0 (21.0, 27.3in.)
Comments: A basin is seen around the stronger indication indicating a probable low velocity.

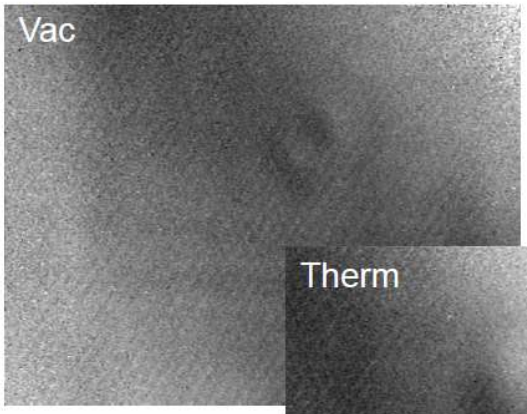

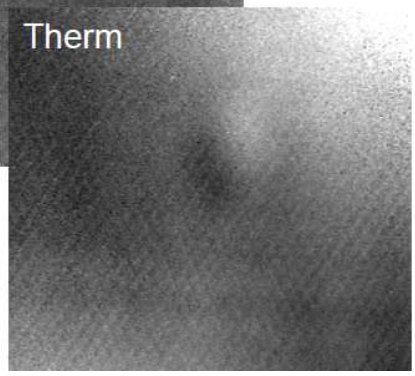

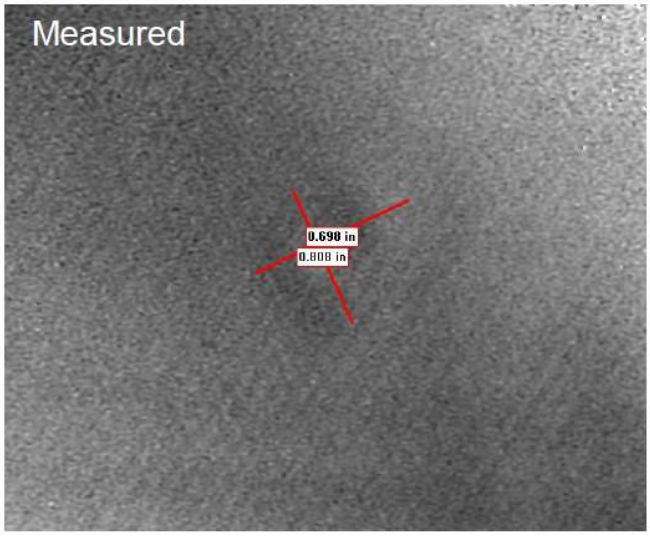

#002

Dims: Basin 1.5x0.7 inches

Location: AFT OML, TB0 (22.0, 21.0in.)

Comments: A basin is seen around the stronger indication indicating a probable low velocity.

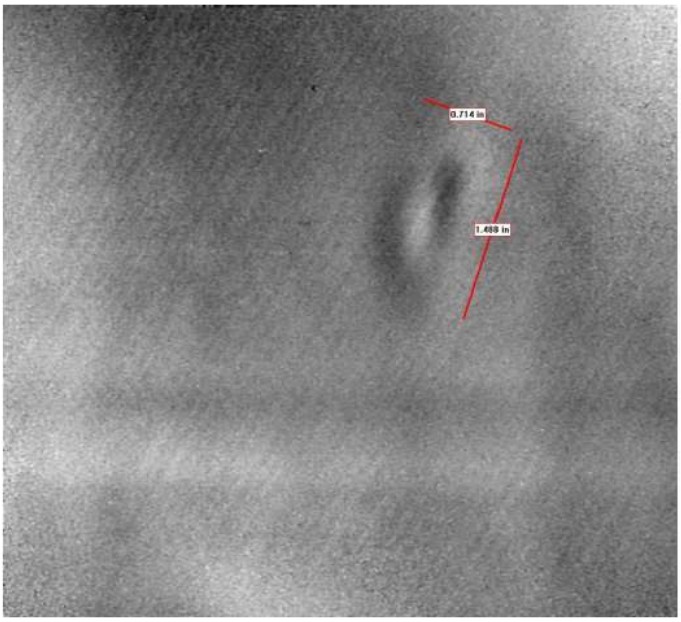

#003

Dims: Basin 0.7x1.2 inches

Location: AFT OML, TB0 (72.6 x 41.5in.)

Comments: A basin is seen around the stronger indication indicating a probable low velocity.

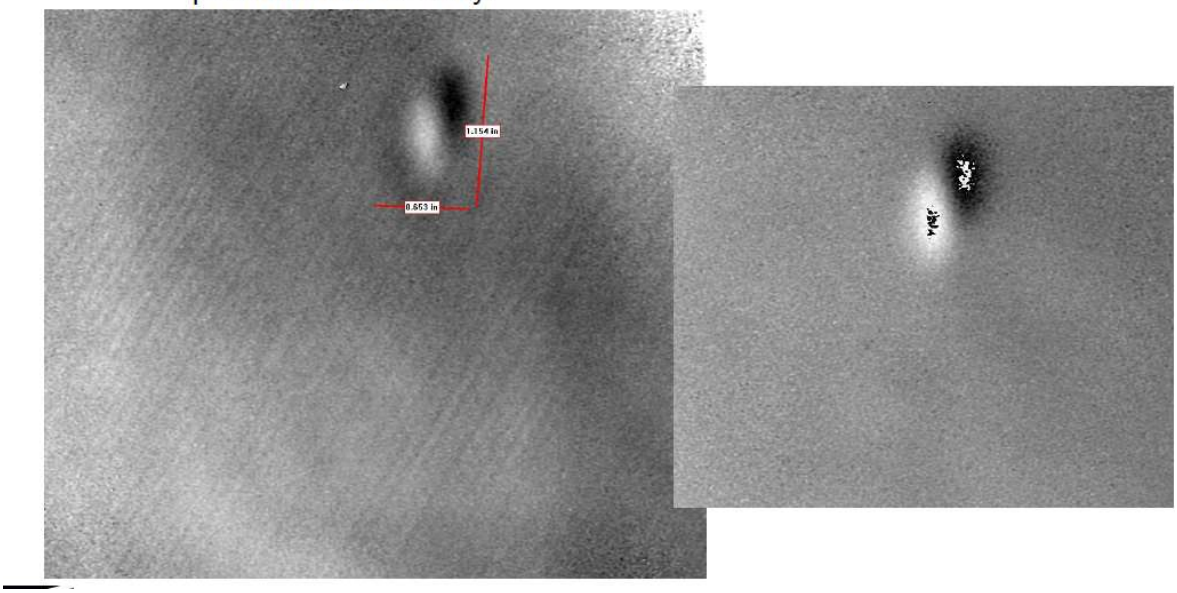

#004
Dims: Basin 0.81x0.70 inches
Location: AFT OML, TB0 (72.6, 34.5in.)
Comments: Honeycomb core appears attached to the face sheet over the indication, suggesting a core anomaly as opposed to a disbond.

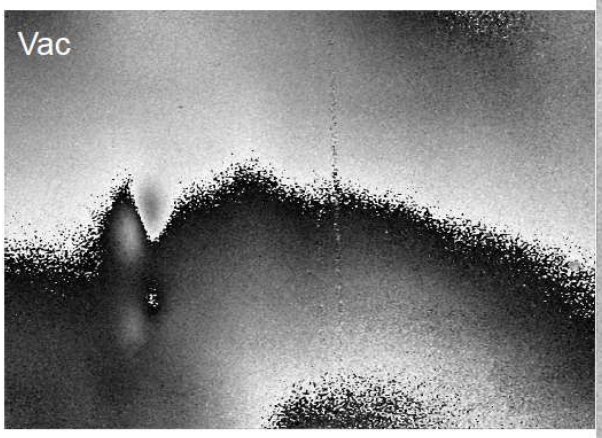

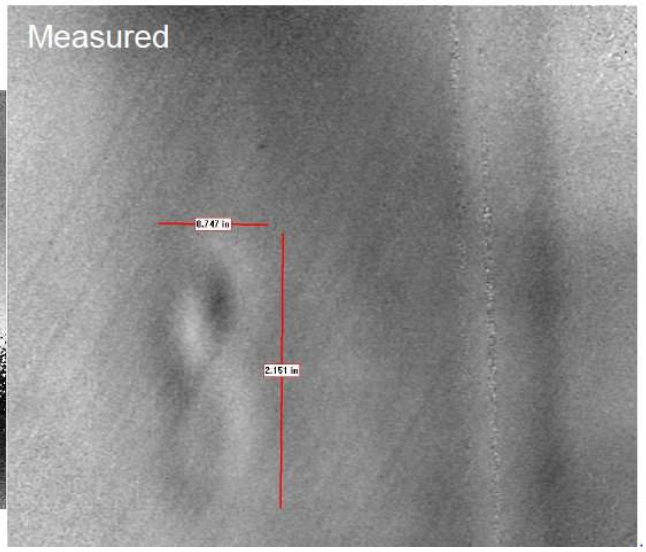

#005
Dims: 0.35 x 0.28 inches
Location: AFT OML, TB0 (100.6, 35.8in.)
Comments: probable core anomaly as opposed to a disbond.

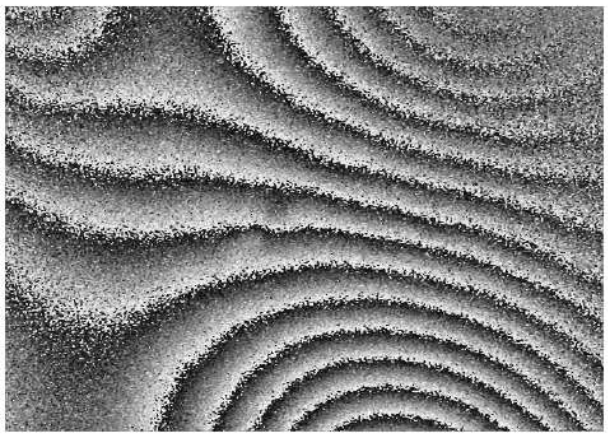

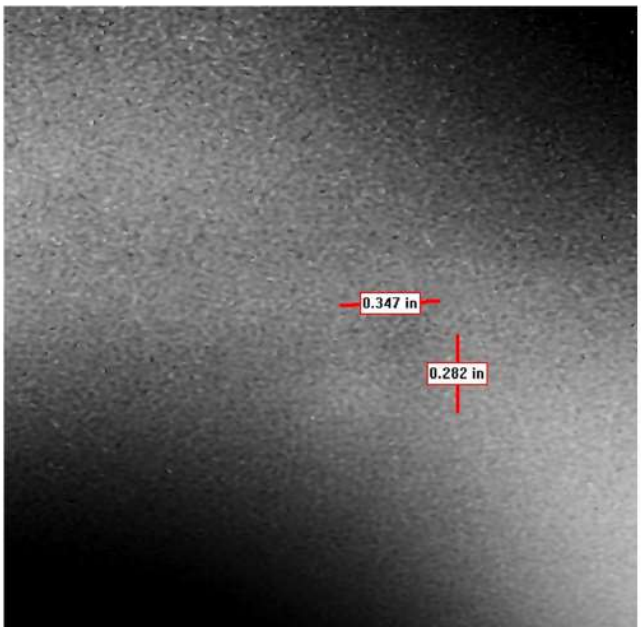

#006
Dims: 0.37 x 0.23 inches
Location: AFT OML, TB0 (137.4, 35.3in.)
Comments: probable core anomaly as opposed to a disbond.

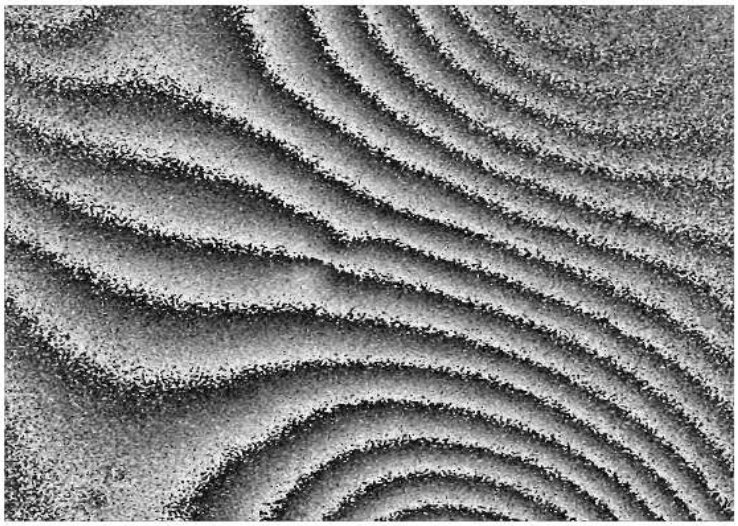

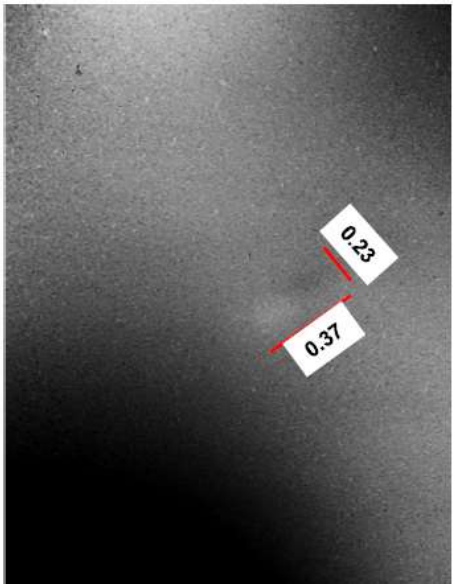

#007
Dims: Basin 0.51 x 0.29 inches
Location: AFT OML, TB0 (190.8, 41.0in.)
Comments: probable core anomaly as opposed to a disbond.

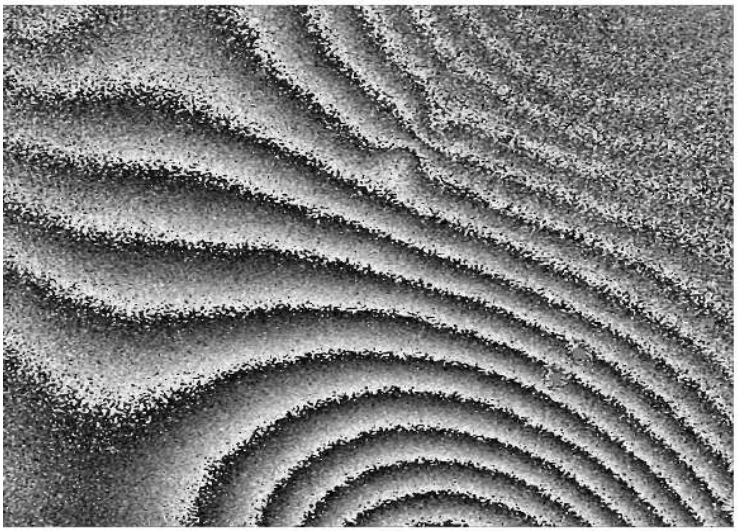

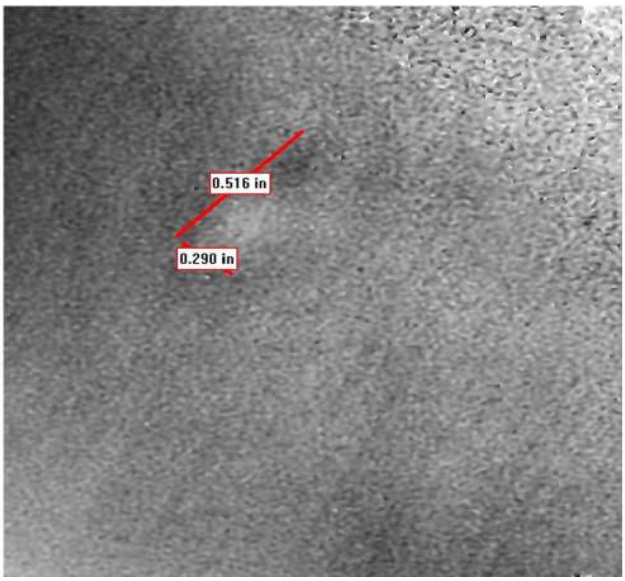

#008
Dims: 0.35 x 0.32 inches
Location: AFT OML, TB0 (239.2, 42.0 in.)
Comments: probable core anomaly as opposed to a disbond.

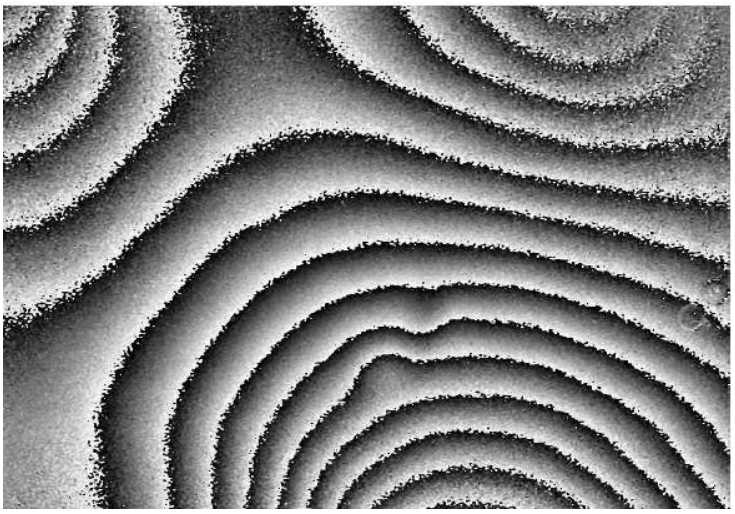

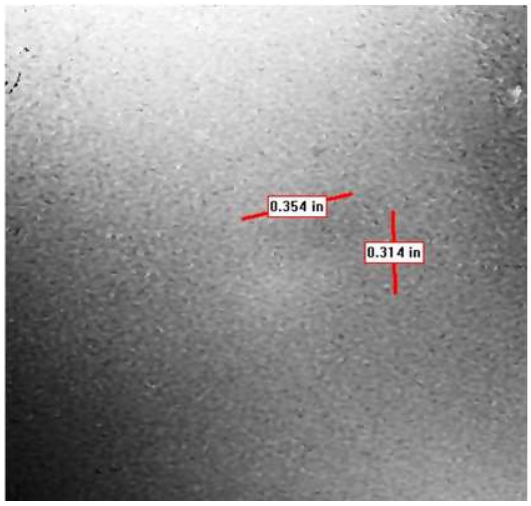

#009
Dims: Basin 0.94 x 1.26 inches
Location: AFT OML, TB0 (237.7, 26.57in.)
Comments: Honeycomb core appears attached to the face sheet over the indication, suggesting a core anomaly as opposed to a disbond.

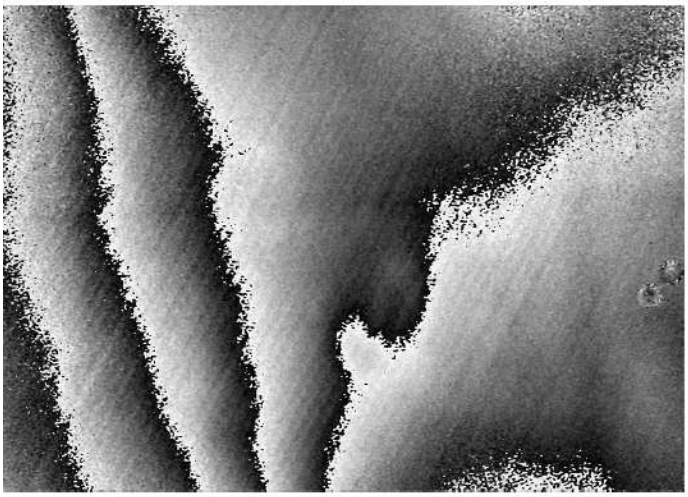

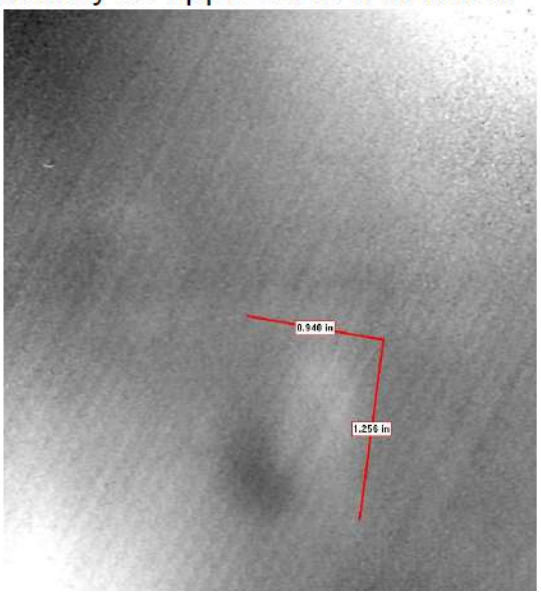

#010
Dims: 0.37 x0.83 inches
Location: AFT OML, TB3 (258.0, 42.0 in.)
Comments: A slight basin is seen, probable low velocity impact or core anomaly.

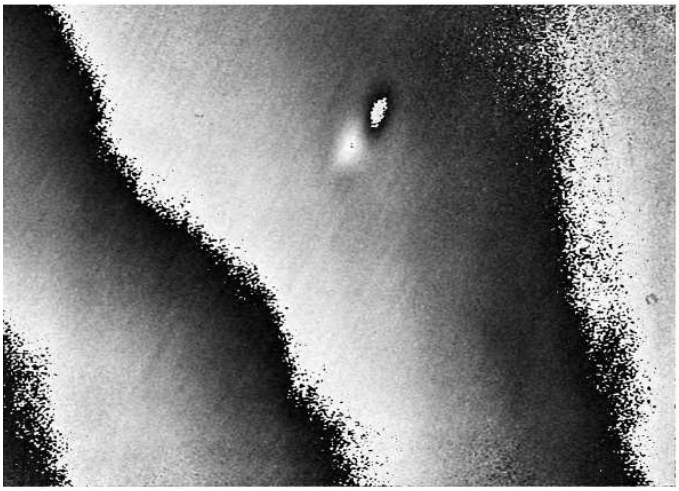

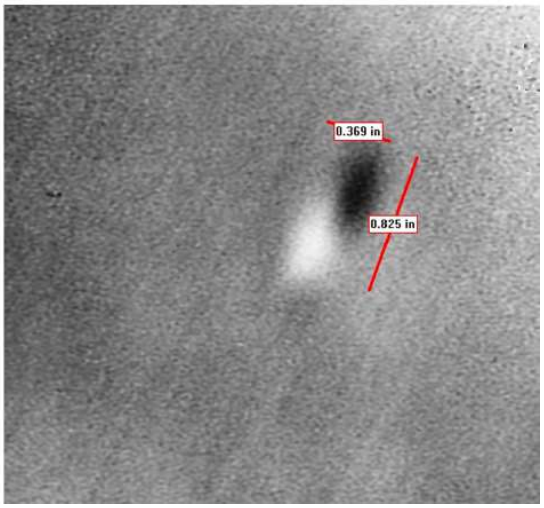

#011
Dims: Basin 0.81x0.70 inches
Location: AFT IML, TB1 (Marked on Part)
Comments: probably face sheet to core disbond.

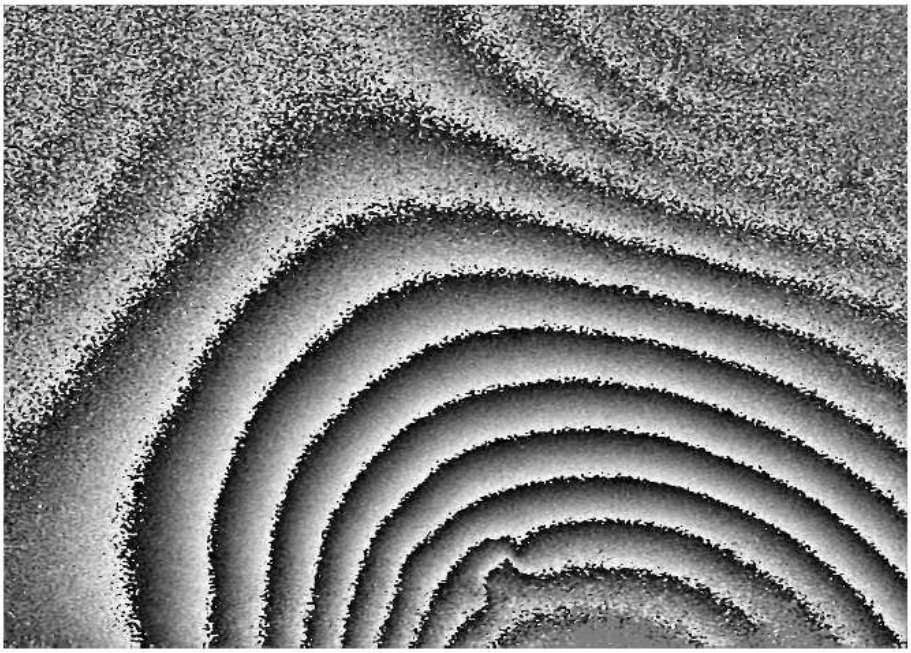

#012
Dims: Basin 0.66 x 1.0 inches
Location: FORWARD OML, TB0 (35.5, 59.0 in.)
Comments: Honeycomb core appears attached to the face sheet over the indication, suggesting a core anomaly as opposed to a disbond.

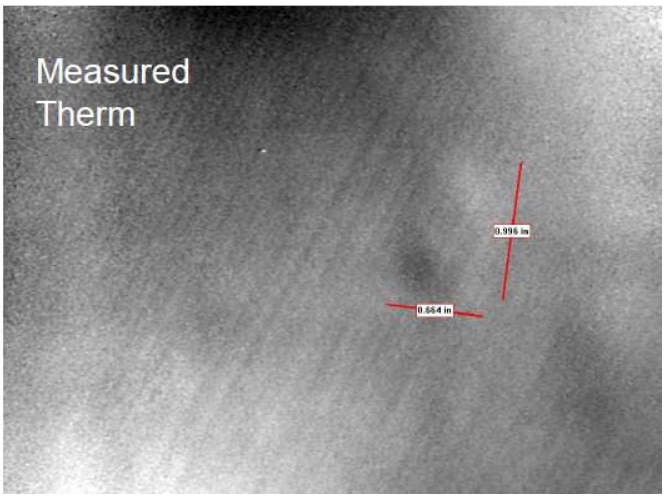

#013
Dims: 0.63 x 0.86 inches
Location: AFT OML, TB0 (36.0 x 65.5 in.)
Comments: strong indication, probable face sheet to core disbond

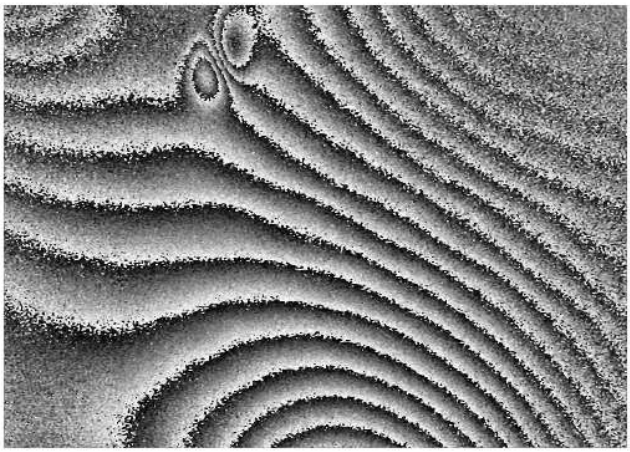

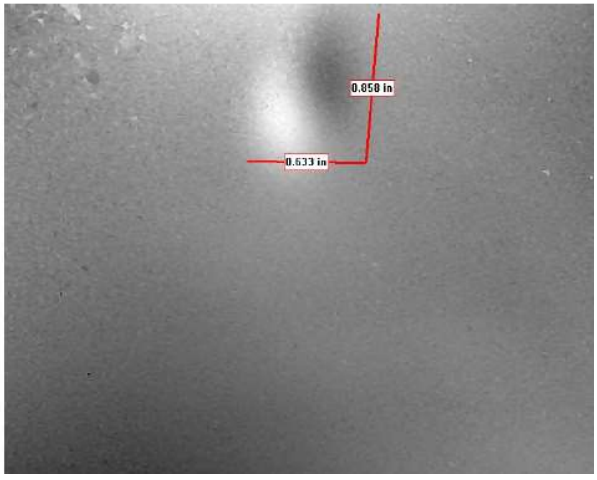

#014 & #015

Dims: #14/0.38 x 0.48 inches; #15/0.32 x 0.52
Location: AFT OML, TB0 #14/(35.7, 72.5 in.); #15/(38.0 x 77.5 in.)
Comments: Honeycomb core appears attached to the face sheet over the indication, suggesting a core anomaly as opposed to a disbond.

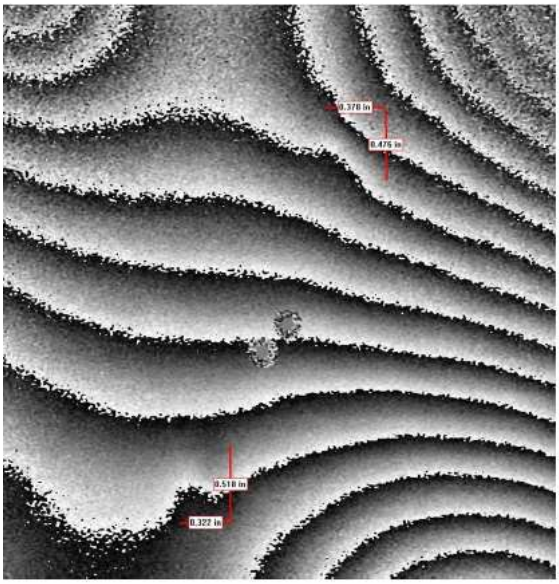

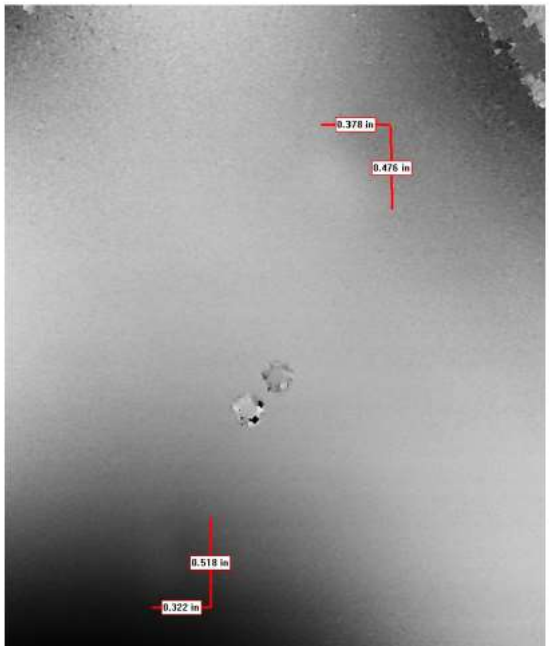

#016

Dims: #16/1.0 x 5.0 inches
Location: FORWARD OML, TB3 #16/(270.66, 6.0 in.);
Comments:

The red arrows at right show an unknown anomaly at the forward end of the barrel at the location above. This was marked with tape to facilitate secondary NDT tests.

Laminate Ply Drop